Diss. ETH No. 18543

OPTIMAL CONTROL AND DESIGN OF HYBRID-ELECTRIC VEHICLES

A dissertation submitted to
ETH ZURICH

for the degree of
Doctor of Sciences

presented by
Olle Sundström

MSc in Electrical Engineering,
Chalmers University of Technology
born November 11, 1980
citizen of Sweden

accepted on the recommendation of
Prof. Dr. Lino Guzzella, examiner
Prof. Dr. Bo Egardt, co-examiner
Dr. Patrik Soltic, co-examiner

2009

Olle Sundström
olle.sundstroem@alumni.ethz.ch

ETH Zurich
Institute for Dynamic Systems and Control
Sonneggstrasse 3
8092 Zurich, Switzerland

To my family

Preface

This work is a part of the CLEVER project which is a common project of ETH, Empa, Volkswagen AG and Robert Bosch GmbH. The project is supported in part by the Swiss Federal Office of Energy, the Swiss Federal Office of Environment, Novatlantis, the German Technical and Scientific Association for Gas and Water, and the Swiss Association for Gas and Water.

There are many people who have contributed to my work in various ways, and who deserve my deepest gratitude. First of all, I would like to thank my supervisor, Prof. Dr. Lino Guzzella, and my co-supervisor, Dr. Patrik Soltic, for providing support and guidance throughout the course of my doctoral studies, for organizing of funding, and for giving me the academic and personal freedom that allowed me to work with what, and where, I found interesting. Further, I am grateful to Prof. Dr. Bo Egardt who accepted to be my co-examiner.

I also want to acknowledge Dr. Chris Onder at the Institute for Dynamic Systems and Control, ETH Zürich, Christian Bach at Empa Dübendorf, and Antonio Sciarretta at IFP Rueil-Malmaison for their support and very helpful discussions.

Furthermore, I wish to thank my colleagues at the Institute for Dynamic Systems and Control at ETH and at the Combustion Engine Laboratory at Empa. A special thank goes to Daniel Ambühl for the valuable discussions and for the successful cooperation that led to several joint publications.

This work has given my personal satisfaction because of its potential environmental impact. I am confident that this has helped me finding motivation in difficult times.

August 2009 *Olle Sundström*

Contents

Abstract

The goal of this thesis is to develop novel model-based methods for optimal control and optimal design of hybrid electric vehicles. Two different approaches are used when designing the energy management strategy for two types of parallel hybrid electric vehicles. For the full parallel hybrid a pure mathematical approach is used while an approach derived from optimal sizing studies is used to design the energy management strategy for the torque-assist parallel hybrid.

The optimal control problem associated with the energy management in a full parallel hybrid is solved explicitly for a simplified model. The solution of the optimal control problem shows how optimal energy management strategies are derived and that the solution yields simple rules depending on vehicle parameters. Furthermore, a causal, real-time control strategy including anti-windup is presented.

The novel energy management for the torque-assist hybrid shows that the gear shifting control can be separated from the torque split control. The energy management strategy utilizes the gear shifting strategy for control of the energy flows while the torque split strategy is given by a simple rule. Results show that the proposed energy management strategy achieves a fuel consumption within 1% from the global optimum for most driving cycles. Furthermore, the results are not sensitive to limitations and energy losses associated with gear shifting.

Both the full and the torque-assist parallel hybrid vehicles are optimized with respect to the component dimensions. The overall power-to-weight ratio is kept constant while the hybridization ratio is optimized and investigated for the full hybrid and the torque-assist hybrid. The study shows the non-intuitive result that the need for hybridization is larger in the

torque-assist hybrid than in the full hybrid.

The simplicity of the torque-assist hybrid allows the optimal hybridization ratio to be found using a very simple and computationally cheap rule. The objective of this rule is to minimize the total CO_2 emissions of the vehicle, while maintaining its drivability at a constant level. The starting point is an analysis in which the optimal energy management strategy is found for eight typical driving cycles using dynamic programming. Analyzing these results, a simple yet powerful rule-based method is proposed that allows choosing the sizes of the combustion engine and of the electric motor such that the CO_2 emissions are very close to the minimum value, i.e., with a deviation of less than 1% for most driving cycles.

In the last chapter of this thesis the focus is on the dynamic programming algorithm. Issues related to the implementation of the dynamic programming algorithm for optimal control of a one-dimensional dynamic model is investigated. A study on the resolution of the discretized state space emphasizes the need for careful implementation. A novel method is presented to treat numerical issues appropriately. In particular, the method deals with numerical problems that arise due to high gradients in the optimal cost-to-go function. These gradients mainly occur on the border of the feasible state region. The proposed method not only enhances the accuracy of the solution but also allows for a reduction of the state-space resolution with maintained accuracy. The latter substantially reduces the computational effort to calculate the global optimum. Finally, the improved dynamic programming algorithm is summarized and implemented in a general, public Matlab function.

Zusammenfassung

Das Ziel dieser Arbeit ist die Entwicklung neuer, modellbasierter Methoden für die optimale Regelung und Auslegung von elektrischen Hybridfahrzeugen. Zwei verschiedene Ansätze werden angewandt für die Entwicklung des Energiemanagements für zwei Typen von parallelen elektrischen Hybridfahrzeugen. Für den Fall eines Vollhybridfahrzeuges wird ein rein mathematischer Ansatz angewandt, während das Energiemanagement für ein mildes Hybridfahrzeug aus Studien der optimalen Auslegung abgeleitet wird.

Das Optimal Control Problem für das Energiemanagement von parallelen Vollhybridfahrzeugen wird explizit gelöst für ein vereinfachtes Modell. Diese Lösung zeigt auf, wie optimale Energiemanagementstrategien hergeleitet werden und dass die resultierenden Lösungen einfache Regeln darstellen, welche durch die Fahrzeugparameter definiert sind. Desweiteren wird eine darauf basierende kausale Echtzeitstrategie mit Anti-Windup hergeleitet.

Ein neuartiges Energiemanagement für milde Hybridfahrzeuge zeigt auf, dass die Gangwahl von der Regelung der Momentenaufteilung separiert werden kann. Dieses Energiemanagement verwendet die Gangwahl zur Steuerung der Energieflüsse während die Momentenaufteilung durch einfache Regeln vorgegeben wird. Die Resultate zeigen, dass dieses Energiemanagement Treibstoffverbräuche erzielt, welche für die meisten Fahrzyklen weniger als 1% Abweichung vom globalen Optimum aufweisen. Die erzielten Resultate sind insensitiv bezüglich Beschränkungen und energetischen Verlusten bei Gangschaltvorgängen.

Sowohl das Voll- wie auch das Mildhyridfahrzeug werden bezüglich Komponentendimensionierung optimiert. Das Leistungs/Gewichts-Verhält-

nis wird konstant gehalten während der Hybridisierungsgrad optimiert wird. Der Unterschied zwischen optimalem Hybridisierungsgrad für Voll- beziehungsweise Mildhybridfahrzeug wird untersucht. Die Resultate zeigen überaschenderweise, dass milde Hybridfahrzeuge höhere optimale Hybridisierungsgrade benötigen als Vollhybridfahrzeuge.

Die Einfachheit von milden Hybriden erlaubt den optimalen Hybridisierungsgrad mittels einer sehr einfachen und rechnerisch effizienten Regel zu finden. Das Ziel dieser Regel ist die Minimierung der totalen CO_2 Emissionen des Fahrzeuges, wobei die Fahrleistungen konstant gehalten werden. Ausgangspunkt ist eine Analyse, in welcher die optimale Energiemanagementstrategie mittels Dynamischer Programmierung für acht typische Fahrzyklen ausgewertet wird. Die Untersuchung dieser Resultate erlaubt die Herleitung einer einfachen, aber effektiven Methode, die es erlaubt, die Dimensionierung des Verbrennungsmotors und des Elektromotors so zu wählen, dass die CO_2 Emissionen sehr nahe beim Minimum liegen. Die Abweichungen sind kleiner als 1% für die meisten Fahrzyklen.

Das letzte Kapitel dieser Arbeit fokussiert auf den Algorithmus der Dynamischen Programmierung. Probleme bezüglich der Implementierung der Dynamischen Programmierung für eindimensionale Optimal Control Probleme werden untersucht. Eine Studie der Auflösung des diskretisierten Zustandsraumes verdeutlicht die Notwendigkeit einer exakten Implementierung. Eine neue Methode wird vorgestellt, die es erlaubt, diese numerischen Probleme korrekt zu behandeln. Die Methode behandelt numerische Probleme, die aufgrund grosser Gradienten in der optimalen Restkostenfunktion auftreten. Diese Gradienten treten meist am Rand des lösbaren Zustandsraumes auf. Die vorgestellte Methode verbessert nicht nur die Genauigkeit des gefundenen Lösungen, sondern sie erlaubt auch die Auflösung des Zustandsraumes zu reduzieren bei gleicher Genauigkeit wie im ursprünglichen Problem . Diese Reduktion der Auflösung reduziert den Rechenaufwand für die Auswertung des globalen Optimums wesentlich. Der verbesserte Algorithmus der Dynamischen Programmierung wird letztlich zusammengefasst und in einer Matlabfunktion implementiert.

Chapter 1

Introduction

1.1 Hybrid Electric Vehicles

Hybrid electric vehicles, i.e., vehicles that include an electric path (electric motor and electric energy storage) are an interesting solution to the problem of reducing the carbon dioxide emissions of passenger vehicles. Compared to conventional automobiles, the main benefits of hybrid electric vehicles are the additional operating modes possible and the possibility of downsizing the combustion engine and thus operating it most of the time at higher efficiencies. The additional operating modes are (1) brake energy recuperation, (2) engine start-stop operation, (3) engine operating point shifting and, for some configurations, (4) pure electric driving. However, the main drawback of hybridizing a conventional combustion engine based powertrain is the additional system complexity and cost.

There exist several types of topologies of hybrid electric vehicle, such as series, parallel, and split hybrids. In this text a parallel type is considered, where there is only one mechanical connection between the electric motor and combustion engine. However, the methods proposed in this text can easily be extended to other topologies. The two main types of parallel hybrids are the full parallel hybrid and the torque-assist parallel hybrid, also known as single-shaft hybrid [1], mild hybrid [2], or power-assist hybrid. In the full hybrid the combustion engine can be decoupled from the electric motor using an electronically controlled clutch. Frequent opening and closing of this clutch during normal driving operation requires

careful control [3] and puts high requirements on the components in order to guarantee a sufficient lifetime. The torque-assist hybrid, on the other hand, does not require an electronically controlled clutch since the electric motor is always coupled with the combustion engine. The disadvantage of not having a clutch is the reduced possibility to utilize pure electric driving and recharging operation in the vehicle [4].

1.2 Objectives of this Thesis

In the thesis at hand, the optimal control and optimal design of hybrid electric vehicles are investigated. There are three main objectives of this text. The first objective is to explain in detail how the optimal control of the power split between the two energy converters is derived mathematically and to show the implications for real-time applications. The second objective is to show how the interconnection between optimal control and optimal sizing of the components in hybrid vehicles can help in developing both energy management strategies and sizing rules. The third objective is to develop efficient tools for calculating the optimal control of hybrid vehicles. The text is intended to give the reader new perspectives on how to optimize hybrid electric vehicles.

1.3 Contributions of this Thesis

This work, with the objectives presented in the previous section, resulted in several contributions to the field of optimal control and design of hybrid electric vehicles.

Two different approaches are used when designing the energy management strategy for the two parallel hybrid electric vehicles. For the full parallel hybrid, a pure mathematical approach is used while an approach derived from optimal sizing is used for the torque-assist parallel hybrid. The mathematical approach for the full parallel hybrid shows that the optimal control problem associated with the energy management can be solved explicitly, as shown in [I]. The solution shows that the optimal

energy management strategy is in fact a set of simple rules depending on vehicle parameters. The approach for the torque-assist hybrid in [II] shows that the gear shifting control can be separated from the torque distribution control. The development of the gear shifting energy management strategy led to the patent application [III]. This energy management strategy is derived from a simple rule developed for determining the optimal hybridization ratio in a torque-assist hybrid.

The optimal hybridization ratio in the full hybrid and the torque-assist hybrid are investigated in [IV]. This investigation shows the non-intuitive results that the need for hybridization is larger in a torque-assist hybrid than in a full hybrid. Moreover, the simplicity of the torque-assist hybrid allows the optimal hybridization ratio to be found using a very simple and computationally cheap rule, as explained in [V].

Finally, a key tool for evaluating hybrid vehicles is the dynamic programming algorithm. In [VI] and [VII] a novel method for improving the accuracy of the dynamic programming algorithm is presented. The method is particularly useful for solving optimal control problems with final state constraints. The method allows the state-grid resolution to be reduced and thus reducing the computational demand. The improved dynamic programming algorithm is implemented in Matlab and an overview of the function is presented in [VIII]. This implementation allows researchers to quickly and accurately solve dynamic programming problems.

1.4 Publications Associated with this Thesis

The following publications are associated with this project:

[I] D. Ambühl, O. Sundström, A. Sciarretta, L. Guzzella, "Explicit Optimal Control Policy and its Practical Application for Hybrid Electric Powertrains", *Control Engineering Practice*, 2009, Submitted for publication

[II] O. Sundström, L. Guzzella, and P. Soltic, "A Transmission-Actuated Energy Management Strategy", *IEEE Transactions on Vehicular Technology*, 2009, Accepted for publication

[III] O. Sundström, L. Guzzella, P. Soltic, and T. Huber, "Betriebstrategie für milde hybrid fahrzeuge", *Deutsches Patent- und Markenamt*, Germany, Submitted on 24 November 2008

[IV] O. Sundström, L. Guzzella, and P. Soltic, "Optimal Hybridization in Two Parallel Hybrid Electric Vehicles using Dynamic Programming", In *Proceedings of the 17th IFAC World Congress*, pages 4642-4647, Seoul, Korea, 2008

[V] O. Sundström, L. Guzzella, and P. Soltic, "Torque-Assist Hybrid Electric Powertrain Sizing: From Optimal Control Towards a Sizing Law", *IEEE Transactions on Control Systems Technology*, 2009, Accepted for publication

[VI] O. Sundström, D. Ambühl, and L. Guzzella, "On Implementation of Dynamic Programming for Optimal Control Problems with Final State Constraints", *Oil & Gas Science and Technology - Rev. IFP, DOI : 10.2516/ogst:2009020*, 2009, Accepted for publication

[VII] O. Sundström, D. Ambühl, and L. Guzzella, "On Implementation of Dynamic Programming for Optimal Control Problems with Final State Constraints", In *Proceedings of Les Rencontres Scientifiques de l'IFP Advances in Hybrid Powertrains*, Rueil-Malmaison, France, 2008

[VIII] O. Sundström and L. Guzzella, "A Generic Dynamic Programming Matlab Function", In *Proceedings of the 18th IEEE International Conference on Control Applications*, pages 1625-1630, Saint Petersburg, Russia, 2009

Chapter 2

Control of Hybrid Electric Vehicles

Minimization of the integral fuel consumption of hybrid electric vehicles requires appropriate control of the power distribution between the primary and the secondary power converter. This optimal control problem is often referred to as the energy management problem in literature. Various approaches have been published so far. These approaches are typically divided into two groups, namely heuristic strategies and optimal strategies [5].

Heuristic approaches are often applied in real-time implementations. Low fuel consumption can be achieved, but the performance is very sensitive to the tuning of the rules. A typical rule-based method is fuzzy logic, which was used by [6] and [7]. Such a heuristic control strategies are in general not scalable, since these rules are often not model-based. [8] used a different approach where they used the results obtained from dynamic programming to extract rules.

On the other hand, strategies minimizing a local cost function to find the actual control proved to achieve low fuel consumption. This local cost function is typically an equivalent fuel consumption that consists of the actual fuel consumption and a weighted electric consumption. These approaches were introduced by [9, 10] and [11] and further improved by [12] and [13]. The local minimization strategies require a model of the powertrain, but are easily scalable. However, such strategies can require more computational power than rule-based methods, since an online optimization has to be carried out in real-time operation. In [14] and [15] the authors used Pontryagin's minimum principle to derive similar strategies

that minimize a local cost function.

In the first part of this chapter an optimal strategy based on Pontryagin's minimum principle is derived for a full parallel hybrid. In the second part an energy management strategy is derived for a torque-assist parallel hybrid. The strategy for the torque-assist hybrid controls both the torque split and the gear shifting and it is a combination of a rule-based and an optimal strategy.

2.1 Control of a Full Parallel Hybrid

In this section the explicit optimal control of a full parallel hybrid is studied. First a speed independent, unconstrained model of the full parallel hybrid is presented. This model allows for an analytical solution of the optimal control, resulting in clearly defined rules. This rule-based control is one of the main findings in this part of the chapter. All rules are well defined by powertrain parameters only and close the gap between optimal strategies and heuristic strategies.

The simplified model is then extended to a speed dependent, input constrained model. The analytical optimal control for the extended model is found similarly to the one for the first model. The control can still be expressed as clearly defined rules being now speed dependent. The analytical solution is then used to derive a causal controller. This solution allows to derive an anti-windup scheme, for the integrator in the causal controller, using only powertrain parameters.

2.1.1 Speed Independent Model

For the parallel hybrid electric powertrain whose structure is illustrated in Fig. 2.1, we use a simplified model relating the total power demand $P_d(t)$, the motor power $P_m(t)$, and the engine power $P_e(t)$ to the fuel power $P_f(t)$, the battery power $P_b(t)$, and the energy content in the battery $E_b(t)$. Assuming a battery model with a voltage source V_{oc} in series with

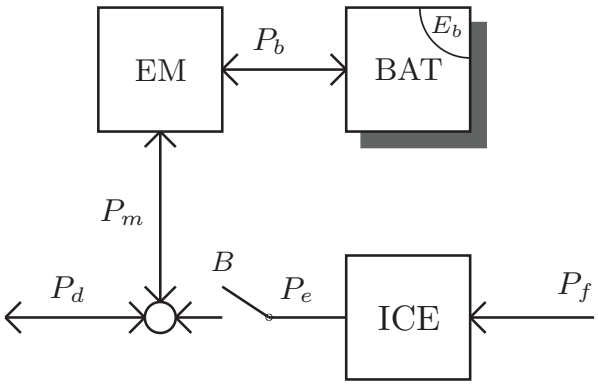

Figure 2.1: Topology of the parallel hybrid electric powertrain. EM and ICE are static blocks while BAT is a dynamic block with the state variable E_b. The variable B decides whether the engine is on and the clutch is closed.

a resistor R, the battery current I_b is given by

$$I_b = \frac{V_{oc} - \sqrt{V_{oc}^2 - 4RP_b}}{2R}. \tag{2.1}$$

The total power loss over the resistance is

$$P_l(P_b) = RI_b^2 = \frac{\left(V_{oc} - \sqrt{V_{oc}^2 - 4RP_b}\right)^2}{4R}. \tag{2.2}$$

Approximating the power loss using a Taylor series around $P_b = 0$ yields

$$P_l(P_b) \approx P_l(0) + \frac{P_l^{'}(0)}{1!} \cdot P_b + \frac{P_l^{''}(0)}{2!} \cdot P_b^2 + \mathcal{O}(P_b^3) \tag{2.3}$$

$$= 0 + 0 \cdot P_b + \frac{R}{V_{oc}^2} \cdot P_b^2 + \mathcal{O}(P_b^3). \tag{2.4}$$

Throughout this section, the battery power loss in the simplified model is therefore assumed to be

$$P_l(P_b) = \frac{R}{V_{oc}^2} \cdot P_b^2 = \alpha P_b^2. \tag{2.5}$$

The model equations are

$$P_e(t) = P_d(t) - P_m(t) \tag{2.6}$$

$$P_f(t) = \frac{P_e(P_m(t), P_d(t)) + P_0}{e} \cdot B \tag{2.7}$$

$$P_b(t) = P_m(t) \cdot \eta^{-\mathrm{sgn}(P_m(t))} \tag{2.8}$$

$$\frac{d}{dt}E_b(t) = -P_b(P_m(t)) - \alpha P_b(P_m(t))^2, \tag{2.9}$$

where B is equal to one when the fuel injection is active (engine on) and the clutch between engine and motor is engaged, $(P_e(t) > 0)$, P_0 is the engine friction power, e its internal efficiency, η the efficiency of the electric motor, and $\alpha = \frac{R}{V_{oc}^2}$. The only state variable of this model is the energy content of the battery $E_b(t)$ given by (2.9). In the remainder of this section the time dependencies of the variables P_d, P_e, P_m, P_f, P_b, and E_b in the model equations (2.6)–(2.9) are omitted to increase readability.

Initially, the only constraint to the model is that the engine cannot provide any negative power,

$$P_e \in [0, \infty) \tag{2.10}$$

$$P_m \in (-\infty, \infty). \tag{2.11}$$

However, in Section 2.1.5 constraints are added to the model in order to achieve a more realistic behavior.

Table 2.1: Parameters of the powertrain

Parameter	Value	Unit
P_0	$4.5 \cdot 10^3$	W
e	0.4	-
η	0.9	-
R	0.5	Ω
V_{oc}	300	V
$\alpha = \frac{R}{V_{oc}^2}$	$\approx 5.6 \cdot 10^{-6}$	W^{-1}

2.1.2 Optimal Control

The optimal control problem consists of finding the optimal power signal for the electric motor P_m^o such that the fuel consumption is minimized and the charge in the battery is sustained over the driving cycle. The requested power profile P_d is given by the driving cycle as a disturbance and the final time t_f, being the duration of the cycle, is fixed.

The optimal control problem is formulated by the cost functional, the system dynamics, input constraints and state constraints, and the initial and the final condition. The cost functional to be minimized, which is the total fuel (energy) consumption over the driving cycle is

$$J = \int_0^{t_f} P_f(\tau) d\tau. \tag{2.12}$$

While the system dynamics and input constraints are given by (2.6)–(2.11), the state constraints are neglected throughout this section. The initial and the final condition are chosen equal to zero such that charge sustenance is guaranteed

$$E_b(0) = E_b(t_f) = 0. \tag{2.13}$$

Hence, a positive (negative) battery energy content $E_b(t)$ indicates that the battery is charged (discharged) at time t compared to the initial condition. Note that the energy content of batteries is in general bounded. However, the optimal control problems solved in this section neglect the bounds on the state. This assumption allows for explicit solutions. Nevertheless, as it will be shown in Section 2.1.8, the battery's energy content can still be kept within reasonable bounds by an appropriate causal control.

2.1.3 Pontryagin's Minimum Principle

The solution to the optimal control problem stated above is solved using Pontryagin's minimum principle. This method has been successfully applied by [14]. This section shows the detailed derivation of the optimal control law using the simplified model. The formulation of the optimal control problem defined by (2.6)–(2.13) yields the following Hamiltonian

[16]

$$\begin{aligned} H &= P_f - \lambda \cdot \left(P_b + \alpha P_b^2\right) \\ &= \frac{P_d - P_m + P_0}{e} \cdot B - \lambda \cdot \left(P_m \cdot \eta^{-\mathrm{sgn}(P_m)} + \alpha P_m^2 \cdot \eta^{-2\mathrm{sgn}(P_m)}\right). \end{aligned} \tag{2.14}$$

If the control P_m^o is optimal, then the conditions (2.15)–(2.19) are satisfied according to Pontryagin's minimum principle.

$$\frac{d}{dt} E_b^o = -P_m^o \cdot \eta^{-\mathrm{sgn}(P_m^o)} - \alpha \left(P_m^o \cdot \eta^{-\mathrm{sgn}(P_m)}\right)^2 \tag{2.15}$$

$$E_b^o(0) = 0 \tag{2.16}$$

$$E_b^o(t_f) = 0 \tag{2.17}$$

$$\frac{d}{dt} \lambda^o = -\nabla_{E_b} H|_o = 0 \tag{2.18}$$

$$H(P_m^o, \lambda^o, t) \leq H(P_m, \lambda^o, t) \tag{2.19}$$

These conditions are necessary for optimality. Since the Hamiltonian is not a function of the state variable E_b, the optimal co-state λ^o is constant. Throughout this section the constant optimal co-state (2.20), with inverted sign, is referred to as *equivalence factor*, s, since it is weighting the electric power in the battery with the chemical power provided by fuel in the Hamiltonian (2.14).

$$\lambda^o(t) = -s \tag{2.20}$$

Equation (2.19) states that P_m^o can only be optimal if it is the global minimizer of the Hamiltonian. Therefore, the Hamiltonian is carefully analyzed in the following to derive the optimal control law. The Hamiltonian (2.14) expressed as a piecewise function is

$$H = \begin{cases} \frac{P_d+P_0}{e} + \left(s\eta - \frac{1}{e}\right) P_m + s\alpha\eta^2 P_m^2, & \text{if } P_m \leq 0 < P_d - P_m \\ \frac{P_d+P_0}{e} + \left(\frac{s}{\eta} - \frac{1}{e}\right) P_m + \frac{s\alpha}{\eta^2} P_m^2, & \text{if } 0 \leq P_m < P_d \\ \frac{s}{\eta} P_m + \frac{s\alpha}{\eta^2} P_m^2, & \text{if } P_m = P_d \geq 0 \\ s\eta P_m + s\alpha\eta^2 P_m^2, & \text{if } P_m = P_d \leq 0 \end{cases} \tag{2.21}$$

The first interval $P_m \leq 0 < P_d - P_m$ indicates that the electric motor power is negative $P_m < 0$ and the engine power positive $P_e = P_d - P_m > 0$.

To simplify the explanations throughout this section, the four parts of the Hamiltonian (2.21), together with the special case $P_m = 0 < P_d$, are

defined as

$$H_{re} = \frac{P_d + P_0}{e} + \left(s\eta - \frac{1}{e}\right) P_m + s\alpha\eta^2 P_m^2, \quad \text{for } P_m < 0 < P_d - P_m \tag{2.22}$$

$$H_{th} = \frac{P_d + P_0}{e}, \quad \text{for } P_m = 0 < P_d \tag{2.23}$$

$$H_{bo} = \frac{P_d + P_0}{e} + \left(\frac{s}{\eta} - \frac{1}{e}\right) P_m + \frac{s\alpha}{\eta^2} P_m^2, \quad \text{for } 0 < P_m < P_d \tag{2.24}$$

$$H_{el} = \frac{s}{\eta} P_m + \frac{s\alpha}{\eta^2} P_m^2, \quad \text{for } P_m = P_d \geq 0, \tag{2.25}$$

$$H_{el}^- = s\eta P_m + s\alpha\eta^2 P_m^2, \quad \text{for } P_m = P_d \leq 0, \tag{2.26}$$

where H_{re} is the Hamiltonian for recharging, H_{th} represents pure thermal operation, H_{bo} boosting, H_{el} pure electric propulsion, and H_{el}^- pure electric recuperation.

To find the control P_m that minimizes the Hamiltonian (2.21), the first and second derivatives of the Hamiltonian with respect to the control P_m are analyzed. Since the Hamiltonian is not differentiable at $P_m = 0$ and $P_m = P_d$, the derivatives are only analyzed for H_{re} and H_{bo}

$$\frac{\partial H_{re}}{\partial P_m} = \left(s\eta - \frac{1}{e}\right) + 2s\alpha\eta^2 P_m, \quad \text{for } P_m < 0 < P_d - P_m \tag{2.27}$$

$$\frac{\partial H_{bo}}{\partial P_m} = \left(\frac{s}{\eta} - \frac{1}{e}\right) + 2\frac{s\alpha}{\eta^2} P_m, \quad \text{for } 0 < P_m < P_d. \tag{2.28}$$

Since the parameters α and η are positive and s is assumed to be positive[1], the second derivatives of the Hamiltonians H_{re} and H_{bo} are positive

$$\frac{\partial^2 H_{re}}{\partial P_m^2} = 2s\alpha\eta^2 > 0 \tag{2.29}$$

$$\frac{\partial^2 H_{bo}}{\partial P_m^2} = 2\frac{s\alpha}{\eta^2} > 0. \tag{2.30}$$

To analyze the change in the derivative $\frac{\partial H}{\partial P_m}$ at the point $P_m = 0$ the limits of the first derivatives (2.27) and (2.28) are investigated. The limits when

[1] A posteriori checking of the optimal solution will reveal that this assumption was valid.

P_m is approaching zero are

$$\lim_{P_m \to 0^-} \frac{\partial H_{re}}{\partial P_m} = s\eta - \frac{1}{e} \tag{2.31}$$

$$\lim_{P_m \to 0^+} \frac{\partial H_{bo}}{\partial P_m} = \frac{s}{\eta} - \frac{1}{e}, \tag{2.32}$$

where

$$\lim_{P_m \to 0^-} \frac{\partial H_{re}}{\partial P_m} < \lim_{P_m \to 0^+} \frac{\partial H_{bo}}{\partial P_m}. \tag{2.33}$$

Equation 2.33 is true for any s since $0 < \eta < 1$. Equation (2.33), together with the property of the second derivative (2.29)–(2.30), proves that

$$\frac{\partial H_{re}}{\partial P_m} < \frac{\partial H_{bo}}{\partial P_m}. \tag{2.34}$$

This property will be used in the following for the minimization of the Hamiltonian.

Minimization for $P_d > 0$

The minimum of the Hamiltonian can be found, depending on the value of s, in different intervals of the control P_m. A sketch of the Hamiltonian for all intervals of s is shown in Fig. 2.2. There is a discontinuity in the Hamiltonian at $P_m = P_d$. Hence, this control can be an optimal control candidate for all intervals in s.

The minimization of the Hamiltonian for its continuous part is carried out by analyzing its derivatives. If the limit of the derivative of H_{bo} (2.32) is negative, i.e. $s < \frac{\eta}{e}$, the optimum of the Hamiltonian is either in H_{bo} or in H_{el}. If the limit of the derivative of H_{re} (2.31) is positive, i.e. $s > \frac{1}{\eta e}$, the optimum of the Hamiltonian is either in H_{re} or in H_{el}. Finally, if the limit of the derivative of H_{bo} (2.32) is positive and the limit of the derivative of H_{re} (2.32) is negative, then the optimum is either in H_{th} or in H_{el}. These conclusions can be summarized as

$$\min_{P_m} H(P_m) = \begin{cases} \min\{H_{el}, H_{bo}\}, & \text{if } s < \frac{\eta}{e} \\ \min\{H_{el}, H_{th}\}, & \text{if } \frac{\eta}{e} \le s \le \frac{1}{\eta e} \\ \min\{H_{el}, H_{re}\}, & \text{if } s > \frac{1}{\eta e} \end{cases} \tag{2.35}$$

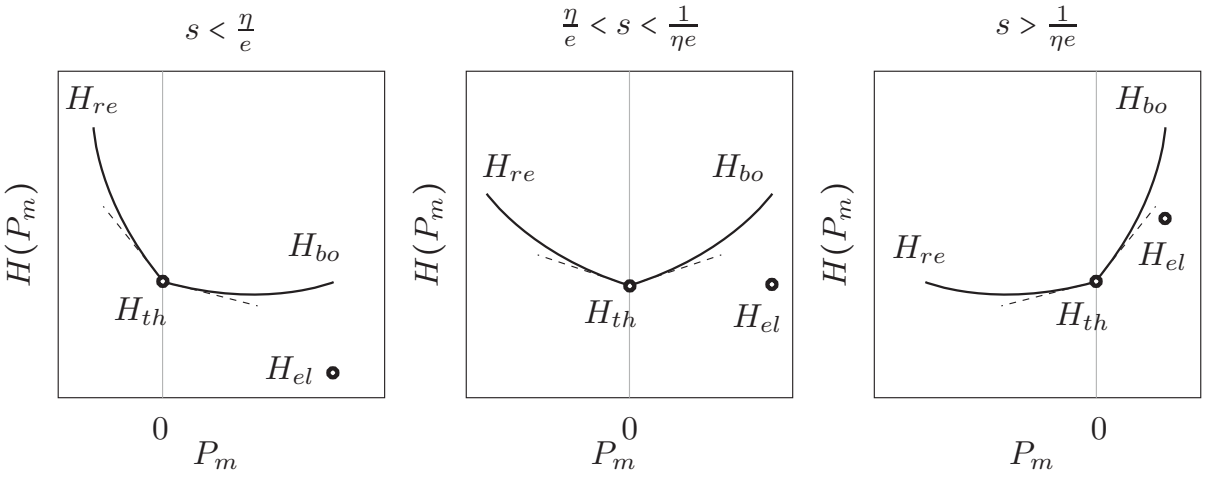

Figure 2.2: Schematic overview of the shape of the Hamiltonians H_{re} and H_{bo} for all intervals of s.

To find the control P_m that minimizes the Hamiltonian H_{bo} (2.24), the derivative (2.28) is set to zero and solved for P_m.

$$\frac{\partial H_{bo}}{\partial P_m} = \left(\frac{s}{\eta} - \frac{1}{e}\right) + 2\frac{s\alpha}{\eta^2} P_m = 0 \tag{2.36}$$

$$\Rightarrow P_m = P_m^{bo}(s) \triangleq \frac{\eta(\frac{\eta}{e} - s)}{2s\alpha} \tag{2.37}$$

To find the control P_m that minimizes the Hamiltonian H_{re} (2.22), the derivative (2.27) is set to zero and solved for P_m.

$$\frac{\partial H_{re}}{\partial P_m} = \left(s\eta - \frac{1}{e}\right) + 2s\alpha\eta^2 P_m = 0 \tag{2.38}$$

$$\Rightarrow P_m = P_m^{re}(s) \triangleq -\frac{s - \frac{1}{\eta e}}{2s\alpha\eta} \tag{2.39}$$

The candidates for the optimal control P_m^o corresponding to (2.35) are therefore

$$P_m^o \in \begin{cases} \{P_d,\ P_m^{bo}(s)\}, & \text{if } s < \frac{\eta}{e} \\ \{P_d,\ 0\}, & \text{if } \frac{\eta}{e} \le s \le \frac{1}{\eta e} \\ \{P_d,\ P_m^{re}(s)\}, & \text{if } s > \frac{1}{\eta e}. \end{cases} \tag{2.40}$$

The control that minimizes the Hamiltonian is determined by comparing the Hamiltonians in (2.35) when using the corresponding optimal control candidates in (2.40).

For $s < \frac{\eta}{e}$, only $H_{el}(P_d)$ and $H_{bo}(P_m^{bo}(s))$ can be optimal according to (2.35) and (2.40). Therefore, the condition for pure electric driving is

$H_{el}(P_d) < H_{bo}\left(P_m^{bo}(s)\right)$. Solving this inequality for the power demand P_d yields the condition for pure electric driving, namely

$$P_d < P_{lim}^{bo}(s) \triangleq \frac{-\left(\frac{s}{\eta} - \frac{1}{e}\right) + \sqrt{4\frac{s\alpha}{\eta^2}\frac{P_0}{e}}}{2\frac{s\alpha}{\eta^2}}. \tag{2.41}$$

For $\frac{\eta}{e} \leq s \leq \frac{1}{\eta e}$, the condition $H_{el}(P_d) < H_{th}(0)$ yields as condition for pure electric driving

$$P_d < P_{lim}^{th}(s) \triangleq \frac{-\left(\frac{s}{\eta} - \frac{1}{e}\right) + \sqrt{\left(\frac{s}{\eta} - \frac{1}{e}\right)^2 + 4\frac{s\alpha}{\eta^2}\frac{P_0}{e}}}{2\frac{s\alpha}{\eta^2}}. \tag{2.42}$$

For $s > \frac{1}{\eta e}$, from $H_{el}(P_d) < H_{re}\left(P_m^{re}(s)\right)$ it follows

$$P_d < P_{lim}^{re}(s) \triangleq \frac{-\left(\frac{s}{\eta} - \frac{1}{e}\right) + \sqrt{\left(\frac{s}{\eta} - \frac{1}{e}\right)^2 - \left(\frac{s}{\eta} - \frac{1}{e\eta^2}\right)^2 + 4\frac{s\alpha}{\eta^2}\frac{P_0}{e}}}{2\frac{s\alpha}{\eta^2}}. \tag{2.43}$$

It is interesting to note that for equality of the above conditions, i.e. $P_d = P_{lim}^{(\cdot)}$, the Hamiltonian has two identical minima. For a constant power demand, this would result in singular optimal control as investigated by [17]. The only charge-sustaining solution would be either pure thermal propulsion or duty cycling between pure electric and recharging. In reality, the power profile is never constant over the entire problem duration. Consequently, the optimal control for $P_d = P_{lim}^{(\cdot)}$ is chosen to be pure electric $P_m^o = P_d$ without loss of optimality.

Minimization for $P_d < 0$

When $P_d < 0$, both boosting H_{bo} and pure thermal driving H_{th} are not possible since $P_e \in [0,\ \infty)$. The Hamiltonian H_{re} given by (2.22) is possible when $P_d - P_m > 0$. Equation (2.22) remains the same when $P_d < 0$. However, the Hamiltonian for pure electric recuperation (2.26) is different from the one of pure electric driving (2.25). During braking phases ($P_d < 0$), the only candidates are therefore $H_{re}\left(P_m^{re}(s)\right)$ and $H_{el}^{-}(P_d)$. Pure electric

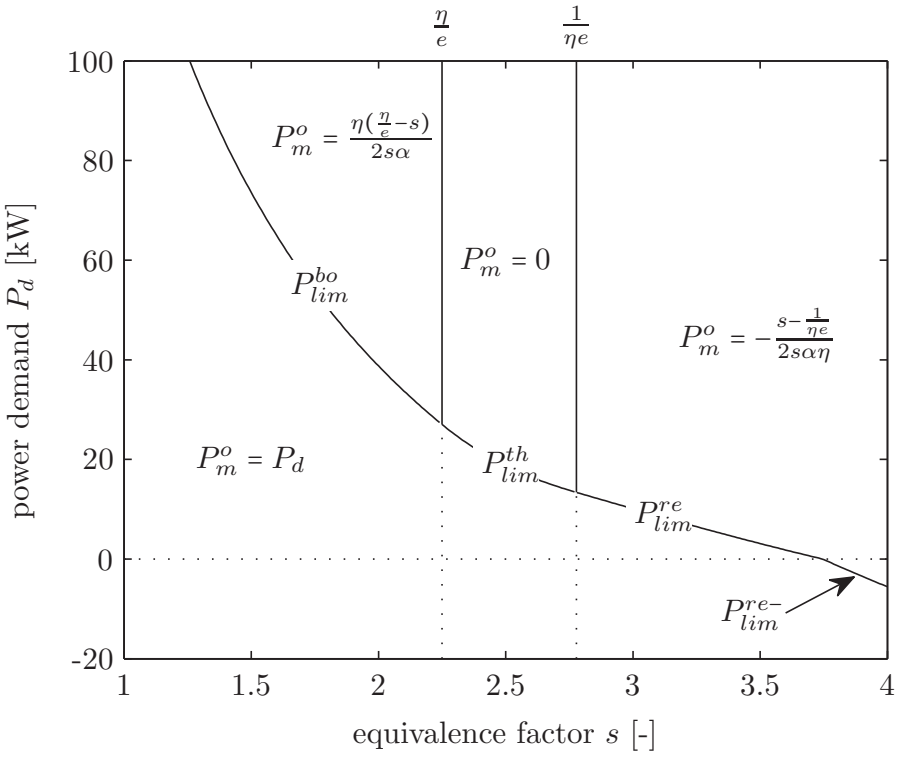

Figure 2.3: Overview of the regions with the different optimal control P_m^o (separated by solid lines) and the power limits $P_{lim}^{(\cdot)}$ for the unconstrained problem.

recuperation is optimal if

$$H_{el}^{-}(P_d) < H_{re}\left(P_m^{re}(s)\right) \tag{2.44}$$

$$P_d < P_{lim}^{re-}(s) \triangleq \frac{-\left(s\eta - \frac{1}{e}\right) + \sqrt{4s\alpha\eta^2\frac{P_0}{e}}}{2s\alpha\eta^2}. \tag{2.45}$$

2.1.4 Resulting Optimal Control Law

The resulting optimal control law can be represented as a clearly defined map. This map is shown in Fig. 2.3 for a powertrain with the parameters specified in Table 2.1. It contains the optimal motor power as a function of a constant equivalence factor s and the requested power P_d. The constant equivalence factor s is introduced in Section 2.1.3 below, where the optimal control law is derived in detail. The optimal control law consists of only four regions, namely pure electric driving (including recuperation), pure thermal, boosting, and recharging.

The power limits $P_{lim}^{(\cdot)}$ separating the four regions in the control map are given by

$$P_{lim}^{bo}(s) = \frac{-\left(\frac{s}{\eta} - \frac{1}{e}\right) + \sqrt{4\frac{s\alpha}{\eta^2}\frac{P_0}{e}}}{2\frac{s\alpha}{\eta^2}} \tag{2.46}$$

$$P_{lim}^{th}(s) = \frac{-\left(\frac{s}{\eta} - \frac{1}{e}\right) + \sqrt{\left(\frac{s}{\eta} - \frac{1}{e}\right)^2 + 4\frac{s\alpha}{\eta^2}\frac{P_0}{e}}}{2\frac{s\alpha}{\eta^2}} \tag{2.47}$$

$$P_{lim}^{re}(s) = \frac{-\left(\frac{s}{\eta} - \frac{1}{e}\right) + \sqrt{\left(\frac{s}{\eta} - \frac{1}{e}\right)^2 - \left(\frac{s}{\eta} - \frac{1}{e\eta^2}\right)^2 + 4\frac{s\alpha}{\eta^2}\frac{P_0}{e}}}{2\frac{s\alpha}{\eta^2}} \tag{2.48}$$

$$P_{lim}^{re-}(s) = \frac{-\left(s\eta - \frac{1}{e}\right) + \sqrt{4s\alpha\eta^2\frac{P_0}{e}}}{2s\alpha\eta^2}. \tag{2.49}$$

These power limits show the clear advantage of the simplified model presented in this section, namely the fact that the resulting optimal control is a simple rule-based controller. However, it is completely defined by physical powertrain parameters and it is derived using Pontryagin's minimum principle.

The optimal control corresponding to the map shown in Fig. 2.3 is mathematically expressed as

$$P_m^o(P_d, s) = \begin{cases} \frac{\eta(\frac{\eta}{e} - s)}{2s\alpha}, & \text{if } (P_d > 0) \cap (s < \frac{\eta}{e}) \cap (P_d > P_{lim}^{bo}(s)) \\ 0, & \text{if } (P_d > 0) \cap (\frac{\eta}{e} \leq s \leq \frac{1}{\eta e}) \cap (P_d > P_{lim}^{th}(s)) \\ -\frac{s - \frac{1}{\eta e}}{2s\alpha\eta}, & \text{if } (P_d > 0) \cap (s > \frac{1}{\eta e}) \cap (P_d > P_{lim}^{re}(s)) \\ -\frac{s - \frac{1}{\eta e}}{2s\alpha\eta}, & \text{if } (P_d < 0) \cap (P_d > P_{lim}^{re-}(s)) \\ P_d, & \text{otherwise.} \end{cases} \tag{2.50}$$

Example on a Driving Cycle

The optimal control law (2.50) as a function of the power demand P_d and the equivalence factor s is applied in this section to a driving cycle,

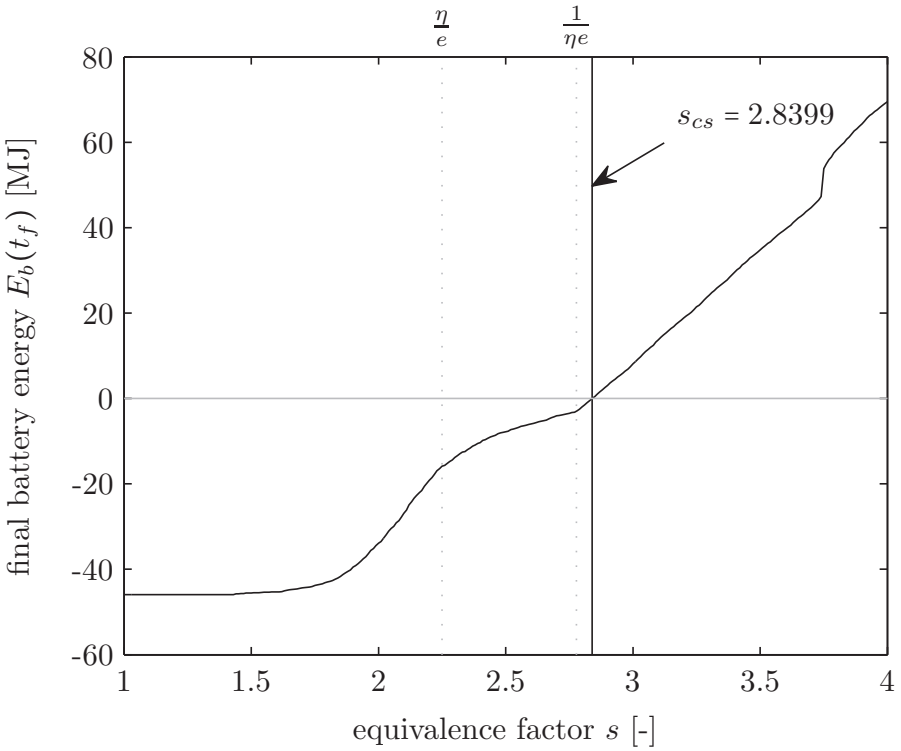

Figure 2.4: Energy in the battery E_b at final time t_f on CADC as a function of the equivalence factor s. The charge sustaining value s_{cs} is indicated by the vertical line.

namely the Common Artemis Driving Cycle (CADC) [18], see Appendix B. The remaining problem consists of finding a constant equivalence factor that guarantees the charge sustenance for the driving cycle. Figure 2.4 shows the final energy content in the battery when the optimal control law (2.50) is applied with the powertrain parameters given in Table 2.1. The charge sustaining equivalence factor is found by a root finding algorithm at $E_b(t_f) = 0$.

The shaded area in Fig. 2.5 illustrates the instances during which the engine is used to recharge the battery, with $P_m = -2187.1$ W. As stated by the optimal control law (2.50), the threshold that determines between pure electric and recharging operation is a power limit as shown in the upper graph of Fig. 2.5. The bottom part of the figure shows the speed profile and illustrates clearly that there is no speed limit deciding between electric or recharging modes.

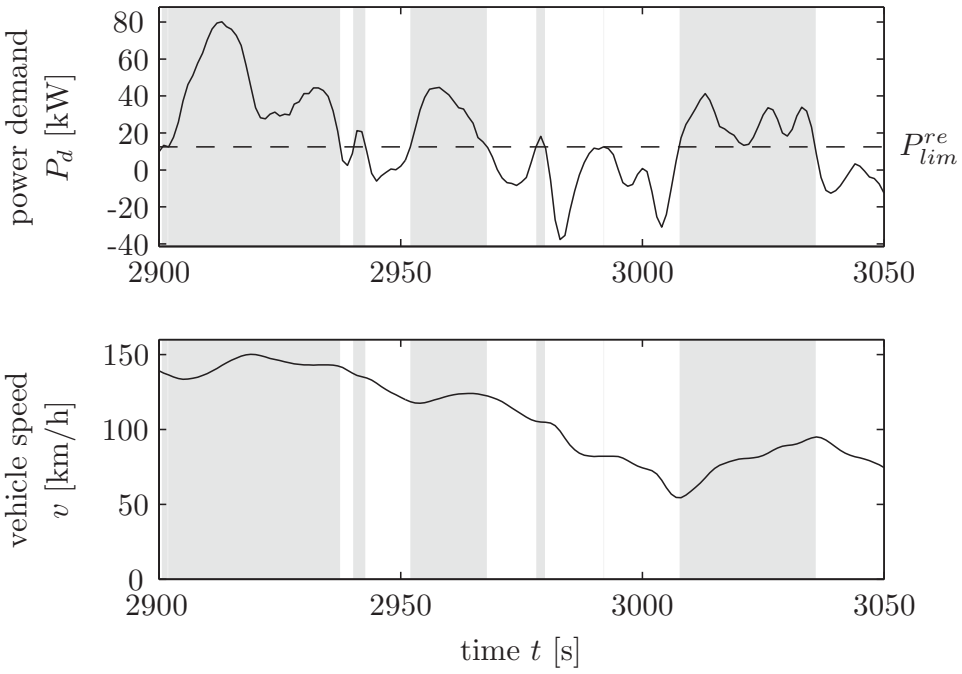

Figure 2.5: Power and speed profile $P_d(t)$ and $v(t)$ of CADC on the interval $t \in [2900,\ 3050]$ with the optimal control. Gray indicates recharging mode ($P_m = -2187.1$ W), white indicates electric mode ($P_m = P_d$).

2.1.5 Input Constrained Model

The optimal control of the simplified model presented in Section 2.1 is being extended toward a more realistic model in this section. First, input constraints, i.e., power limits on the engine and the motor are being imposed. Second, the model is extended to a time-variant model, i.e., its parameters are speed-dependent.

The only constraint in the model thus far has been that the engine cannot provide any negative power. This single input constraint is not sufficient, however. The minimum and maximum power limits of the electric motor must be considered as well as the maximum power of the combustion engine. Hence, this section extends the optimal control law in presented Section 2.1.4 with the following power constraints:

$$P_e \in [0,\ P_{emax}] \tag{2.51}$$

$$P_m \in [P_{mmin},\ P_{mmax}]. \tag{2.52}$$

As a consequence of these constraints, the power balance (2.6) cannot always be fulfilled. For example, very high power demands $P_d > P_{emax} + P_{mmax}$

Table 2.2: Power limits of the powertrain

Parameter	Value	Unit
P_{emax}	$75 \cdot 10^3$	W
P_{mmax}	$25 \cdot 10^3$	W
P_{mmin}	$-25 \cdot 10^3$	W

are infeasible. Similarly, strongly negative power demands $P_d < P_{mmin}$ are infeasible for the powertrain. However, for such strong negative power demands, the remaining braking power is assumed to be absorbed by the conventional brakes such that $P_m = P_{mmin}$.

The control P_m can now be limited to P_{mmin}, P_{mmax}, or to $P_d - P_{emax}$ indirectly by the engine. Hence, the optimal control that minimizes the Hamiltonian is not only a function of s, but also of the constraints being active. The power limits shown in Fig. 2.3 that separate the different operating modes are now extended with additional limits due to the constraints. Figure 2.6 shows an example of the new power limits for a powertrain with the parameters listed in Table 2.1 and Table 2.2. Note that this is only an example and that there will be other active power limits if the parameters change. Figure 2.6 shows that the number of power limits and the number of regions with different operating modes have increased. The power limits that are added to the previous limits (2.46)–(2.49) are $P_{emax} + P_m^{bo}(s)$, P_{emax}, $P_{emax} + P_m^{re}(s)$, $P_{emax} + P_{mmin}$, P_{mmax}, P_{mmin}, $P_{lim}^{re,m}(s)$, and $P_{lim}^{re,m-}(s)$. These power limits are derived analogously to the limits (2.46)–(2.49). The regions in Fig. 2.6 are also separated by the two new equivalence factor limits $s_{lim}^{bo,m}$ and $s_{lim}^{re,m}$. The equations for the power limits $P_{lim}^{re,m}(s)$ and $P_{lim}^{re,m-}(s)$ are given in (C.6) and (C.9) respectively. The equations for the equivalence factor limits $s_{lim}^{bo,m}$ and $s_{lim}^{re,m}$ are given in (C.2) and (C.4). These equations are explained further in Appendix C.

All new power limits that result from including the constraints on the engine and motor must be calculated for determining the optimal control at the actual operating condition. Therefore, the computational effort for determining the optimal control P_m^o from the equivalence factor s and the current power demand P_d has increased.

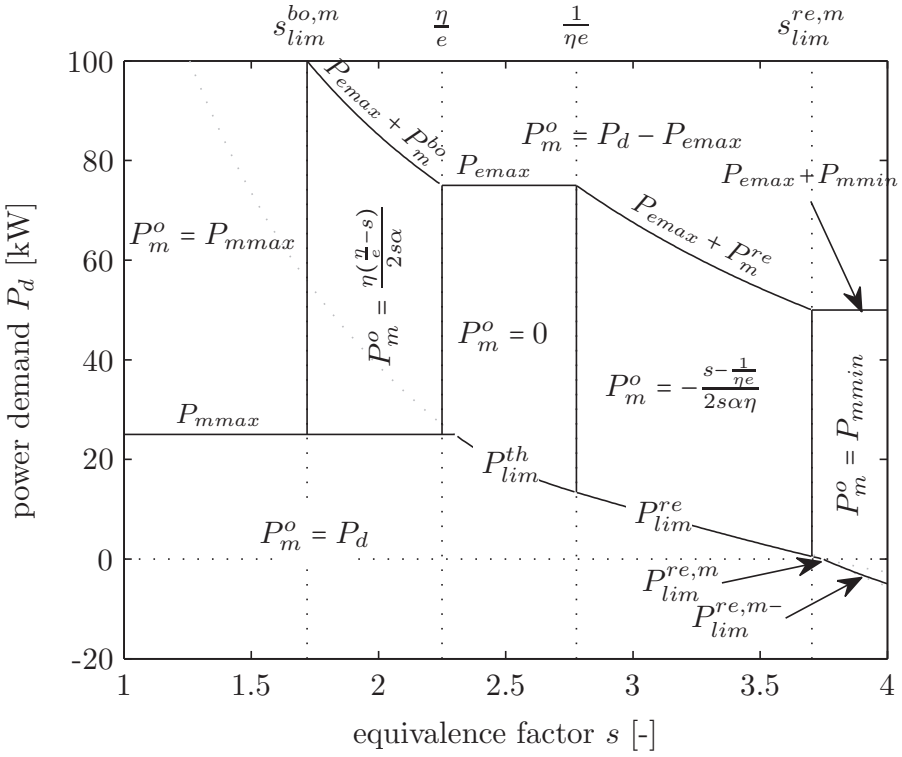

Figure 2.6: Overview of the regions with the different optimal control P_m^o (separated by solid lines) and the power limits $P_{lim}^{(.)}$ for the constrained problem.

A more efficient way of determining the optimal control P_m^o is to, as described in [15], evaluate the Hamiltonian (2.21) for the possible optimal control candidates given by

$$\mathcal{P}(P_d, s) = \{0,\ P_d,\ P_m^{bo}(s),\ P_m^{re}(s),\ P_{mmax},\ P_{mmin},\ P_d - P_{emax}\}. \quad (2.53)$$

The optimal control is then determined by evaluating the Hamiltonian for the control candidates in (2.53) and selecting the control that yields the minimum. This selective minimization of the Hamiltonian must respect the constraints (2.51) and (2.52), as well as the power balance (2.6)

$$P_m^o(P_d, s) = \underset{P_m \in \mathcal{P}(P_d, s)}{\operatorname{argmin}} \ H(P_m, P_d, s) \quad (2.54)$$

s.t.

$$P_e = P_d - P_m \quad (2.55)$$

$$P_m \in [P_{mmin},\ P_{mmax}] \quad (2.56)$$

$$P_e \in [0,\ P_{emax}]. \quad (2.57)$$

Throughout this section, the method of selectively minimizing the Hamiltonian for the optimal control candidates is referred to as selective Hamil-

tonian minimization (SHM). Note that, for many operating conditions, a careful implementation of the SHM can utilize the constraints (2.55)–(2.57) in order to minimize the feasible candidates in $\mathcal{P}(s)$. It is therefore possible to reduce the computational effort to perform the minimization (2.54).

Example on a Driving Cycle

When the power constraints in the engine and motor are included, the method of finding the charge sustaining equivalence factor is the same as in Section 2.1.4, i.e., a root finding algorithm is used. Note that the initial guess of the algorithm must be larger than $s_{lim}^{bo,m}$ since below this equivalence factor the operating modes do not change and the final energy in the battery is constant. The charge sustaining equivalence factor for CADC is slightly different when including the constraints $s_{cs} = 2.8463$ compared to the unconstrained case $s_{cs} = 2.8399$ because of the new regions shown in Fig. 2.6.

Figure 2.7 shows a section of the optimal charge-sustaining control for the CADC where four different modes can be observed. These modes are recharging $P_m = -2409.0$ W, electric driving and recuperation $P_m = P_d$, maximum recuperation $P_m = P_{mmin}$, and boosting or recharging limited by the engine $P_m = P_d - P_{emax}$. This figure clearly shows that the different operating modes are separated by power limits (top graph) and not by speed limits (bottom graph).

2.1.6 Input Constrained, Speed Dependent Model

The model described in Section 2.1.5 does not depend on the rotational speed of the crankshaft. In reality, however, several component parameters are speed-dependent. This section investigates a modified version of the model given by equations (2.6)–(2.9) including the input constraints (2.51) and (2.52), where e, P_0, and P_{emax} are replaced by $e(\omega)$, $P_0(\omega)$, and $P_{emax}(\omega)$, respectively.

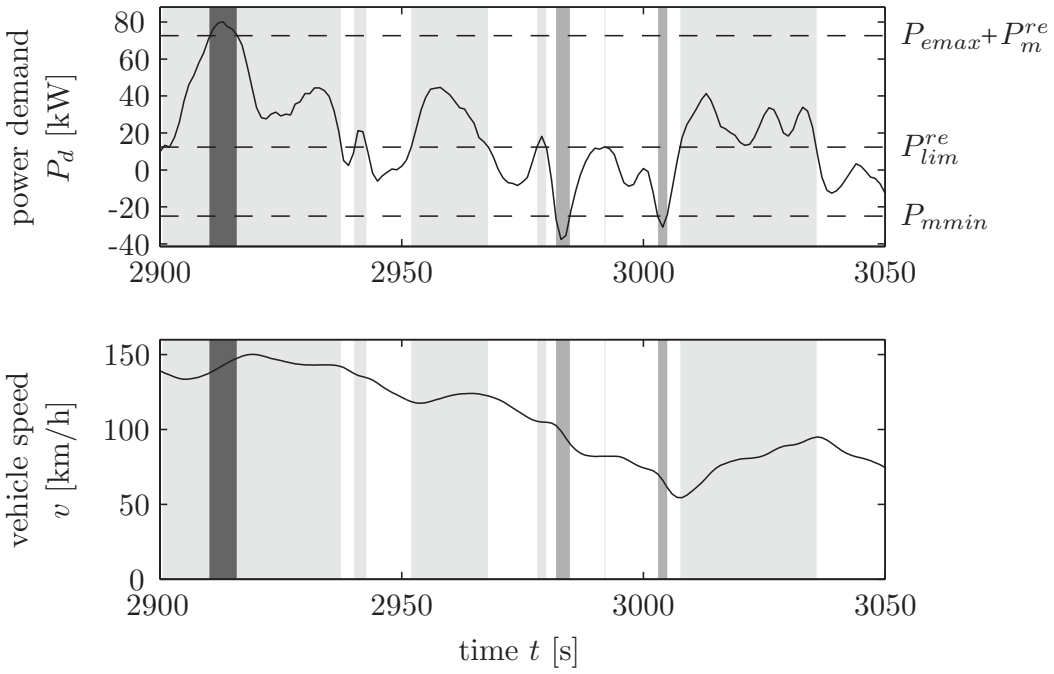

Figure 2.7: Power and speed profile $P_d(t)$ and $v(t)$ of CADC on the interval $t \in [2900, 3050]$ with the optimal control. Light gray indicates recharging mode ($P_m = -2409.0$ W), medium gray indicates maximum recuperation ($P_m = P_{mmin}$), dark gray indicates boosting or recharging limited by engine ($P_m = Pd - P_{emax}$), and white indicates electric mode ($P_m = P_d$).

In the electric path, only the parameters of the electric motor are speed-dependent, strictly speaking. This would result in the parameters $\eta(\omega)$, $P_{mmax}(\omega)$, and $P_{mmin}(\omega)$. The battery characteristics are indeed not speed-dependent. However, the parameter α, which captures nonlinearities in the battery, can also be used to capture the nonlinearities in the electric motor. Consequently, the entire electric path is integrated in the parameters $\eta(\omega)$, $\alpha(\omega)$, $P_{mmax}(\omega)$, and $P_{mmin}(\omega)$.

The speed-dependent model is finally obtained by fitting the parameters of the simplified, speed-independent model to measured data for a set of rotational speeds. The following data of a real powertrain are typically available to fit the speed-dependent model:

- A stationary fuel consumption map of the engine as a function of the rotational speed and the torque,
- the maximum torque curve of the engine,

- the idle speed of the engine,
- a stationary electric consumption map of the motor as a function of the rotational speed and the torque,
- the maximum and minimum torque lines of the motor,
- the open circuit voltage and the inner resistance curves for charging and discharging of the battery as a function of the state-of-charge.

Measured-Data Model

In order to evaluate the simplified model introduced Section 2.1.5 using speed-dependent parameters versus the real powertrain, an extended model relying on the measured data of the powertrain is used. This model is referred to as the *original model* in throughout this section. It is being used instead of the real powertrain since a prototype is not available at this stage.

The modeling approach follows common approaches such as those described by [19] and [20]. These models assume that the speeds and the accelerations are kept constant over each sampling interval. Such models are known as *quasi-static* models. This assumption has been verified for engines of passenger cars by [21]. It is obvious that this assumption is also valid for electric machines because the time constants of the electric components are very small compared to the dynamics of the powertrain speed. An overview of a quasi-static model is shown in Appendix A. The model used in this section relies on a fuel consumption map for the combustion engine and a electric power map for the electric motor. The battery model is based on an equivalent circuit model as shown in Appendix A. The parameters for the battery model is based on measurements of a Li-Ion battery.

Fitting of Speed Dependent Parameters

The speed-dependent parameters of the simplified model are evaluated for each rotational speed such that the sum of the absolute errors between

the simplified model and the original model is minimized. Such a fit is shown in Fig. 2.8 for $\omega = 1000$ rpm and $\omega = 3000$ rpm. It clearly shows that the engine can be well approximated with an affine function and that the electric path is well described by a piecewise quadratic function.

The resulting speed-dependent parameters for the simplified model are shown in Fig. 2.9, while the corresponding efficiency maps are shown in Figs. 2.10 and 2.11. The peak efficiency in Fig. 2.10 is very high for an SI engine. This is a consequence of the affine approximation that tends to underestimate the fuel consumption at high loads due to enrichment.

Optimal Control

Using the speed-dependent model, the derivation and the solution of the optimal control problem stated in (2.6)–(2.13) do not change from those using the speed-independent model above. The optimal control policy given in (2.54) is still optimal when speed-dependent parameters are used. However, the power limits are now dependent on the rotational speed and thus the different regions shown in Fig. 2.6 vary with the rotational speed. Therefore, the regions defining the optimal control increase by one dimension, namely the speed ω. Figure 2.12 shows the regions for the charge-sustaining equivalence factor for CADC. In order to improve readability, this figure is expressed with torque values instead of power.

2.1.7 Model Validation

In this section, the simplified model (2.6)–(2.9) with the speed-dependent parameters shown in Fig. 2.9 and the constraints (2.51)–(2.52) is validated by the original model in Section 2.1.6. The validation is carried out by application of a feedforward control signal to both models. Both the state trajectory $E_b(t)$ and the cost functional $E_f(t)$ are being compared for three driving cycles. The driving cycles used in this section are the CADC, the New European Driving Cycle (NEDC), and the Federal Test Procedure 72 (FTP72). The feedforward signal applied here is the charge-sustaining optimal control signal evaluated for the simplified model. The charge-

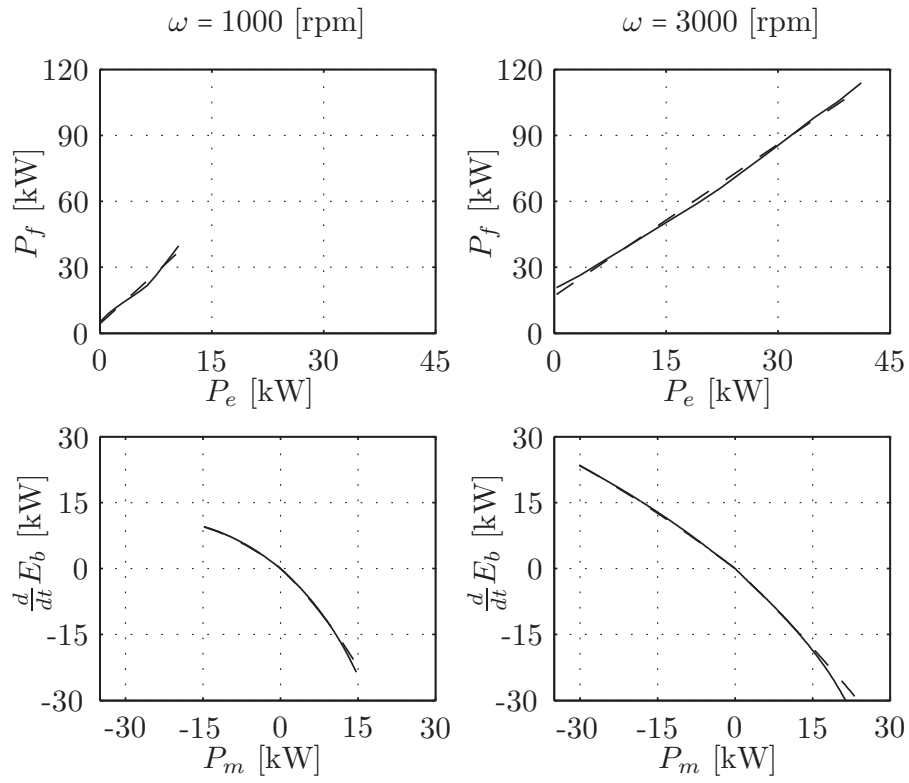

Figure 2.8: Characteristics of the engine (top) and the electric path (bottom) for two selected speeds for the original model (solid) and the fitted simplified model (dashed).

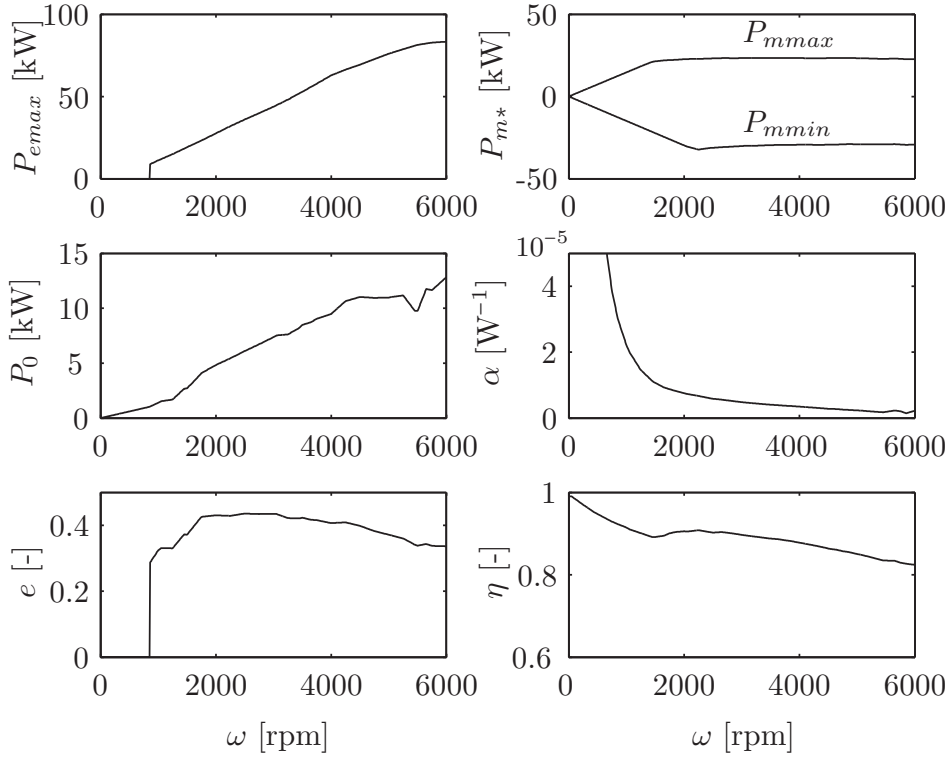

Figure 2.9: Parameters of the simplified, speed-dependent model of the parallel propulsion system.

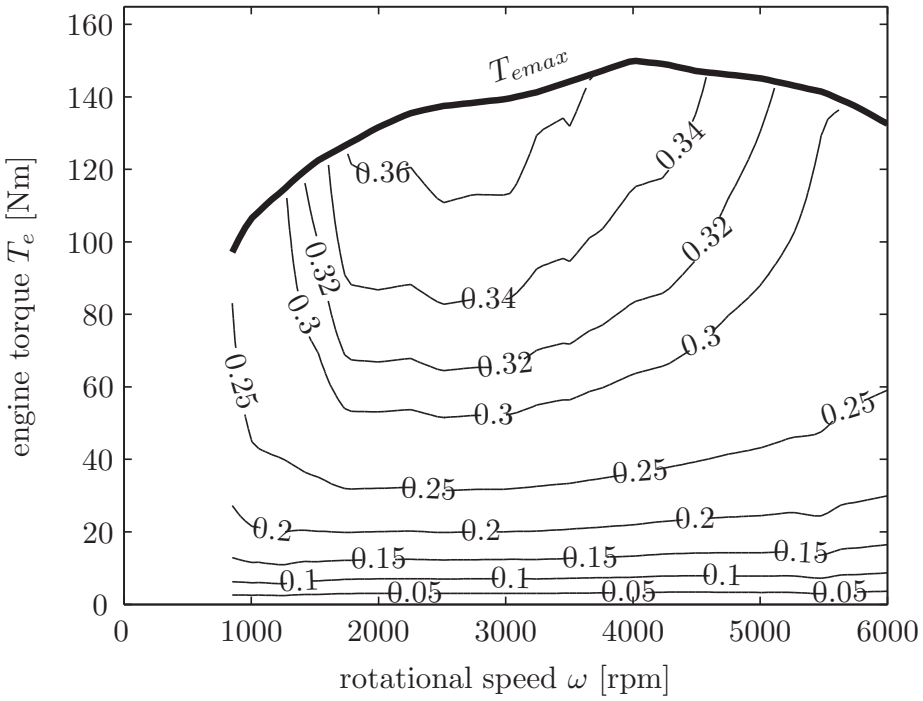

Figure 2.10: Engine map of the simplified, speed-dependent model with iso–efficiency and peak torque lines.

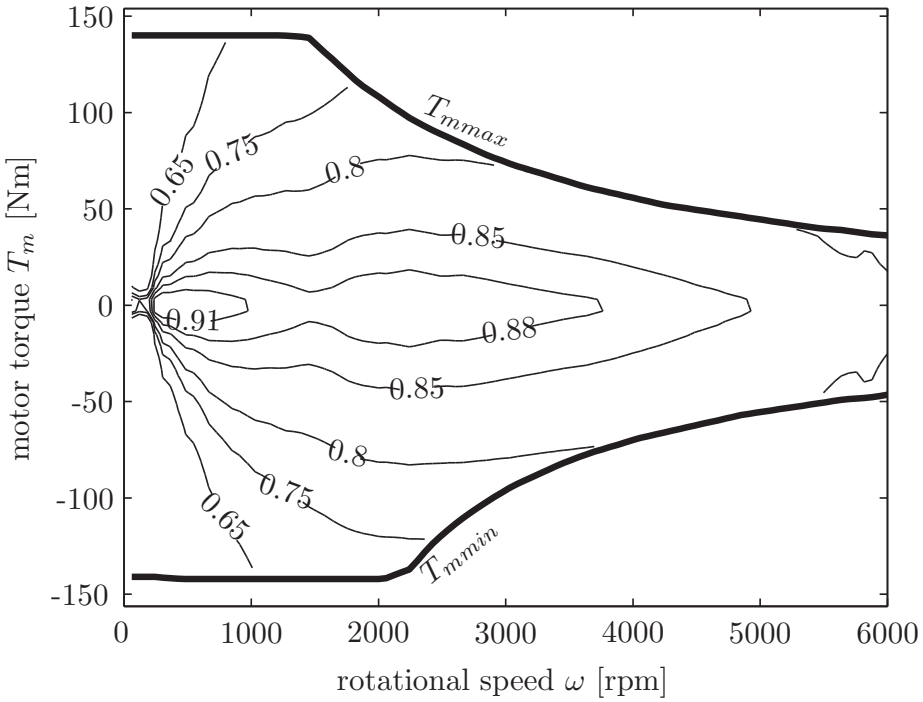

Figure 2.11: Efficiency map of the electric path of the simplified, speed-dependent model. The efficiency includes electric motor and battery.

sustaining optimal control for the CADC is shown in Fig. 2.12. Figure 2.13 shows the state trajectory $E_b(t)$ and the cost functional $E_f(t)$ of both models for the CADC. Note that the models are actuated with the same signal. Both trajectories match very well and justify the simplifications adopted when the simplified model was formulated from the original model.

The relative deviations of the two models for both signals at the final time t_f are defined as

$$\epsilon_{ff,E_b} = \frac{E_{b,orig}(t_f) - E_{b,simp}(t_f)}{\int_0^{t_f} |\dot{E}_{b,orig}(\tau)| d\tau} \tag{2.58}$$

$$\epsilon_{ff,E_f} = \frac{E_{f,orig}(t_f) - E_{f,simp}(t_f)}{E_{f,orig}(t_f)}. \tag{2.59}$$

Table 2.3 shows that the final energy content of the battery $E_b(t_f)$ as well as the final fuel energy use $E_f(t_f)$ of the simplified model fit the original model well. The largest error, i.e., the error in the final energy content ϵ_{ff,E_b} for NEDC, is 1.6%.

Note that the error in the final state ϵ_{ff,E_b} cannot be separated from the error in the cost functional ϵ_{ff,E_f} since a surplus in final battery energy $E_b(t_f)$ could have been used to lower the fuel energy $E_f(t_f)$. Therefore, in order to compare the error in fuel consumption only, the two simulations carried out must have identical initial and final battery energy levels. This is achieved by first obtaining the fuel consumption by simulating the original model with the feedforward $P^o_{m,simp}$ derived for the simplified model. This fuel consumption is the compared to the optimal fuel consumption having identical initial and final battery energy levels. The optimal fuel consumption for the original model is found by means of dynamic programming [22, 23]. The dynamic programming algorithm has been implemented using the ideas introduced by [24]. The difference in fuel consumption between these two simulations reveals the losses introduced by using a simplified model for the evaluation of the control. This excess in fuel consumption is expressed as

$$\epsilon_{ff/dp} = \frac{E^{ff,simp}_{f,orig}(t_f) - E^{dp}_{f,orig}(t_f)}{E^{dp}_{f,orig}(t_f)}. \tag{2.60}$$

These increases in fuel consumption are shown in Table 2.4. Note that the simplified model is state independent while in the original model the

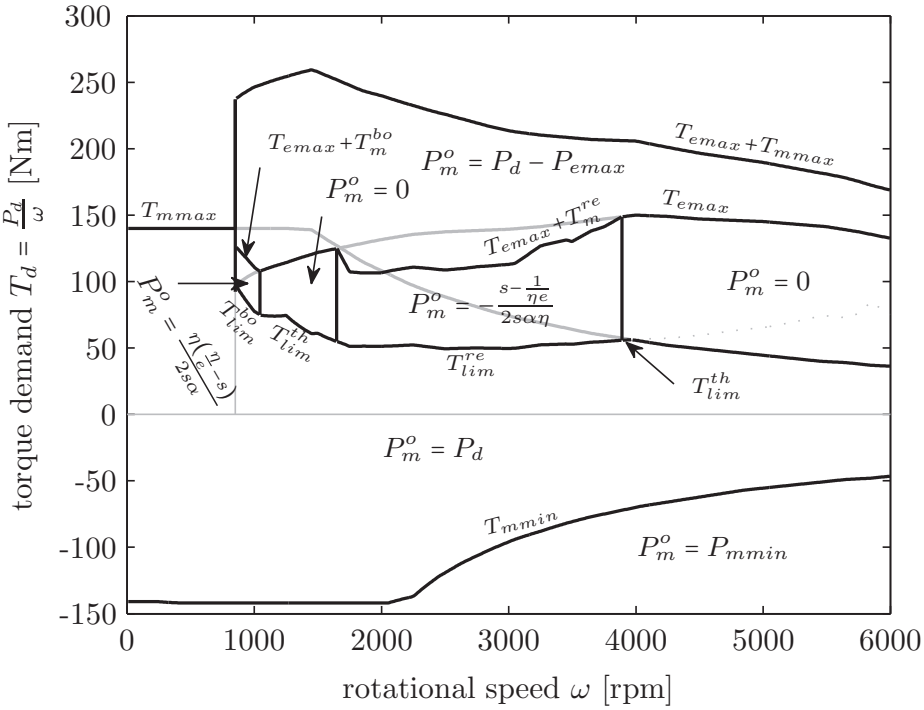

Figure 2.12: Overview of the regions with the different optimal control P_m^o (separated by solid lines) for the constrained, speed-dependent problem. The regions are represented for the charge-sustaining equivalence factor s_{cs} for CADC as a function of gearbox speed ω and torque T_d.

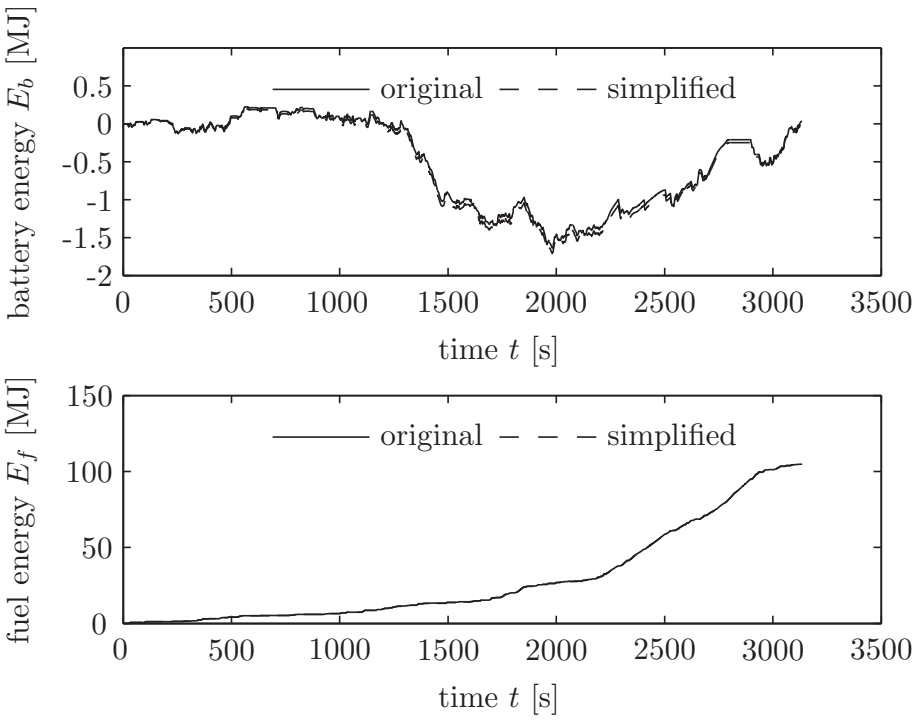

Figure 2.13: Signals for the simplified and original models when using the optimal control determined using the simplified model for the CADC. The upper graph shows the state trajectory E_b, while the lower graph shows the fuel energy E_f.

Table 2.3: Validation of the simplified model versus the original model.

Variable	CADC	NEDC	FTP72
ϵ_{ff,E_b}	0.2%	1.6%	1.1%
ϵ_{ff,E_f}	0.2%	0.7%	1.0%

Table 2.4: Increased fuel consumption due to simplified model for control.

Variable	CADC	NEDC	FTP72
$\epsilon_{ff/dp}$	0.8%	1.2%	1.5%

battery is dependent on the state. A large deviation of the state will therefore increase the error between the models. Part of the error $\epsilon_{ff/dp}$ in Table 2.4 is a consequence of the relatively large state deviations $E_b(t)$ when applying $P^o_{m,orig}$. The solution from dynamic programming accounts for the state dependencies of the original model and reduces the state deviation.

2.1.8 Application of Simplified Model

The simplified, speed-dependent model which was validated in Section 2.1.7 can be used for energy management in a real vehicle. The control of the powertrain at each time sample is then evaluated by the following algorithm:

1. Read the requested power P_d and the actual speed ω.
2. Evaluate the speed-dependent parameters for the rotational speed ω.
3. For a given s, evaluate the control P^o_m that minimizes the Hamiltonian according to (2.54).
4. Apply P^o_m to the electric motor and $P_d - P^o_m$ to the engine.

The constant equivalence factor must be found such that charge sustenance is achieved for the given driving cycle as described in Section 2.1.4. Such a controller cannot be realized because it relies on future information, i.e.,

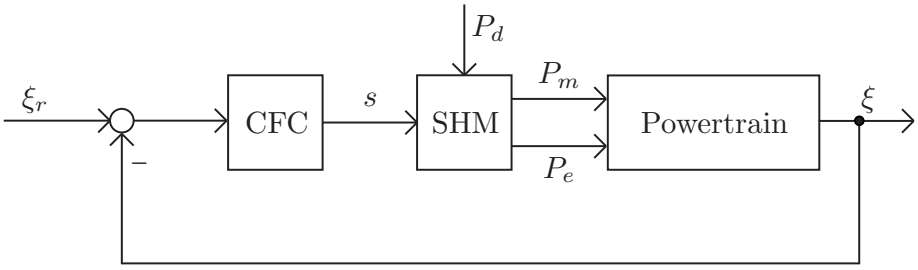

Figure 2.14: Schematic of the control loop including the causal feedback controller (CFC), the selective hamiltonian minimization (SHM), and the powertrain.

it is non-causal. However, suboptimal approaches can be taken to render the control causal.

Causal Feedback Control

A causal controller evaluates an appropriate equivalence factor using only information of the past and the present. Many approaches have been presented in literature [12, 25, 26, 27]. These approaches commonly rely on controlling the state-of-charge ξ to some reference value ξ_r by the equivalence factor s. For this investigation, the (causal) equivalence factor is computed as in [27] by

$$s(t) = 2.8 + 1197 \cdot (\xi_r - \xi(t))^3 + \int_0^t \frac{\xi_r - \xi(\tau)}{100} d\tau. \tag{2.61}$$

The numeric values in this expression are computed with the tuning parameters used by [27] together with the battery capacity $Q_0 = 6.2$ Ah, the open circuit voltage $V_{oc}(\xi = 0.6) = 300$ V, and the reference state-of-charge $\xi_r = 0.6$.

Anti-Windup

The causal feedback control (CFC) given by (2.61) contains an integral part to avoid static errors. This integral part can lead to undesired behavior, called *wind-up* of the integrator, if the controller output is saturated [28]. The controller for this consideration is only the function (2.61) with

$\xi_r - \xi(t)$ being the controller input and $s(t)$ being the controller output as schematically shown in Fig. 2.14. For equivalence factors s being less than $s_{lim}^{bo,m}$ (C.2), the control of the powertrain is independent of the equivalence factor as it can be seen in Fig. 2.6. Hence, the controller output $s(t)$ is saturated for $s < s_{lim}^{bo,m}$. For very high values of $s(t)$, such a saturation does not occur because the power limit $P_{lim}^{re,m-}$ converges for $s \to \infty$ to the minimum power limit of the motor P_{mmin}. This means that for $s > s_{lim}^{re,m}$, there is always more recharging of the battery for larger values of s. Consequently, an anti-windup scheme is implemented with a saturation of $s(t) \in [s_{sub},\ \infty)$, where

$$s_{sub} = \min_{\omega} s_{lim}^{bo,m}(\omega) = \min_{\omega} \frac{\eta(\omega)^2}{e(\omega)\left(2P_{mmax}(\omega)\alpha(\omega) + \eta(\omega)\right)}. \tag{2.62}$$

Example on a Driving Cycle

The causal controller relying on the simplified model is finally applied on the original model. To benchmark its performance, the optimal solution having the same initial and final conditions as the causal controller $E_{b,orig}^{fb,simp}(t_f) = E_{b,orig}^{dp}(t_f)$ is found using dynamic programming. The relative excess fuel consumption is expressed by

$$\epsilon_{fb/dp} = \frac{E_{f,orig}^{fb,simp}(t_f) - E_{f,orig}^{dp}(t_f)}{E_{f,orig}^{dp}(t_f)} \tag{2.63}$$

and is shown in Table 2.5.

The state trajectories resulting from applying the simplified model for causal control of the original model are shown in Fig. 2.15 for the CADC. The figure also shows the optimal state trajectory determined using dynamic programming.

The sub-optimality of the control can be explained by two effects. First, the model used to evaluate the control is simplified, i.e., it does not perfectly represent the real plant. This effect is investigated in Section 2.1.7. Second, the causal controller cannot take into account any future information on the driving cycle. In contrast, the optimal solution from dynamic programming fully exploits information on the driving cycle.

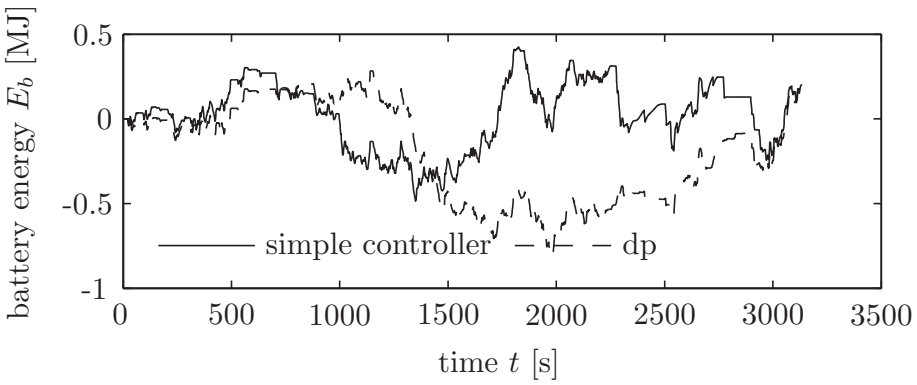

Figure 2.15: State trajectory resulting from applying the simplified model for causal control of the original model (solid), and the state trajectory using DP on the original model (dashed) for CADC

Table 2.5: Relative fuel excess consumption using the simplified model for control of original model

Variable	CADC	NEDC	FTP72
$\epsilon_{fb/dp}$	1.1%	1.7%	1.7%

However, the causal controller given by (2.61) and (2.53)–(2.57) with the speed-dependent parameters shown in Fig. 2.9 is computationally cheap and simple to implement. The controller also achieves results which are within 1.7% from the global optimum for three various driving cycles.

2.2 Control of a Torque-Assist Parallel Hybrid

In this section a torque-assist parallel hybrid equipped with a dual-clutch transmission is studied. The methods of deriving the optimal control for a full hybrid, described in the previous section, can of course also be used for a torque-assist hybrid. However, the approach for designing the energy management strategy in this section is closely linked with the process of finding the optimal design of the torque-assist hybrid. In other words, the strategy proposed in this section is an extension to the simple sizing law for a torque-assist parallel hybrid presented in Chapter 3.

In the literature the gearbox is not always considered when developing energy management strategies. However, in [29], [30], and [31] the gear shifting or crankshaft speed is optimized along with the instantaneous power-split in order to minimize fuel consumption. What is more, the number of gear ratios in the gearbox is, in conventional vehicles, typically optimized for drivability and extreme conditions. Such conditions can be an uphill vehicle launch with a trailer or low-speed driving in a traffic jam. In hybrid vehicles, the gearbox can be optimized for fuel consumption since the electric motor can compensate for torque fluctuations and torque deficits during gearshifts [32]. In this section the proposed energy management strategy is therefore applied to different number of gear ratios in the gearbox.

The focus of this section is to develop an energy management strategy which considers the gear shifting strategy and have low computational requirements, good scalability, and low fuel consumption. Furthermore, the proposed energy management strategy is a combination of the rule-based and the model-based optimal control strategies. The computational load is therefore reduced while maintaining a satisfactory scalability and fuel consumption.

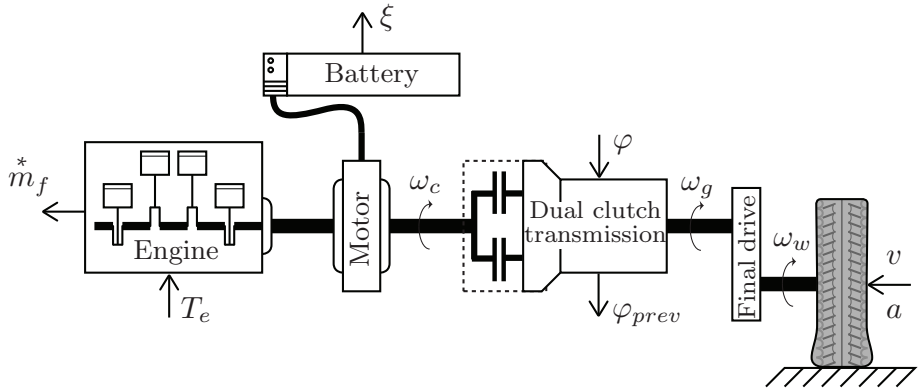

Figure 2.16: Signal flow of the torque-assist parallel hybrid configuration including a dual clutch transmission.

2.2.1 Hybrid Vehicle Model

The vehicle model in this section is based on a midsized vehicle with the mass of $m_v \approx 1660$ kg. The hybrid vehicle model in this section is slightly different than the model in Appendix A. Since the gearbox is a dual-clutch transmission and the gear number is a second input variable the model can be described as follows:

$$\boldsymbol{x}_{k+1} = F(\boldsymbol{x}_k, \boldsymbol{u}_k, \boldsymbol{w}_k) \tag{2.64}$$

where the state vector $\mathbf{x}$, input vector $\mathbf{u}$, and disturbance vector $\mathbf{w}$ are

$$\boldsymbol{x}_k = [\xi_k,\ \varphi_{prev,k}]^T \tag{2.65}$$
$$\boldsymbol{u}_k = [T_{e,k},\ \varphi_k]^T \tag{2.66}$$
$$\boldsymbol{w}_k = [v_k,\ a_k]^T. \tag{2.67}$$

where the state vector $\boldsymbol{x}$ contains the battery state-of-charge ξ_k and the previous gear number $\varphi_{prev,k}$. The input vector $\boldsymbol{u}$ contains the combustion torque $T_{e,k}$ and the new gear number φ_k. The disturbance vector $\boldsymbol{w}$ contains the vehicle speed v_k and the acceleration a_k. The input $T_{e,k}$ can be calculated from, or replaced by, the torque split factor u_s in Appendix A.6.

The basic hybrid vehicle model is explained in Appendix A. Only the model of the dual-clutch gearbox is presented in this section.

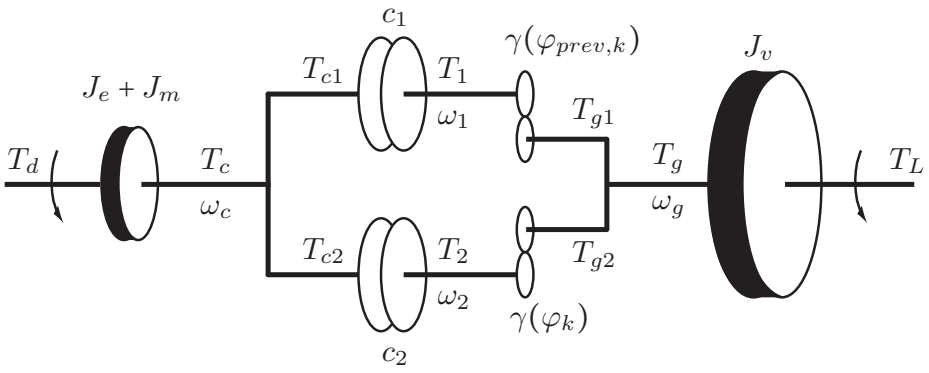

Figure 2.17: Overview of dual clutch transmission model.

2.2.2 Dual Clutch Transmission: Gear Shift

During a gear shift some energy is lost in the two clutches in the gearbox. To estimate the extra required power from the engine and/or the electric motor a simple model of the two shafts in the DCT is used. An overview of the model and the nomenclature is shown in Fig. 2.17. In [33], [34] a more detailed model of a DCT is used to optimize the shifting procedure.

In the simple model the two equations explaining the speed dynamics of the two inertias are

$$(J_e + J_m)\dot{\omega}_c = T_d + T_c \tag{2.68}$$

$$J_v\dot{\omega}_v = T_L + T_g \tag{2.69}$$

where T_d is the torque delivered by the powertrain, T_c is the gearbox input torque, T_g is the gearbox output torque, and T_L is the load torque. However, assuming that during the gear shift procedure from $\gamma(\varphi_{prev,k})$ to $\gamma(\varphi_k)$ the output speed of the gearbox ω_g does not change and that only the crankshaft speed ω_c changes results in

$$J_v\dot{\omega}_g = 0 \Rightarrow T_g = -T_L. \tag{2.70}$$

Since in a dual-clutch gearbox there are two shafts and two clutches (c_1 and c_2), the gearbox input and output torque is divided on the two shafts

$$T_g = T_{g1} + T_{g2} \qquad T_c = T_{c1} + T_{c2}. \tag{2.71}$$

Define the torque split $u_c \in [0,\ 1]$ in the gearbox as

$$u_c = \frac{T_{g1}}{T_g} = \frac{T_{g1}}{T_{g1} + T_{g2}} \tag{2.72}$$

$$T_{g1} = T_g u_c \tag{2.73}$$

$$T_{g2} = T_g(1 - u_c). \tag{2.74}$$

Since the torque on both sides of each clutch are equal, the gears $\gamma(\varphi_{prev,k})$ and $\gamma(\varphi_k)$ define the relationship between the shaft torque $T_{1,2}$ and the output torque T_g

$$T_{c1} = T_1 = \gamma(\varphi_{prev,k})T_{g1} = \gamma(\varphi_{prev,k})T_g u_c \tag{2.75}$$

$$T_{c2} = T_2 = \gamma(\varphi_k)T_{g2} = \gamma(\varphi_k)T_g(1 - u_c). \tag{2.76}$$

The gears $\gamma(\varphi_{prev,k})$ and $\gamma(\varphi_k)$ also define the relationship between the speeds of the two shafts $\omega_{1,2}$ and the speed of the gearbox output shaft ω_g

$$\omega_1 = \frac{\omega_g}{\gamma(\varphi_{prev,k})} \qquad \omega_2 = \frac{\omega_g}{\gamma(\varphi_k)}. \tag{2.77}$$

The power losses at the clutches are then

$$P_{c1} = |(\omega_c - \omega_1)T_1| = \left|\left(\omega_c - \frac{\omega_g}{\gamma(\varphi_{prev,k})}\right)\gamma(\varphi_{prev,k})T_g u_c\right| \tag{2.78}$$

$$P_{c2} = |(\omega_c - \omega_2)T_2| = \left|\left(\omega_c - \frac{\omega_g}{\gamma(\varphi_k)}\right)\gamma(\varphi_k)T_g(1 - u_c)\right| \tag{2.79}$$

where ω_c is the crankshaft speed. The total power loss is

$$\begin{aligned} P_c &= P_{c1} + P_{c2} \\ &= \left|\left(\omega_c - \frac{\omega_g}{\gamma(\varphi_{prev,k})}\right)\gamma(\varphi_{prev,k})T_g u_c - \left(\omega_c - \frac{\omega_g}{\gamma(\varphi_k)}\right)\gamma(\varphi_k)T_g(1 - u_c)\right| \end{aligned} \tag{2.80}$$

Assume the crankshaft speed changes linearly with time

$$\omega_c(t) = \left(\frac{1}{\gamma(\varphi_k)} - \frac{1}{\gamma(\varphi_{prev,k})}\right)\frac{\omega_g}{t_{gs}} \cdot t + \frac{\omega_g}{\gamma(\varphi_{prev,k})} \tag{2.81}$$

where t_{gs} is the duration of the shift procedure $t \in [0,\ t_{gs}]$. Also assume that the torque split $u_c(t)$ goes from one to zero linearly with time during the shift procedure

$$u_c(t) = \frac{t_{gs} - t}{t_{gs}} \tag{2.82}$$

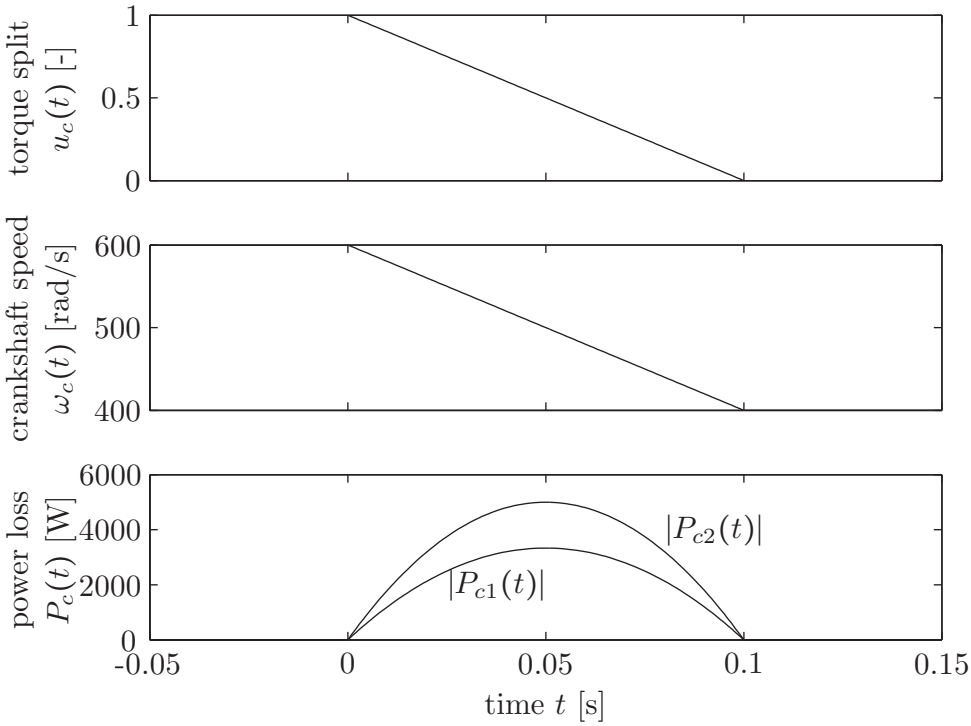

Figure 2.18: The torque split $u_c(t)$ top, the crankshaft speed ω_e middle, and the power at the two clutches $P_c(t)$ during an upshift.

The power loss as a function of time is

$$P_c(t) = \left| \frac{(\gamma(\varphi_{prev,k})^2 - \gamma(\varphi_k)^2)(t^2 - t_{gs}t)T_g\omega_g}{\gamma(\varphi_{prev,k})\gamma(\varphi_k)t_{gs}^2} \right|. \tag{2.83}$$

The total energy loss during a gear shift is

$$E_c = \int_0^{t_{gs}} P_c(t)\ dt = \frac{\left|(\gamma(\varphi_{prev,k})^2 - \gamma(\varphi_k)^2)T_g\omega_g\right| t_{gs}}{6\gamma(\varphi_{prev,k})\gamma(\varphi_k)} \tag{2.84}$$

The maximum power loss is at $t = 0.5t_{gs}$

$$P_{c,max} = \left| \frac{(\gamma(\varphi_{prev,k})^2 - \gamma(\varphi_k)^2)T_g\omega_g}{4\gamma(\varphi_{prev,k})\gamma(\varphi_k)} \right| \tag{2.85}$$

2.2.3 Dual Clutch Transmission: Model

In this section the manual transmission in Appendix A is replaced by the gearbox model presented here. The gearbox model calculates the

crankshaft rotational speed and acceleration together with the crankshaft torque based on the gearbox output speed, acceleration, torque, and desired and current gear number, φ_k and $\varphi_{prev,k}$. The gearbox efficiency is assumed to be constant for all gears $\eta_{gb} = 0.95$. The rotational speed and acceleration of the crankshaft are

$$\omega_c = \frac{\omega_g}{\gamma(\varphi_k)} \qquad \Delta\omega_c = \frac{\Delta\omega_g}{\gamma(\varphi_k)} \tag{2.86}$$

where $\gamma(\varphi_k)$ is the gear ratio of the gear φ_k. The previous gear number $\varphi_{prev,k}$ is the second state variable in the model and it is updated according to the new desired gear φ_k using

$$\varphi_{prev,k+1} = \varphi_k. \tag{2.87}$$

In order to evaluate the proposed gear shifting strategy three types of limitations on the gear shifting are used: 1) unlimited shifting without energy losses, 2) limited shifting without energy losses, and finally 3) limited shifting with energy losses. The equations for each of the three types are specified in the following list:

1) Unlimited shifting without energy losses:

The total gearbox input torque is

$$T_c = \begin{cases} T_g\gamma(\varphi_k)\eta_g^{-1}, & \text{if } T_g \geq 0 \\ T_g\gamma(\varphi_k)\eta_g, & \text{if } T_g < 0 \end{cases} \tag{2.88}$$

Since the gear shifting is independent of the current gear, the desired gear can be anyone of the gears in the gearbox

$$\varphi_k \in \{0, 1, 2, 3, 4, 5, 6\}. \tag{2.89}$$

2) Limited shifting without energy losses:

The total gearbox input torque is decided as in (2.88), but the gear shifting is limited to

$$\varphi_k \in \begin{cases} \{0,1,3,5\}, & \text{if } \varphi_{prev,k} \in \{0,2,4,6\} \\ \{0,2,4,6\}, & \text{if } \varphi_{prev,k} \in \{0,1,3,5\} \end{cases} \tag{2.90}$$

in order to model the instantaneous gear shifting between the two shafts on the DCT.

3) Limited shifting with energy losses:

During a gear shift some energy is lost in the two clutches in the gearbox. To estimate the extra required power from the engine and/or the electric motor a simple continuous-time model of the two shafts in the DCT is used. Using the gear shift model described in Appendix 2.2.2, the total energy loss during a gear shift is

$$E_c = \frac{\left|(\gamma(\varphi_{prev,k})^2 - \gamma(\varphi_k)^2) T_g \omega_g\right| t_{gs}}{6\gamma(\varphi_{prev,k})\gamma(\varphi_k)}. \tag{2.91}$$

Since the vehicle model is a discrete-time model with a time step of one second, the energy E_c contributes to an additional torque amount as follows:

$$T_{gs} = \frac{E_c}{\omega_g t_s} = \frac{\left|(\gamma(\varphi_{prev,k})^2 - \gamma(\varphi_k)^2) T_g\right| t_{gs}}{6\gamma(\varphi_{prev,k})\gamma(\varphi_k) t_s}. \tag{2.92}$$

where $\gamma(\varphi_k)$ is the new gear ratio and $\gamma(\varphi_{prev,k})$ is the previous gear ratio. The total gearbox input torque is

$$T_c = \begin{cases} (T_{gs} + T_g)\,\gamma(\varphi_k)\eta_g^{-1}, & \text{if } T_g \geq 0 \\ (T_{gs} + T_g)\,\gamma(\varphi_k)\eta_g, & \text{if } T_g < 0 \end{cases} \tag{2.93}$$

The gear shifting is also limited according to (2.90).

The energy management strategy in the hybrid vehicle decides how the torque demand is divided between the electric motor and the combustion

engine. The torque-assist parallel hybrid always drags the internal combustion engine even when the vehicle is driving purely electrically since the motor and the engine are always directly coupled. The torque balance at the crankshaft is given by (A.27) in Appendix A. The total torque T_d demanded from combustion and/or electromagnetic forces is given by (A.28). In this chapter, the electric motor torque T_m is determined by

$$T_m = T_d - T_e. \tag{2.94}$$

The electric motor torque T_m and the torque from combustion T_e are limited to

$$T_m \in [T_{mmin}(\omega_c),\ T_{mmax}(\omega_c)] \tag{2.95}$$

$$T_e \in [0,\ T_{emax}(\omega_c)] \tag{2.96}$$

where $T_{mmin}(\omega_c) < 0$, $T_{mmax}(\omega_c) > 0$, and $T_{emax}(\omega_c) > 0$.

2.2.4 Control Problem

For the considered powertrain both the input variable T_e, thus the electric motor torque through (2.94), and the gear number φ_k must be decided. The control objective throughout this section is to minimize the fuel consumption over a driving cycle

$$J = \sum_{k=0}^{N-1} \overset{*}{m}_f (\boldsymbol{u}_k, \boldsymbol{w}_k) \cdot t_s \tag{2.97}$$

by choosing the engine torque $T_{m,k}$ and the desired gear number φ_k at every time step while respecting the battery current, voltage, and state-of-charge limitations, the electric motor and combustion engine torque and speed limitations, and the limitations in the dual-clutch transmission. This section presents a suboptimal causal controller and two optimal solutions based on dynamic programming. The dynamic programming results are used as comparisons for the proposed suboptimal causal controller.

Transmission-Equilibrium Point Strategy (TEPS)

As defined in [35] the equilibrium point strategy (EPS) is defined as the torque split strategy that recuperates all the braking energy possible,

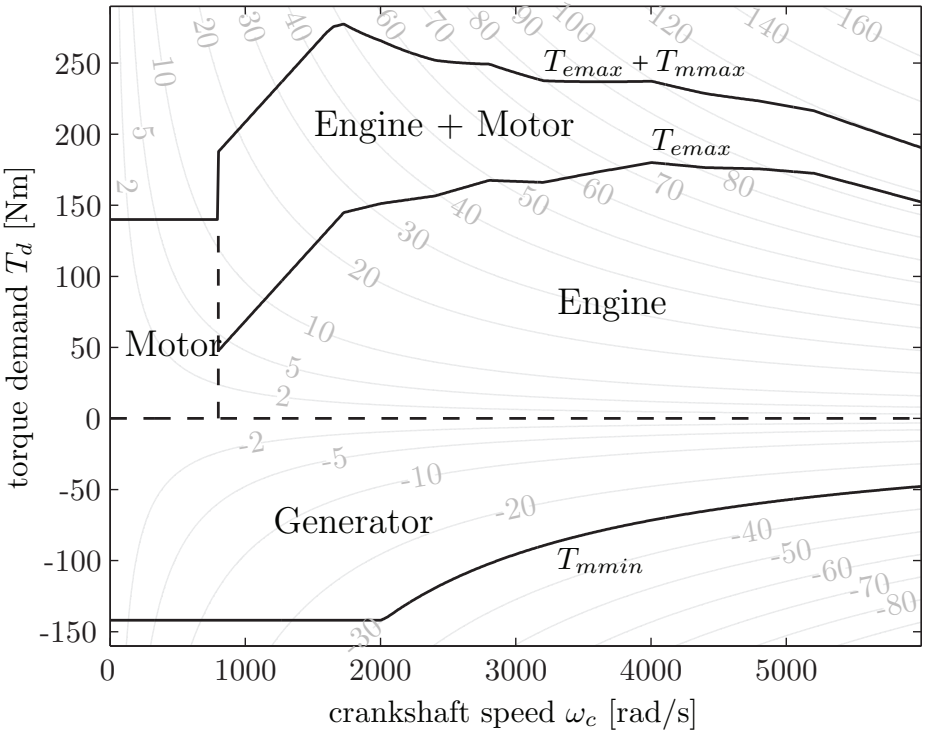

Figure 2.19: The different operating regions of the EPS for the combustion engine and the electric motor in a map showing crankshaft speed and total torque demand.

launches the vehicle from stand-still, and assists the combustion engine when it is operating at maximum load. The EPS is in other words the torque split strategy that uses the combustion engine as much as possible and the electric motor as little as possible. The equilibrium point strategy, shown in Fig. 2.19, is the simple torque split rule

$$T_e = \begin{cases} T_d, & \text{if } 0 < T_d \le T_{emax} \text{ and } \omega_c \ge \omega_{idle} \\ T_{emax}, & \text{if } T_d > T_{emax} \text{ and } \omega_c \ge \omega_{idle} \\ 0, & \text{otherwise} \end{cases} \tag{2.98}$$

$$T_m = \max(T_d - T_e,\ T_{mmin}). \tag{2.99}$$

Note that the EPS in (2.98) and (2.99) is not charge sustaining since the battery state-of-charge is not considered. However, it is shown in [35] that, using a fixed gear shifting strategy, the optimal hybridization ratio [36] of a torque-assist parallel hybrid is close to the hybridization ratio at which the EPS is charge sustaining. The focus of this section is therefore to extend the EPS with a charge sustaining element.

The proposed scheme, denoted Transmission-Equilibrium Point Strategy (TEPS), utilizes the EPS together with the gear shifting in the gearbox to control the state-of-charge in the battery. The gear choice is decided using an equivalent consumption minimization strategy (ECMS) approach [10]. In an ECMS the control is given by the minimizer of the total equivalent fuel consumption in the combustion engine and battery. Typically, in an ECMS for parallel hybrids, the control is the torque split in the vehicle. In this study, however, the control is only the gear number since the torque split is given by the EPS for any given crankshaft speed. The desired gear number φ_k is decided using

$$\varphi_k = \underset{\varphi_k \in I(\varphi_{prev,k})}{\operatorname{argmin}} \; P_f(\boldsymbol{u}_k, \boldsymbol{w}_k) + s_k \cdot P_b(\boldsymbol{x}_k, \boldsymbol{u}_k, \boldsymbol{w}_k) \tag{2.100}$$

where P_f is the fuel power used for combustion, P_b is the internal battery power, and s_k is the equivalence factor. The desired gear number must be an element of the allowed gears $I(\varphi_{prev,k})$ as defined in (2.90). Note that the fuel power P_f and the battery internal power P_b are calculated based on the EPS for a given gear number φ_k and state-of-charge ξ_k.

Since the future driving schedule is generally unknown, the equivalence factor s_k must be controlled such that the battery state-of-charge respects the boundaries for various driving cycles. There exist many controllers for the equivalence factor such as proportional controllers or integrating controllers. Moreover, prediction data can be included in the equivalence controller that is based on GPS and driving mission data [37], [38]. In this section, as in [38], the equivalence factor s_k is determined using a PI-controller

$$s_k = s_0 + \frac{t_s}{T_i} \cdot \sum_{\tau=0}^{k} (\xi_{ref} - \xi_\tau) + \frac{k_p}{Q_0 V_{oc}(\xi_k)} \cdot (\xi_{ref} - \xi_k). \tag{2.101}$$

Using the necessary assumptions, the proportional part of the controller can be derived using optimal control theory and by the instantaneous minimization of the Hamiltonian using a quadratic penalty on the state-of-charge deviation from a reference value [38]. The integrator part of the controller is added to compensate for modeling errors. The benefit of the proposed controller is that both the gear choice and the torque split are considered. Furthermore, the proposed controller only selects the gear among those possible, that minimizes the equivalent fuel consumption

(2.100). The advantage of this approach is that the control is inherently discrete with a low number of possibilities. Compared to controllers which also need to find the minimizer for the continuous torque split, the computational burden is therefore reduced when solving (2.100).

2.2.5 Comparisons

In this section the proposed controller is compared to two types of optimal controllers optimal toque-split/standard shifting and optimal torque-split/optimal shifting. The two types of optimal controllers are explained in the following list:

1) Optimal torque split/optimal gear shifting (OO):

To determine the global optimal solution the dynamic programming algorithm is used to decide both the torque split through $T_{m,k}$ and the gear choice φ_k. This is done in order to evaluate the proposed controller with respect to the lowest achievable fuel consumption.

2) Optimal torque split/standard gear shifting (OS):

To highlight the importance of the proposed controller a standard gear shifting strategy is used together with an global optimal torque split (determined by a single-state single-input dynamic programming algorithm). The standard gear shifting strategy is shown in Fig. A.1. It is a simple speed dependent strategy reflecting a normal driver's behavior. The focus is not on finding an optimized rule-based strategy, but rather on providing a strategy sample which can be used for comparisons. The gray dots in Fig. A.1 show the gear shifting in the New European Driving Cycle (NEDC). The NEDC shifting is similar to the standard shifting strategy represented by the gray boxes.

The resulting gear shifting and state-of-charge trajectories for the proposed

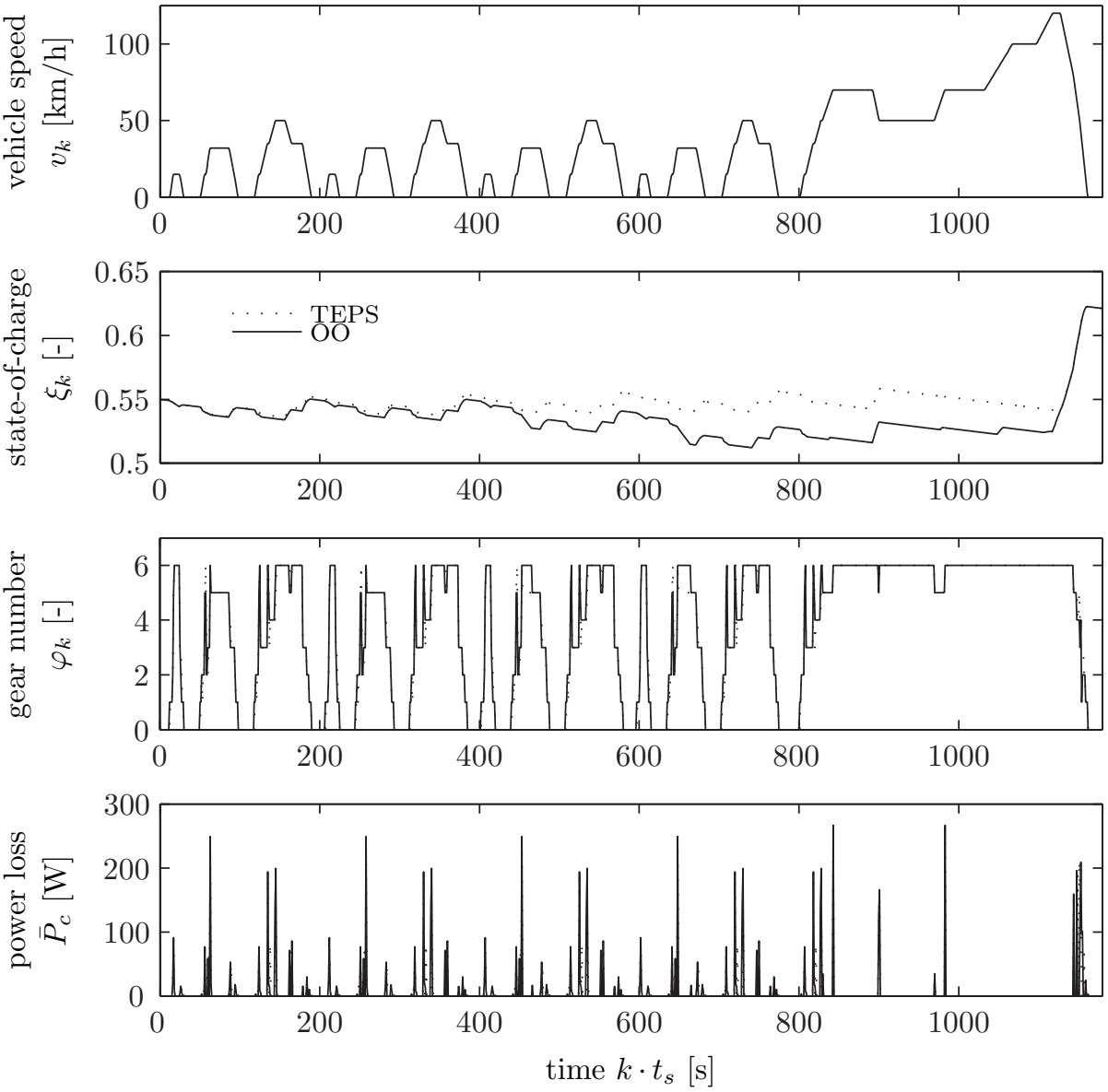

Figure 2.20: The vehicle speed v_k, the state-of-charge trajectories ξ_k, the gear shifting trajectories φ_k, and the power loss at the two clutches $\bar{P}_c(t)$ during gear shifting.

control schemes TEPS and the globally optimal control scheme OO are shown in Fig. 2.20 for the NEDC.

Furthermore, the proposed controller is compared when using different limitations and energy losses for shifting gears (*unlimited shifting without losses*, *limited shifting without losses*, and *limited shifting with losses*). Since a causal controller cannot guarantee an exact charge sustenance for a driving cycle the following method is used for a comparison. First, the proposed causal controller is used for a given driving cycle, then the optimal controllers OO and OS are calculated to achieve exactly the same final state-of-charge as the causal strategy. The relative increase in fuel consumption (FC) from the global optimum using both optimal shifting and optimal torque split (OO) is

$$\epsilon_{OS} = \frac{FC|_{OS} - FC|_{OO}}{FC|_{OO}} \tag{2.102}$$

$$\epsilon_{TEPS} = \frac{FC|_{TEPS} - FC|_{OO}}{FC|_{OO}} \tag{2.103}$$

For all comparisons, four different driving cycles have been used. The driving cycles are shown in Fig. B.1 in Appendix B.

Study on limited gear shifting

Fast gear shifting in a DCT is only allowed from gears on one shaft to gears on the second shaft. This is done by preselecting the desired gear on the unused shaft and then quickly disengaging and engaging the two clutches such that continuous power is delivered to the gearbox output. Since the proposed controller controls the gear shifting, it is important to evaluate the sensitivity on such limitation. Furthermore, during each gear shifting energy is dissipated when the two clutches are disengaged or engaged. Therefore it is also important to investigate the influence of these energy losses on the optimality of the proposed controller.

Table 2.6 shows the relative increase in fuel consumption ϵ_{OS} and ϵ_{TEPS} for the four different driving cycles and for the three different gearbox limitation schemes. It is important to note that on the average, the proposed controller is within 0.9% of the global optimal controller, regardless of the

Table 2.6: The relative increase in fuel consumption between OS and OO (ϵ_{OS}) together with the relative increase in fuel consumption between TEPS and OO (ϵ_{TEPS}). The values are given for different driving cycles and for types of limitations on gear shifting.

driving cycle	FC increase	unlimited w/o losses	limited w/o losses	limited w/ losses
NEDC	ϵ_{OS} [%]	17.1	17.1	17.0
	ϵ_{TEPS} [%]	0.0	0.1	0.1
CADC Urban	ϵ_{OS} [%]	24.4	23.6	22.8
	ϵ_{TEPS} [%]	0.9	1.6	1.5
CADC Road	ϵ_{OS} [%]	12.8	12.3	11.9
	ϵ_{TEPS} [%]	0.6	0.8	0.8
FTP-72	ϵ_{OS} [%]	23.9	23.4	23.0
	ϵ_{TEPS} [%]	0.7	0.9	0.9
average	$\overline{\epsilon_{OS}}$ [%]	19.5	19.1	18.7
	$\overline{\epsilon_{TEPS}}$ [%]	0.6	0.9	0.8

gearbox limitation scheme. Furthermore, the proposed controller outperforms by far the OS control strategy for all cycles and limitation schemes. This emphasizes the importance of not using standard gear shifting for the considered hybrid configuration. In the following sections, the results are only evaluated on the basis of the average fuel consumption increase, $\overline{\epsilon_{TEPS}}$ and $\overline{\epsilon_{OS}}$, for all four driving cycles.

Study on hybridization ratio

In hybrid vehicles the size of the components, such as that of the engine and of the electric motor, can significantly influence the control strategy. The ratio between the maximum power of the electric motor and the maximum power of the powertrain is here referred to as hybridization ratio. The hybridization ratio is further explained in Chapter 3. Other studies focusing more on design optimization and optimal hybridization ratios are [4] and [39]. A high hybridization ratio results in a large electric path (electric motor and battery) and a small combustion engine. On the other hand, a low hybridization ratio results in a small electric path and a large

Table 2.7: The average relative increase in fuel consumption for the four driving cycles, shown for different hybridization ratios. The top figure shows the relative increase in fuel consumption for the TEPS and the bottom figure shows it for the OS scheme.

powertrain parameters ($HR/V_d/P_{emmax}/Q_0$)	FC increase	unlimited w/o losses	limited w/o losses	limited w/ losses
10%/1.9l/11kW/2.9Ah	$\overline{\epsilon_{OS}}$ [%]	18.6	18.1	17.7
	$\overline{\epsilon_{TEPS}}$ [%]	0.8	0.9	0.9
22%/1.6l/24kW/6.4Ah	$\overline{\epsilon_{OS}}$ [%]	19.5	19.1	18.7
	$\overline{\epsilon_{TEPS}}$ [%]	0.6	0.9	0.8
30%/1.4l/33kW/9.0Ah	$\overline{\epsilon_{OS}}$ [%]	19.7	19.2	18.8
	$\overline{\epsilon_{TEPS}}$ [%]	0.4	0.6	0.7

combustion engine. When the hybridization ratio is changed, the engine is sized using the displacement volume, as defined in (A.18) and (A.19), and the motor torque limits and power map are sized linearly with the maximum power. The battery capacity is related to the maximum power of the battery. The capacity is therefore scaled to match the maximum power of the electric motor. The mass of each of the components scales also with the hybridization ratio. The total vehicle mass therefore increases when the hybridization ratio is increased. However, the maximum power-to-weight ratio of the vehicle is kept constant at 68 W/kg for different hybridization ratios.

In this section, a range of hybridization ratios have been investigated, namely $HR \in \{0.1, 0.22, 0.3\}$. For the lowest hybridization ratio, the engine has a displacement of 1.9 liter, while it is 1.4 liter for the highest hybridization ratio. The maximum power of the electric motor for the lowest hybridization ratio is 11 kW and 33 kW for the highest hybridization ratio.

Table 2.7 shows the average increase in fuel consumption $\overline{\epsilon_{OS}}$ and $\overline{\epsilon_{TEPS}}$ for different hybridization ratios. The results show that the relative increases in fuel consumption between the control schemes are insensitive to the hybridization ratio. The proposed controller is therefore applicable to different levels of hybridization without compromising performance.

Study on reducing the number of gears

This section studies the number of gears in the gearbox in order to show the sensitivity of different gear configurations on the performance of the proposed controller. In this study the gear ratios have been kept constant while the possible gears have been varied. The new configurations are

$$\tilde{\gamma} \in \{\gamma_{1,3,6},\ \gamma_{1,3,5},\ \gamma_{1,2,5},\ \gamma_{1,2,4},\ \gamma_{1,3,4}\} \tag{2.104}$$

The results of the average relative increase in fuel consumption for the four driving cycles are shown in Fig. 2.21. The results are shown with the proposed strategy using the original gear configuration γ as reference. The ranges of relative fuel consumption increase for the four cycles of each gear configuration are also shown. Fig. 2.21 shows an increase of only a 2% in fuel consumption with a gearbox containing only the 1st, 3rd, and 6th gear from the original gearbox. Furthermore, the reduced gearbox $\gamma_{1,3,6}$ has less than 3% increase in fuel consumption than the *optimally* controlled original gearbox. It is important to note that with only three gears there will be drivability issues in many operating conditions. Thus, this study only shows that the number of gears can be reduced in terms of energy management and fuel consumption.

2.3 Summary and Discussion

In the first part of this chapter, the explicit solution to the optimal control problem of a simplified speed independent unconstrained full hybrid electric powertrain has been derived and studied. The solution to the optimal control problem shows how simple power limits determine the optimal operating mode in the hybrid. The unconstrained problem has been extended to the case where the electric motor and combustion engine have power constraints. The derivation of the optimal control is similar to the unconstrained case. However, there are several additional power limits deciding the optimal control.

The speed independent, constrained model has been further extended to a speed dependent model. The powertrain parameters were fitted to measured data. The explicit solution to the problem can still be determined

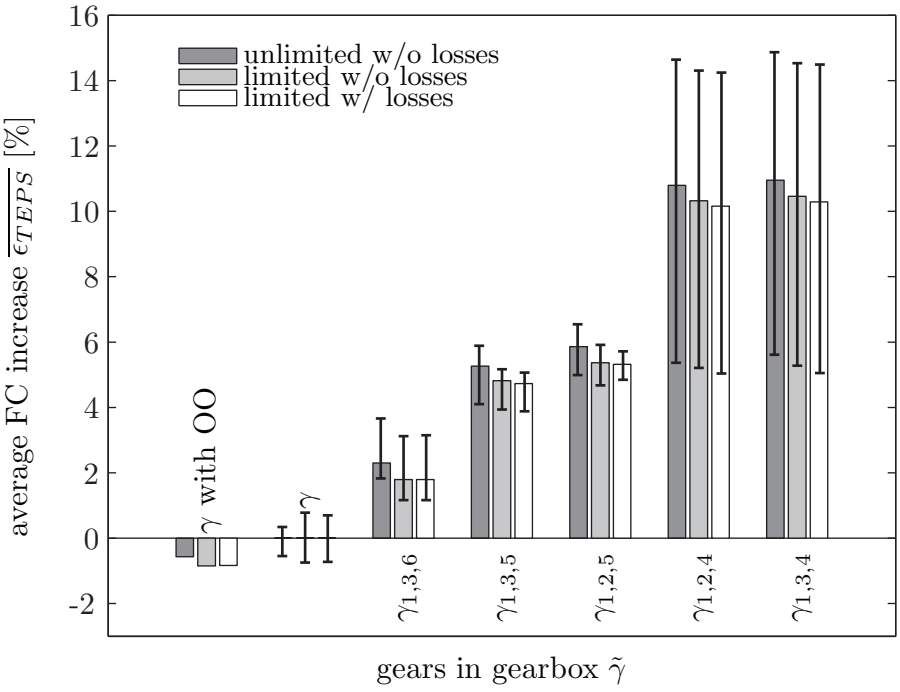

Figure 2.21: Free shifting: Increase in fuel consumption when reducing the number of gears in the gearbox compared to a 6-speed gearbox. Values are given as the average fuel consumption increase for the NEDC, CADC Urban, CADC Road, and FTP-72 driving cycles.

with several additional power limits. The charge sustaining optimal control map is shown for the CADC in terms of torque demand and rotational speed. It shows that the optimal control can be expressed as a simple rule-based map where all regions are defined by model parameters. However, a computationally cheaper method is proposed where the Hamiltonian is selectively minimized for a set of explicit optimal control candidates. The benefit of this formulation is the simple structure and the low number of possible minima.

The model has been validated using the original model that relies on measured data. A comparison of the signals of the original and simplified model by applying a feedforward signal has been carried out. It shows a maximum error of 1.6% in the final state and 1.0% in the final cost for three commonly used driving cycles. Despite the broad simplifications the model captures the most important characteristics of the original hybrid powertrain.

The simplified model is used in a causal energy management strategy,

where the equivalence factor is updated by a causal controller. When using the simplified model for causal control the fuel consumption is within 1.7% from the global optimum for three driving cycles. The simplicity and the high performance in fuel economy prove that the proposed strategy is well suited for realtime-control of parallel hybrid electric powertrains. The formulation of the simplified model further allowed to analytically derive a saturation in the equivalence factor that can be used to implement an anti-windup scheme in a causal equivalence factor controller.

The second part of this chapter shows a novel energy management strategy for a torque-assist hybrid equipped with an automatic manual gearbox. Typically, the torque split control is used for the purpose of energy management in parallel hybrid vehicles. However, a simple rule is used for the torque split control while the gear shifting strategy is used as a supervisory energy management controller to influence the battery state-of-charge. The benefit of the proposed controller is the relatively low computational requirement since an online optimization is only performed on the possible gear choices.

The proposed controller is robust with regard to different hybridization ratios. Moreover, it is also robust to the gear shifting limitations and energy losses normally present in automated manual gearboxes. Finally, the proposed control strategy can be used with a gearbox having only three possible gears while keeping the overall fuel consumption within 3% from the global optimum obtained using gearbox with 6 possible gears. The number of gears is therefore not of significant importance when the gear shifting strategy is used for energy management purposes. However, it is important to note that the 6-speed gearbox is the most efficient option and that it offers many benefits with respect to drivability.

The model is relatively simple and detailed drivability issues has not been taken into account. Additional studies on drivability issues must be performed in order to evaluate the usefulness of the proposed energy management strategy.

Chapter 3

Design of Hybrid Electric Vehicles

Designing a hybrid electric vehicle involves two major tasks: first, sizing the engine and electric components, and second, developing an energy management strategy, which decides on the power distribution between the electric motor and the combustion engine. The difficulty of this process comes from the fact that these two issues are inherently and intimately coupled. This interconnection has been emphasized in [40] for a series hybrid electric vehicle. The sizing problem includes several non-trivial constraints, such as packaging, cost, and availability limitations. The freedom of choosing component sizes is therefore restricted. The sizing problem is often solved intuitively while respecting all the constraints. The control design problem is better amenable to a systematic solution, but a good design requires that both problems are solved as well as possible. An overview of studies in the field of simulating the effects of sizing the combustion engine and electric motor is shown in [41].

There exist two main approaches to the problem of optimal control/dimensioning of hybrid electric vehicles. The first one uses a parameterized rule-based energy management strategy [42, 43, 44, 45, 46] and optimizes the strategy parameters together with the engine and electric path size for a given cycle [39, 47]. This approach allows fast evaluation of each of the configurations. It can therefore be used easily in an optimization environment that is based on evolutionary algorithms for example [48, 49]. However, due to the fact that the rule-based energy management strategy is not optimal, the various configurations cannot be evaluated on the basis of their optimal performance.

The second approach to the control/dimensioning problem is to use an optimal control approach. Since the energy management problem in a hybrid electric vehicle is nonlinear and includes both state and input constraints, the optimal control problem can be solved using a dynamic programming algorithm [22]. In [50] the authors used a simplified stochastic dynamic programming approach to optimize a fuel cell hybrid vehicle. Another approach is to use Pontryagin methods for determining the optimal control and thus the design parameters [51]. With the optimal control approach the energy management strategy is optimal for the given cycle, but the computational requirement when solving the optimal control problem is large, compared with that of a straightforward rule-based energy management strategy.

Sizing the hybrid powertrain involves finding the optimal size of the internal combustion engine, the electric motor, and the battery. The relationship between the maximum power of the powertrain and the maximum power of the electric motor can be described using the hybridization ratio [36, 39, 50, 52] which is further explained in Section 3.1.2. A similar definition of degree of hybridization is used in [53] and of hybridization factor in [54].

The first part of this chapter shows how the optimal hybridization ratios differ for the full parallel hybrid compared to the torque-assist parallel hybrid. The second part presents a computationally efficient method of determining the optimal hybridization ratio in a torque-assist parallel hybrid.

3.1 Optimal Hybridization Ratio in Parallel Hybrid Vehicles

The focus of this section is to quantify the hybridization needs, i.e. the optimal dimensioning of the power train components, in two types of parallel hybrid electric vehicles while excluding the influence of the control strategy on component sizing. The two types of parallel topologies are the torque-assist hybrid, shown in Fig. 3.1, and the full hybrid, shown in

Fig. 3.2. Note that the full hybrid requires an electrically controlled clutch between the engine.

3.1.1 Hybridization Ratio

The total maximum power of the vehicle P_{totmax} be the sum of the maximum output power levels of the two power sources

$$P_{totmax} = \max_{\omega_c} \{(T_{icemax}(\omega_c) + T_{emmax}(\omega_c)) \cdot \omega_c\} \tag{3.1}$$

where $T_{icemax} = T_{emax} - T_{e0}$ is the maximum output torque of the engine and $T_{emmax} = T_{mmax} - T_{m0}$ is the maximum output torque of the electric motor. Let

$$\omega_c^o = \arg\max_{\omega_c} \{(T_{icemax}(\omega_c) + T_{emmax}(\omega_c)) \cdot \omega_c\} \tag{3.2}$$

then the hybridization ratio, as in [36], is defined as

$$HR = \frac{P_{emmax}(\omega_c^o)}{P_{totmax}} \tag{3.3}$$

where P_{emmax} is the maximum output power of the electric motor. When optimizing the hybridization ratio in the vehicle it is only interesting to compare ratios with similar driving performance. Performance can be defined in several ways such as time from 0 to 100 km/h, steady-state top speed, and gradability. The time from 0 to 100 km/h is strongly related to the maximum power-to-weight ratio [20]. This chapter therefore compares different hybridization ratios with equivalent maximum power-to-weight ratios (≈ 68 W/kg which corresponds to $t_{0-100\text{km/h}} \approx 11.3$s).

3.1.2 Model Scaling

The combustion engine model is scaled using the displacement volume V_d according to the equations given in Appendix A. For all engine sizes the bore-to-stroke ratio is kept constant and therefore the mean piston speed for a given rotational speed changes with changing displacement. In the electric motor model the maximum torque and electric-power map

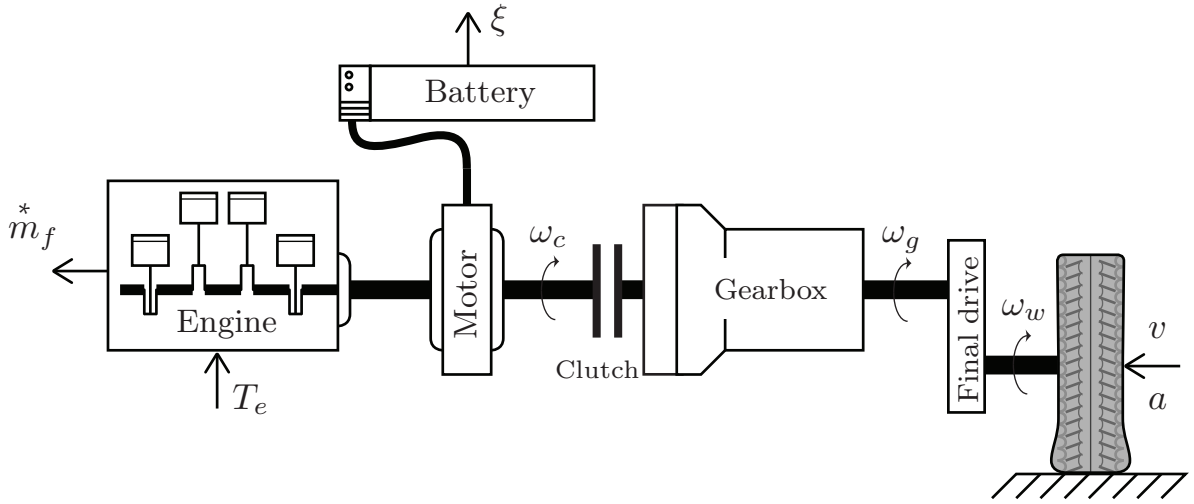

Figure 3.1: The torque-assist parallel hybrid electric vehicle configuration (including input signals and output signals).

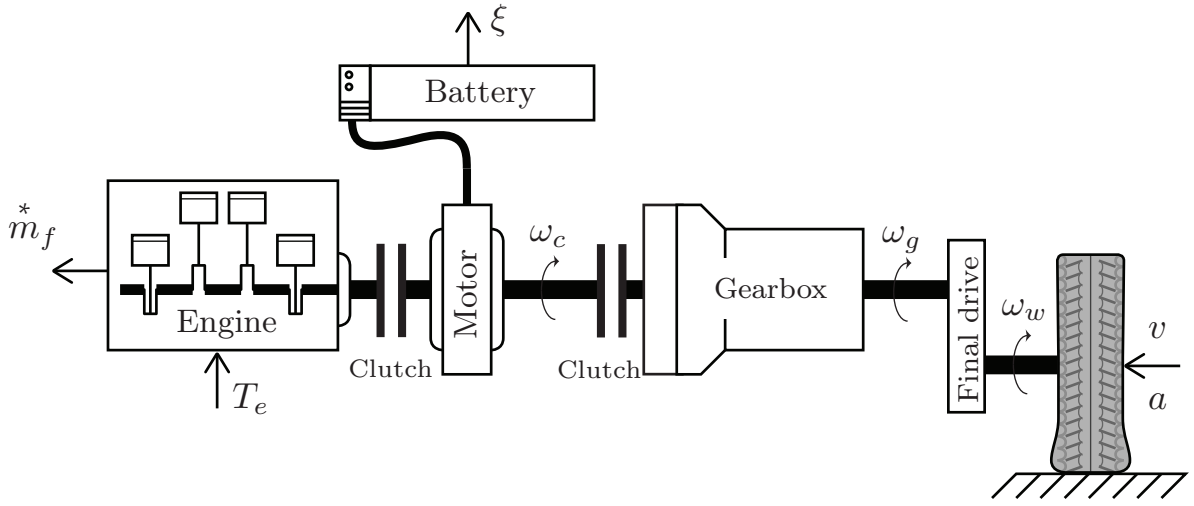

Figure 3.2: The full parallel hybrid electric vehicle configuration (including input signals and output signals).

$\Gamma(\omega_c, T_{em})$ are scaled using a linear dependency on the rated maximum power. Furthermore, the mass and inertia of the motor are also scaled using a linear relationship on the maximum power. In the battery model, the nominal open circuit voltage is kept constant while the internal resistance and battery mass are scaled based on the battery capacity. The battery is assumed to have a constant maximum-current-to-capacity ratio. The desired maximum power of the battery, given by the maximum power of the electric motor, together with the nominal voltage and the maximum-current-to-capacity ratio therefore gives the capacity of the battery. Thus, the battery capacity is scaled such that the maximum power corresponds to the maximum electric power of the electric motor.

The different vehicle characteristics for different hybridization ratios are shown in Fig. 3.4. Note that steady-state top speed v_{max}^{ice} is defined as the top speed when only the combustion engine is used. The steady-state top speed of $v_{max}^{ice} \approx 120$ km/h for a hybridization ratio of 80% is sufficient for most countries. Since the total vehicle mass is increasing with increasing degree of hybridization, the total maximum power also increases to maintain an equal power-to-weight ratio.

The gear ratio choice in the 6-speed manual gearbox is separated into two schemes: fixed gear ratios and adjusted gear ratios. When referring to fixed gear ratios the gear ratios in the gearbox are kept constant even when changing the hybridization ratio. However, since the mean piston speed changes with the hybridization ratio, keeping the gear ratios fixed is undesirable.

When referring to the adjusted gear ratios the following simple rule for choosing the gear ratios is used: the fifth gear $\gamma(5)$ is optimized for vehicle top-speed at the maximum engine speed. The sixth gear $\gamma(6)$ is chosen such that the vehicle speed is maximized when the engine speed is where the engine reaches its maximum torque. The first gear $\gamma(1)$ is chosen such that the vehicle speed at engine idle (and with a closed clutch) is constant. The remaining gears $\gamma(2) - \gamma(4)$ are chosen with a constant ratio between the gears $\frac{\gamma(j)}{\gamma(j+1)} = \mathcal{C}$. The different gear ratios for the fixed and the adjusted schemes are shown in Fig. 3.3.

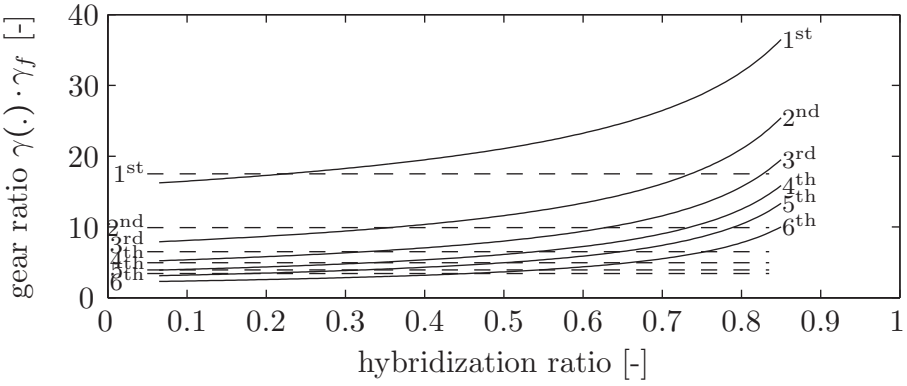

Figure 3.3: Transmission ratios of the gearbox, including the final drive, for different hybridization ratios. Fixed ratios are represented by dashed lines and adjusted gear ratios are shown with solid lines.

3.1.3 Dynamic Programming: Results

To exclude the influence of the control strategy on component sizing an optimal control method is used. By using this method all different designs are evaluated based on their optimal performance and therefore compared on an equal basis. This method has been used to determine the effect of battery size on total energy losses in a fuel cell hybrid electric vehicle by [55]. Since the considered system is highly nonlinear and is valid under multiple complex constraints Bellman's dynamic programming algorithm [22] is a suitable method to compute the optimal control input. The dynamic programming algorithm is explained in detail in Chapter 4.

When using dynamic programming for solving the energy management problem, for a given driving cycle and hybridization ratio, the results is an optimal control signal map over time and state of charge. To get the optimal state trajectory and the minimum CO_2 emission, the optimal control signal map is used to determine the torque split during a forward simulation of the vehicle for the same drive cycle. Such an optimal control signal map is shown in Fig. 3.5 for a torque-assist hybrid with 21.5% hybridization. Figure 3.6 shows the optimal control signal map for a full hybrid with 21.5% hybridization. Note that the optimal strategy is very different in the two types of hybrids. In the full hybrid there are long periods of pure electric driving (green) while in the torque-assist hybrid the engine and motor both supplies power (blue). The only time the torque-assist hybrid

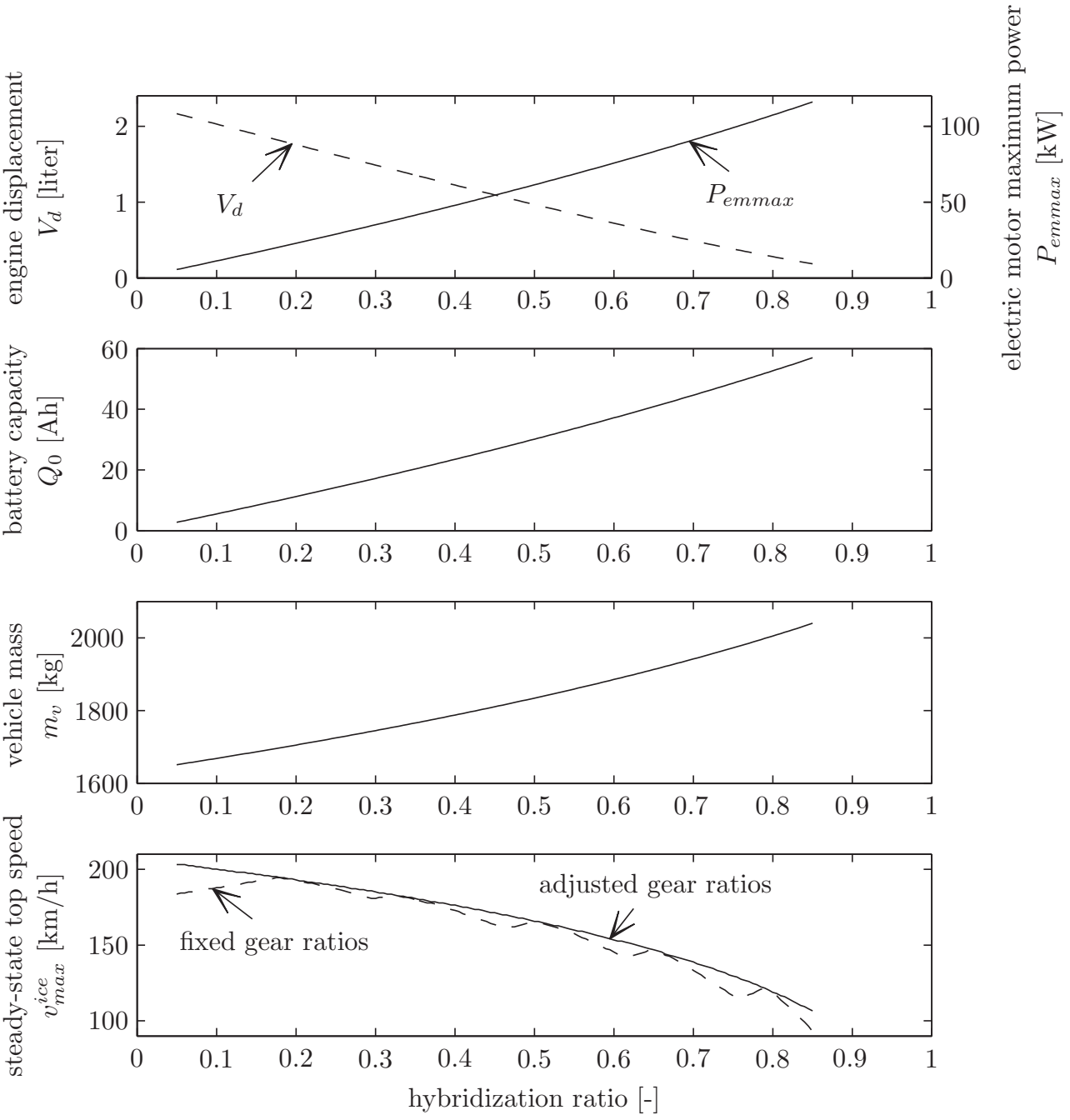

Figure 3.4: Engine displacement and motor maximum power, battery capacity, vehicle total mass, and steady-state top speed (for fixed and adjusted gear ratios) with changing hybridization ratio.

Table 3.1: Optimal hybridization ratio for the torque assist hybrid (TA^o), the full hybrid (F^o) and the difference ($TA^o - F^o$). The hybridization ratio where the full hybrid has the same CO_2 emission as the optimum of the torque assist hybrid (F_{TA^o}) and the difference ($TA^o - F_{TA^o}$)

	Hybridization Ratio (%)				
Cycle	TA^o	F^o	$TA^o - F^o$	F_{TA^o}	$TA^o - F_{TA^o}$
NEDC	59.5	52	7.5	14.4	45.1
CADC U.	62	45	17	13.3	48.7
CADC R.	56	40	16	14.5	41.5
CADC H.	45	41.5	3.5	27.9	17.1
CADC	49	41.5	7.5	19.1	29.9
HWFET	61.5	59.5	2	49.2	12.3
FTP-72	65	51	14	14.2	50.8
US06	45.5	37	8.5	20.1	25.4

is using the motor solely is during the braking and starting phases. The actual optimal input trajectory is the torque split (color) exactly on the state of charge trajectory (black line) in Fig. 3.5 and 3.6. The resulting CO_2 emission for the 21.5% torque-assist hybrid is 144.2 g/km and for a full hybrid with the same hybridization is 109.2 g/km which is approximately 24% less.

3.1.4 Comparison Between Two Types of Parallel Hybrid Vehicles

In order to see the influence of hybridization on CO_2 emissions the torque split problem is solved using dynamic programming for hybridization ratios ranging from 5% to 75% with a step of 0.5%. The resulting CO_2 emissions for the eight different driving cycles are shown in Fig. 3.7. The resulting optimal hybridization ratios and comparisons are summarized in Table 3.1. Since the step in hybridization is 0.5% the numbers in Table 3.1 are only a rough estimate.

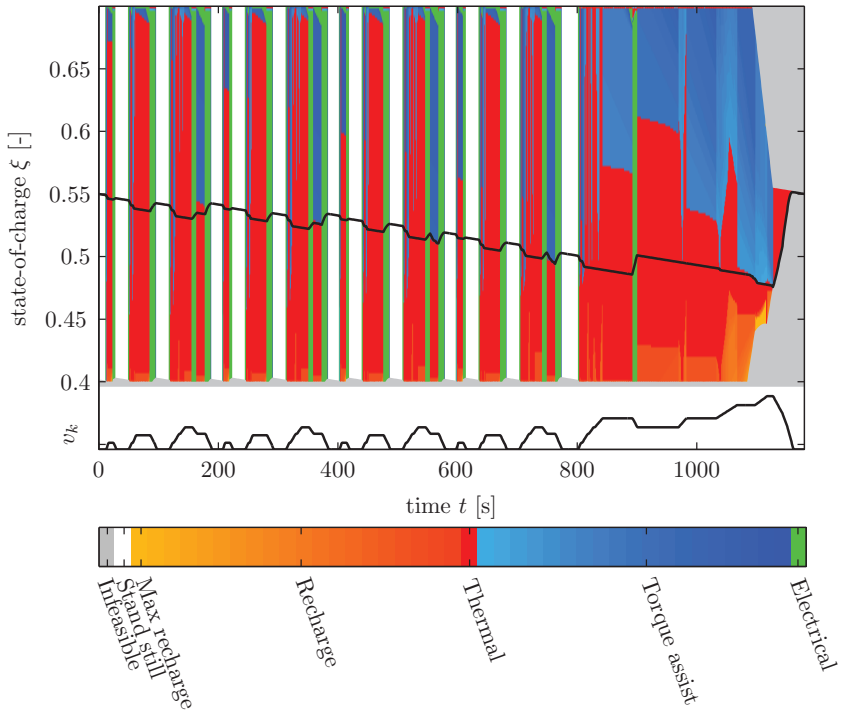

Figure 3.5: The optimal input map for the torque-assist hybrid with 21.5% hybridization ratio driving the NEDC and the optimal state of charge trajectory (black).

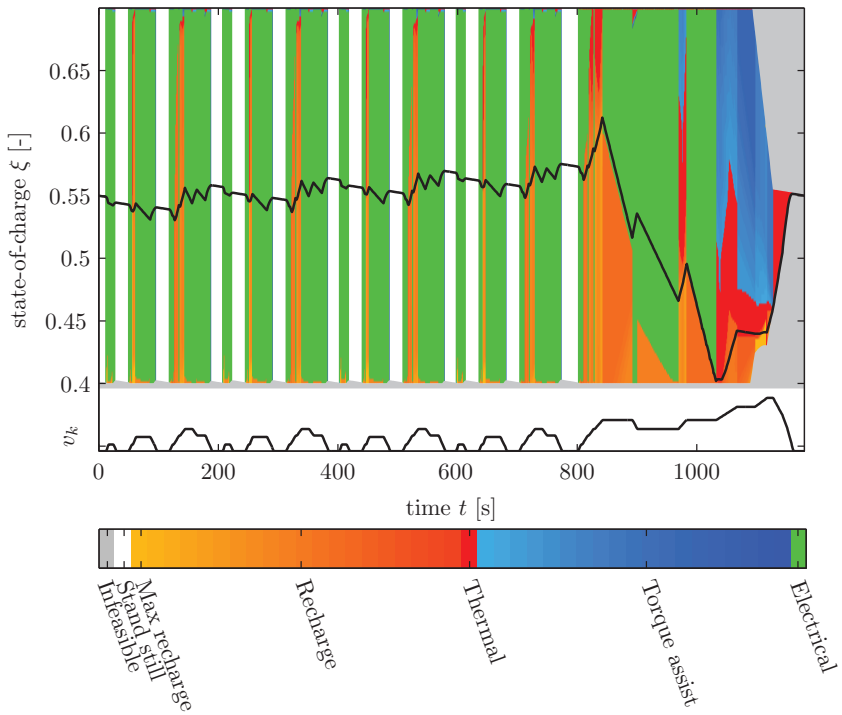

Figure 3.6: The optimal input map for the full hybrid with 21.5% hybridization ratio driving the NEDC and the optimal state of charge trajectory (black).

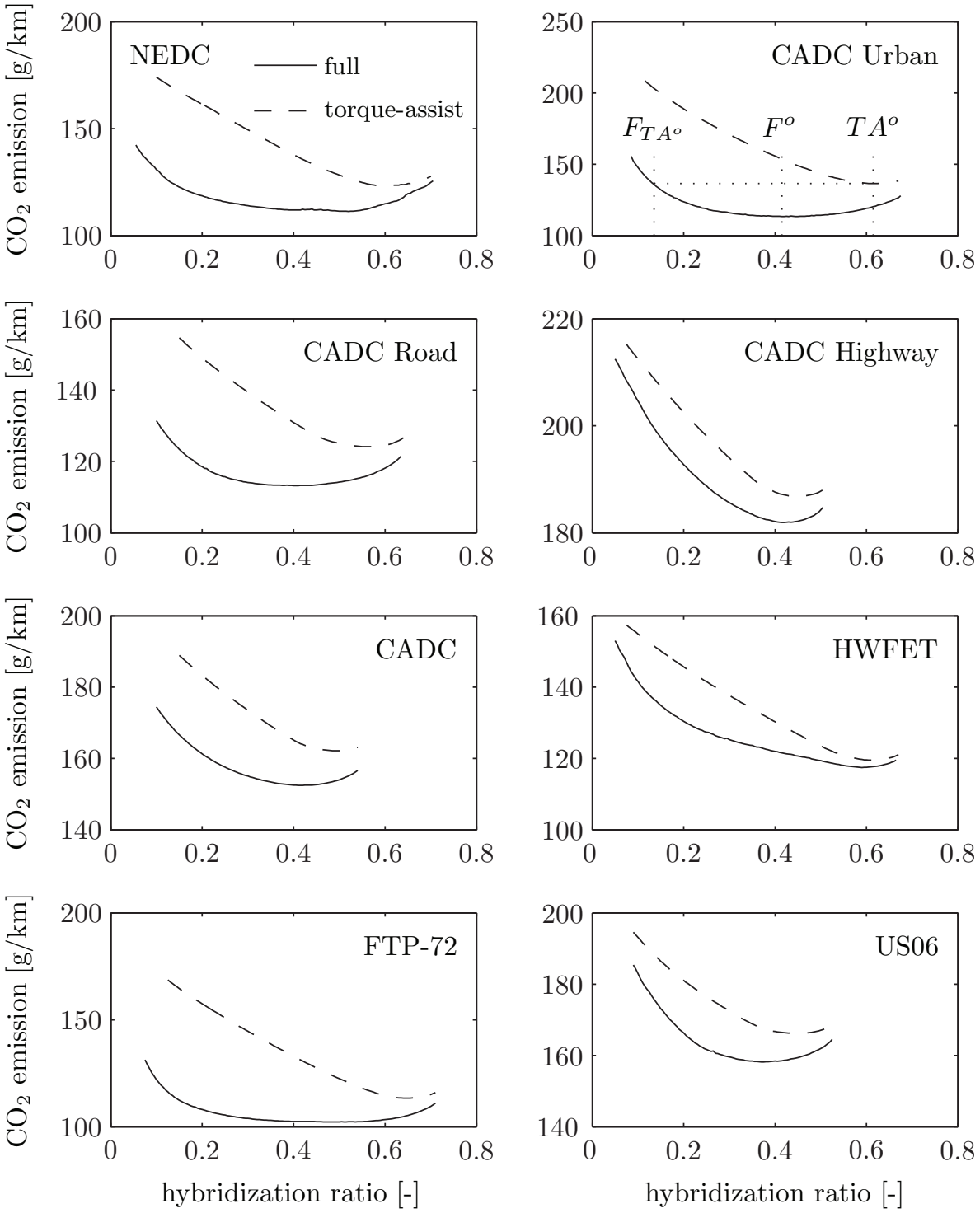

Figure 3.7: Carbon dioxide emissions for the torque-assist hybrid (dashed) and the full hybrid (solid).

Since the optimal control in the full hybrid utilizes electric driving considerably more than in the torque-assist hybrid the expectation is that the need for hybridization is higher in a full hybrid than in a torque-assist hybrid. The results in Fig. 3.7 and in Table 3.1 on the other hand show that the optimal hybridization ratio in a full parallel hybrid is in fact at lower levels of hybridization than in a torque-assist parallel hybrid. The reason for this is the reduced degree of freedom in the torque-assist hybrid. Electric driving is not beneficial since the engine cannot be decoupled and has to be dragged by the electric motor. The reduced degree of freedom makes the torque-assist hybrid a typical downsizing concept where most of the reduction in fuel consumption when increasing hybridization ratio is due to the downsized combustion engine. For the full parallel hybrid the benefit also comes from the possibility of occasionally increasing the load of the combustion engine in order to, later, be able to drive purely electrically. The freedom of such shifts in operating points is reduced when the hybridization ratio is increased too much. The clear difference in optimal strategy has therefore also clear implications on optimal hybridization ratio.

3.2 Sizing Rule for the Torque-Assist Parallel Hybrid

In this section we consider a torque-assist parallel hybrid electric vehicle. The torque-assist hybrid configuration is shown in Fig. 2.16. This section starts from the optimal control approach using the dynamic programming method and, through analysis of the optimal strategies and optimal hybridization ratios, develops a simple rule to size the considered hybrid vehicle for a given driving cycle. The proposed sizing law is compared to the results from dynamic programming for all the eight different driving cycles in Appendix B. Two gear-ratio-definition schemes are used to examine the influence of the gear ratio choice on the proposed sizing law, fixed and adjusted gear ratios. The adjusted gear ratios are defined using a simple rule described in Section 3.1.2 and the fixed gear ratios are defined for a 1.6 liter combustion engine. Finally, a study on how several parameters affect the results is shown in order to emphasize the robustness of the proposed sizing rule.

3.2.1 Dynamic Programming: Analysis

This section presents the results obtained when the dynamic programming algorithm, shown in Chapter 4, is used to optimize the energy management strategy for different hybridization ratios with the same maximum power-to-weight ratio. The dynamic programming algorithm has been used for hybridization ratios between 5% and 85% using a discretization of 0.5%. This section analyzes the dynamic programming results in order to establish a basis for developing a component sizing law. For a single vehicle configuration the output of the dynamic programming algorithm is an optimal torque split map over time and battery state-of-charge. For a visualization of such a map readers are referred to [4]. Once the optimal torque split map is calculated, the map and the model is used in a forward fashion to generate the optimal state-of-charge trajectory, fuel consumption, and CO_2 emission. The optimal CO_2 emissions using fixed gear ratios for different hybridization ratios for the driving cycles NEDC, CADC, and FTP-72 as detailed in Appendix B are shown in Fig. 3.8. To analyze

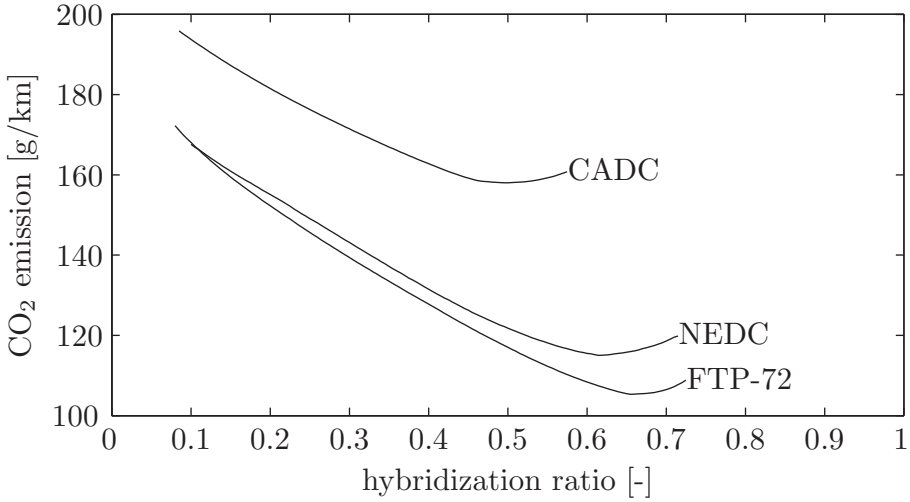

Figure 3.8: Optimal CO_2 emissions, determined by dynamic programming, for different hybridization ratios for NEDC, CADC, and FTP-72 using fixed gear ratios.

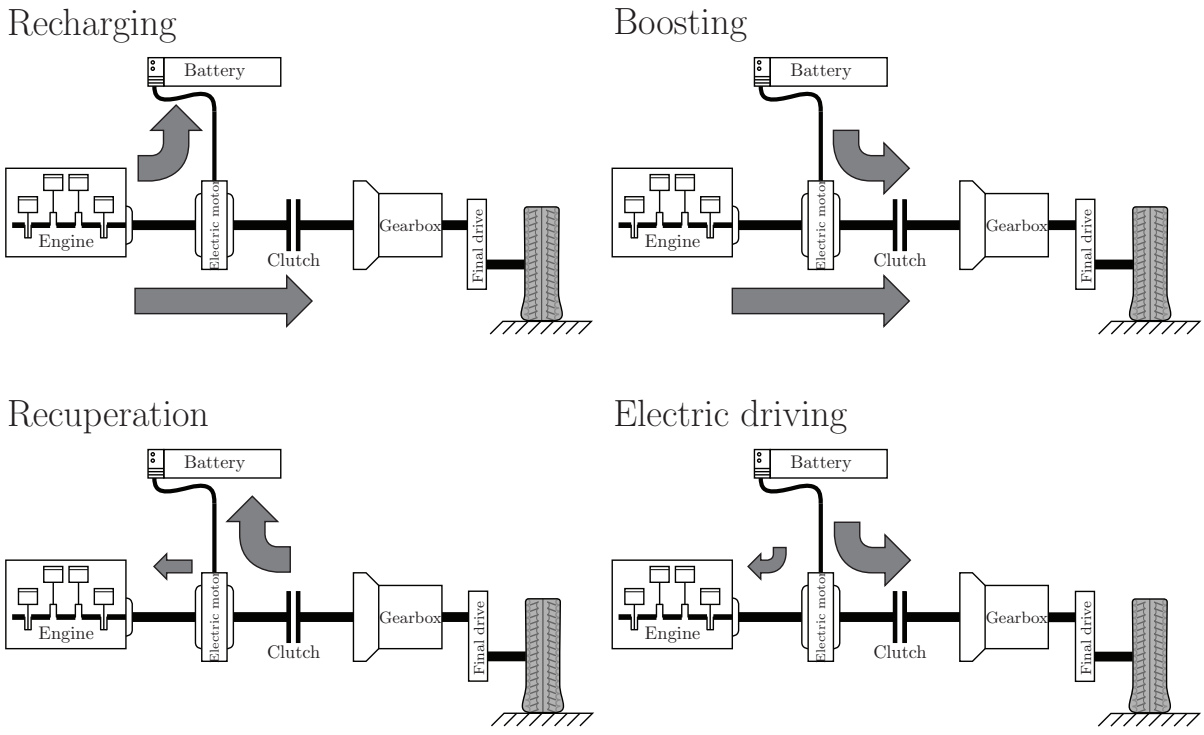

Figure 3.9: Energy flow for the electric operating modes 1) Recharging 2) Torque boosting 3) Recuperation 4) Electric driving. When operating in electric driving and recuperation modes, there is also an energy flow to the engine due to engine friction and the coupling between the motor and the engine.

the results shown in Fig. 3.8, the different electric operating modes must be considered. The operating modes are different levels of torque boosting, electric driving, brake energy recuperation, and battery recharging. The energy flows for the various electric operating modes are shown in Fig. 3.9. Torque boosting is when both the combustion engine and the electric motor provide torque for traction (top right graph in Fig. 3.9). Battery recharging corresponds to the mode when the combustion engine is providing more torque than demanded by the driving cycle in order to recharge the battery (top left graph in Fig. 3.9). Electric driving and brake energy recuperation are the modes when only the electric motor is used for negative torque (braking) and positive torque (traction), respectively (shown in the bottom two graphs in Fig. 3.9). Note that in the electric driving and recuperation modes some energy is always dissipated in the engine due to friction.

The different levels of each mode are determined by the torque split factor u. It is important to note that in this study the engine and electric motor are always coupled and that the results of this study would change significantly if a clutch was introduced between engine and motor.

The following analysis of the different modes focuses on the electric path energy and in particular on the energy available for traction at the crankshaft. For example, the recuperated braking energy has to go through the electric path into the battery and then back again in order to be referred to as energy available for traction.

The different energy flows in the electric path are shown in Fig. 3.10. Each energy in Fig. 3.10 is the power accumulated during the driving cycle. The battery average efficiency η_{batt}, motor efficiency η_{mot}, and generator efficiency η_{gen} are given by

$$\eta_{batt} = \frac{E_{el}^{out}}{E_{el}^{in}} \quad \eta_{mot} = \frac{E_{mech}^{out}}{E_{el}^{out}} \quad \eta_{gen} = \frac{E_{el}^{in}}{E_{mech}^{in}} \tag{3.4}$$

if the final state-of-charge is the same as the initial state-of-charge, which is the case when solving the dynamic programming problem described in Chapter 4. The total electric path efficiency, calculated over a driving cycle, is

$$\eta_{epath} = \eta_{gen} \cdot \eta_{batt} \cdot \eta_{mot}. \tag{3.5}$$

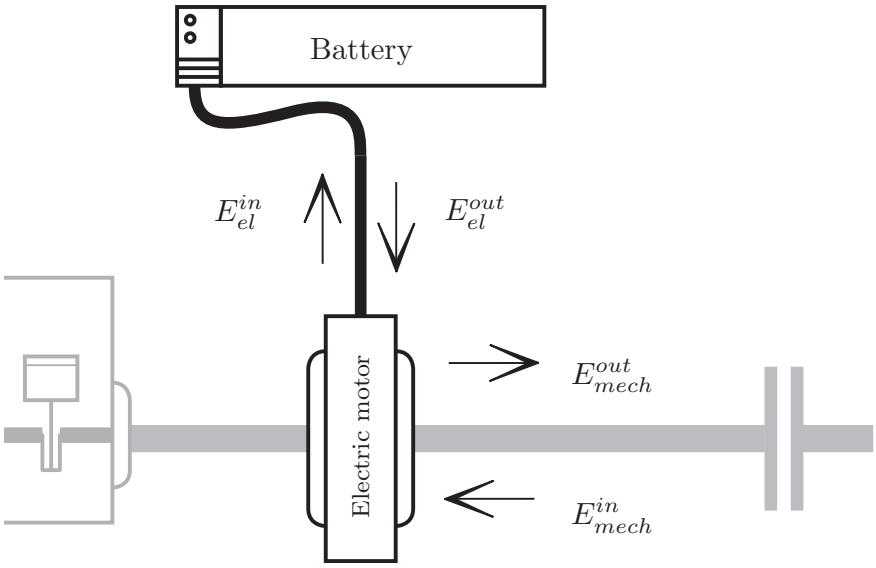

Figure 3.10: Electric path energy flows.

Let us start by analyzing the modes that charge the battery, namely recharging and brake energy recuperation. The amount of recuperated brake energy is

$$E_{rec} = -\sum_{\substack{0\leq k<N \\ T_{d,k}<0 \\ T_{m,k}<0}} T_{m,k} \cdot \omega_{c,k} \cdot t_s. \tag{3.6}$$

Note that the recuperated energy E_{rec} might not be equivalent to the amount of brake energy during a driving cycle, due to powertrain limitations during hard braking phases (such as current and torque limitations). The recuperated energy available for traction is then

$$E_{rec}^{tra} = \eta_{epath} \cdot E_{rec} \tag{3.7}$$

since the recuperated energy has to go through the electric path (generator-battery-motor) before being available for traction. The recharging energy is

$$E_{rech} = -\sum_{\substack{0\leq k<N \\ T_{d,k}>0 \\ T_{m,k}<0}} T_{m,k} \cdot \omega_{c,k} \cdot t_s. \tag{3.8}$$

Similarly to the recuperated energy, the recharged energy available for traction is

$$E_{rech}^{tra} = \eta_{epath} \cdot E_{rech} \tag{3.9}$$

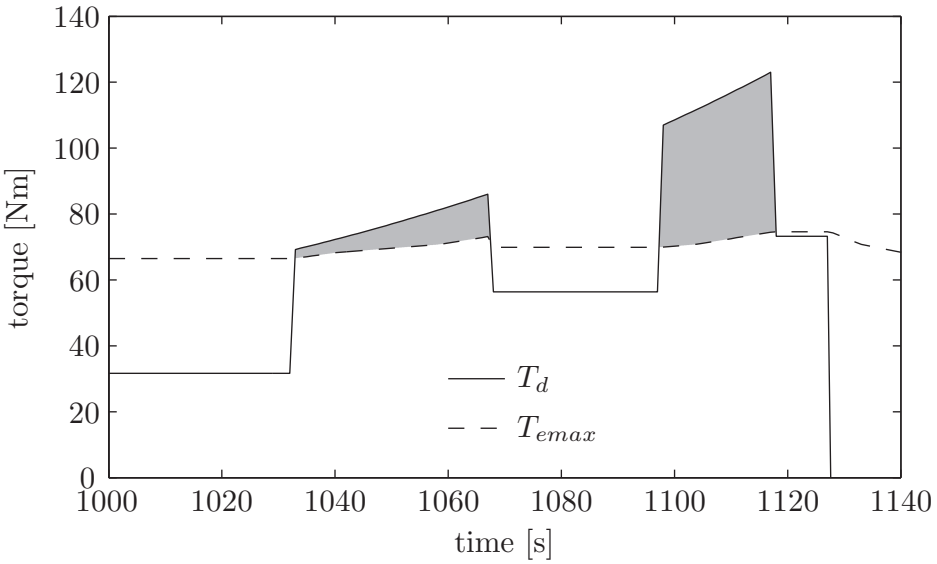

Figure 3.11: Torque profile for a part of the NEDC. Combustion engine maximum torque (dashed), driving cycle torque demand (solid), and the origin of the required boost torque (gray area).

since the recharged energy has to go through the electric path before being available for traction. To estimate the optimal hybridization ratio consider the following definition. Let the minimum required boost energy for a given driving cycle be

$$E_{bst} = \sum_{\substack{0 \le k < N \\ T_{d,k} > T_{emax,k} \\ \omega_{c,k} \ge \omega_{idle}}} \Big(T_{d,k} - T_{emax,k} \Big) \cdot \omega_{c,k} \cdot t_s. \tag{3.10}$$

Figure 3.11 shows the torque demand T_{dem} (solid line) at the end of the NEDC. In addition, the maximum engine torque, for a rather small engine, is shown (dashed line) together with the torque deficit (gray region) which, multiplied with the crankshaft speed, yields the minimum required boosting power.

The additional required energy from the electric path is the required start-assist energy

$$E_{start} = \sum_{\substack{0 \le k < N \\ T_{d,k} > 0 \\ \omega_{c,k} < \omega_{idle}}} T_{d,k} \cdot \omega_{c,k} \cdot t_s. \tag{3.11}$$

The operating points in terms of torque and speed from where the required boost energy E_{bst}, required start-assist energy E_{start}, and recuperation energy E_{rec} originate are shown in Fig. 3.12.

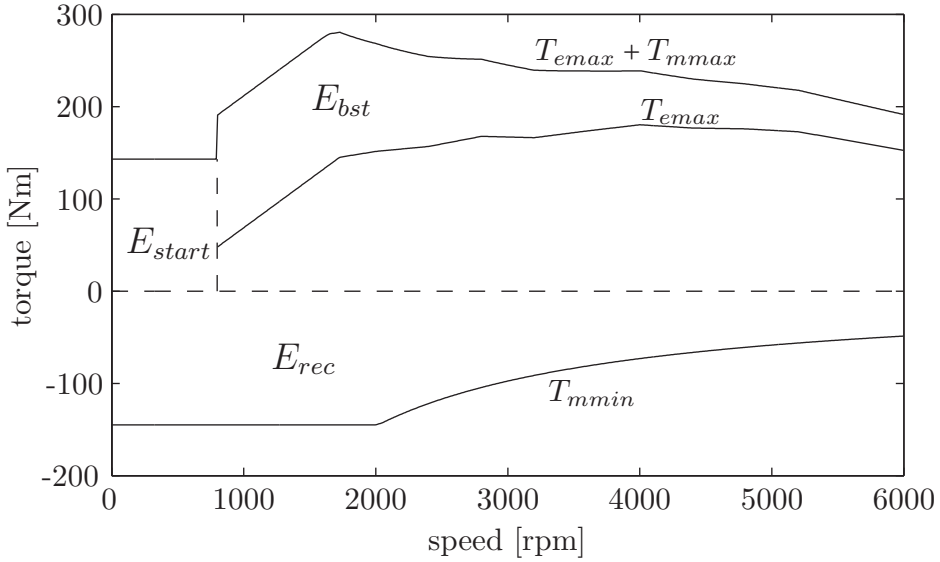

Figure 3.12: Speed-torque map over combustion engine and electric motor torque limits, together with the regions from which the required boost energy E_{bst}, required start-assist energy E_{start} and recuperation energy E_{rec} originate.

It is now possible to define the theoretical minimum required electric energy

$$E_{el,req} = E_{start} + E_{bst}, \tag{3.12}$$

which is the smallest amount of electric energy that is required to complete the driving cycle.

Consider the optimal CO_2 emission for NEDC, CADC, and FTP-72 shown in Fig. 3.8. The main reason for the reduction in CO_2 emission is the fact that the engine is downsized when the hybridization ratio is increased. This leads to a higher mean effective pressure and therefore a higher efficiency. However, the energies in the electric path also affect the CO_2 emission. The theoretical minimum required electric energy, the recuperated energy available for traction, and the recharging energy available for traction for the three driving cycles are shown in Fig. 3.13.

The recuperated energy available for traction E_{rec}^{tra} (solid curve in Fig. 3.13) increases with an increasing hybridization ratio due to three effects. First, the electric path size increases and thus the peak charging power increases, which allows for a more complete recuperation. Second, the total vehicle mass increases and with it the energy to be recuperated potentially. Third, the ICE drag torque decreases, which thus reduces the energy losses

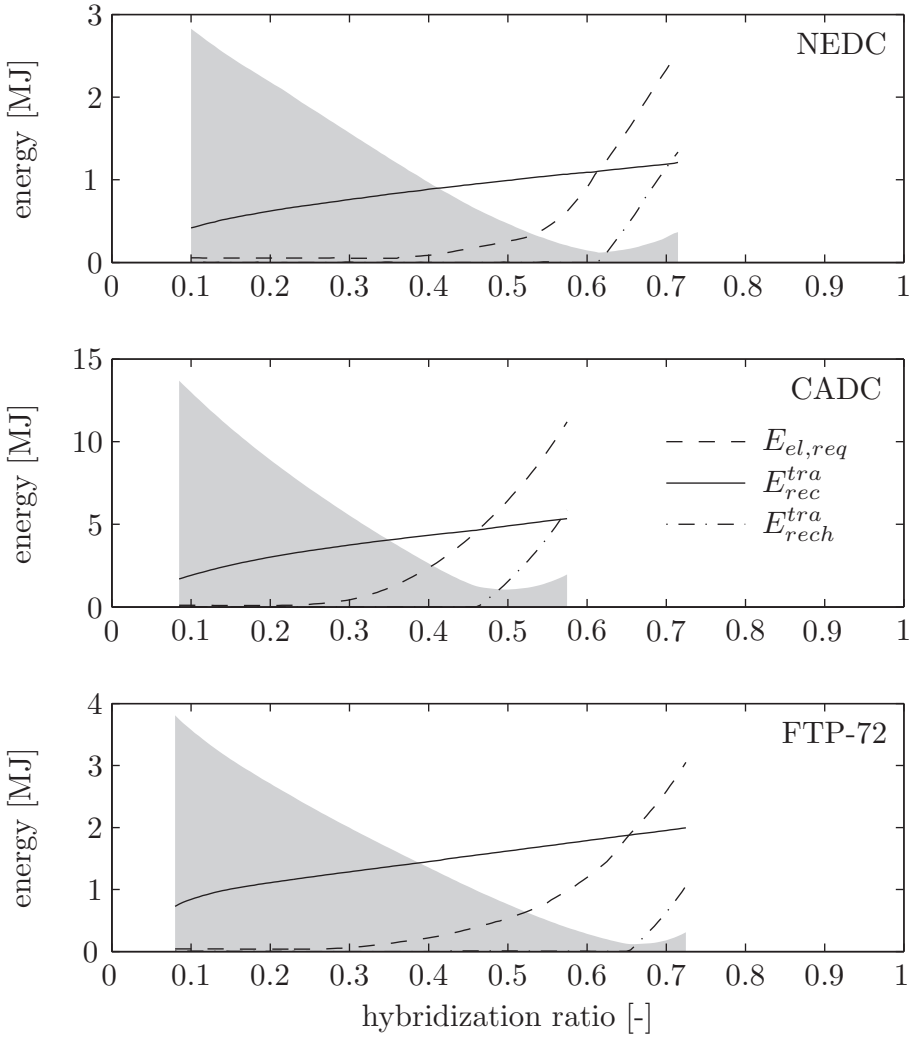

Figure 3.13: Energy analysis with recharging energy available for traction (dot-dashed), recuperated energy available for traction (solid), and theoretical minimum required electric energy (dashed) and the minimum CO_2 emission profile (gray) for the NEDC, CADC, FTP-72 with varying hybridization ratio.

while braking. The theoretical minimum required electric energy[1] $E_{el,req}$ (dashed line in Fig. 3.13) includes the two components, the start-assist energy and the minimum required boost energy. The start-assist energy increases slightly due to the increased mass of the vehicle. However, the largest contribution to the increase in the minimum required electric en-

[1]Note that the theoretical minimum required electric energy with its components start and boost energy requirement, is not the same as the actual electric energy used by the optimal strategy. For low hybridization ratios the recuperated energy available for traction is larger than the theoretical minimum required electric energy. The optimal strategy thus uses the remaining recuperated energy either for torque boosting or for electric driving.

ergy $E_{el,req}$ is due to the minimum required boost energy E_{bst}. The reason for this fact is the decreasing maximum torque of the ICE when the hybridization ratio is increased. The significant change in the slope of the minimum electric energy required $E_{el,req}$ for the NEDC at $HR \approx 0.55$ is due to the non-smooth torque distribution for this cycle. For the NEDC, there are long constant vehicle speed regions with constant torque demand. Consequently there is a threshold at which the maximum engine torque is lower than the torque required at the constant vehicle speed regions of the cycle. The slope of $E_{el,req}$ in Fig. 3.13 thus changes since the torque deficit has to be provided by the electric motor. A similar but much smaller effect can be observed in the FTP-72 cycle. The electric energy produced by the ICE available for traction E_{rech}^{tra} is shown by the dot-dashed curve in Fig. 3.13.

The following observations can be made from the energy analysis shown in Fig. 3.13. The recharging mode is used only when the recuperated energy available for traction is lower than the minimum required electric energy. When the recuperated energy cannot fulfill the minimum required electric energy demand, only the difference must be recharged using the ICE (see Fig. 3.13 at high hybridization ratios). The optimal strategy is therefore to minimize the amount of necessary recharging using the ICE as much as possible, since otherwise recharging would occur even for low hybridization ratios.

The outline of the optimal CO_2 emissions (shown first in Fig. 3.8) are shown in Fig. 3.13 as areas shaded gray. The minimum CO_2 emission and the optimal hybridization ratio are very close to the point where the recuperated energy available for traction E_{rec}^{tra} is equal to the theoretical minimum required electric energy $E_{el,req}$

$$HR^o \approx HR|_{E_{el,req}=E_{rec}^{tra}}, \tag{3.13}$$

in other words, where the recuperated energy only is used for the necessary boosting when the engine is operating at maximum load. This observation, which is a key result of this section, is also true for the remaining driving cycles shown in Appendix B. The next section uses this property to define a simple sizing algorithm for the considered hybrid electric vehicle.

3.2.2 Equilibrium Point: Definition

Based on the observations and the analysis in the previous section, it is now possible to define the equilibrium hybridization point and the corresponding equilibrium point strategy as follows:

Definition

The equilibrium point strategy (EPS) is the energy management strategy in a hybrid electric vehicle that uses all recuperated energy for vehicle starting and torque-assist when the combustion engine operates at maximum load.

Definition

The equilibrium hybridization point (EP) for a hybrid electric vehicle on a given driving cycle is the hybridization ratio (defined in Section 3.1.2) where the equilibrium point strategy is charge-sustaining.

Note that the EPS is not charge-sustaining for hybridization ratios other than EP. Using the definitions of EPS and EP, the equilibrium point is exactly that hybridization ratio at which the required electric energy $E_{el,req}$ is equal to the recuperated energy available for traction E_{rec}^{tra}

$$EP \equiv HR|_{E_{el,req}=E_{rec}^{tra}}. \tag{3.14}$$

One of the main results of this section is that the EP is close to the global optimum. It is important to note that the EPS is an extremely simple and rule-based energy management strategy, which can be written as

$$T_e = \begin{cases} T_d & \text{if } 0 < T_d \le T_{emax} \text{ and } \omega_c \ge \omega_{idle} \\ T_{emax} & \text{if } T_d > T_{emax} \text{ and } \omega_c \ge \omega_{idle} \\ 0 & \text{otherwise} \end{cases} \tag{3.15}$$

$$T_m = \max(T_d - T_e,\ T_{epathmin}). \tag{3.16}$$

Moreover, its simplicity allows the EP to be found using a simple iterative procedure of vehicle model scaling and simulation. One simple algorithm for finding the EP is the following:

1. Initialize a hybrid electric vehicle model with the hybridization ratio $HR = HR_0$ (using a constant power-to-weight ratio)

2. Simulate the given driving cycle using the equilibrium-point strategy

3. If $\xi_N > \xi_0$
   then increase HR and go to step 2

   If $\xi_N < \xi_0$
   then decrease HR and go to step 2

   If $\xi_N = \xi_0$
   then $EP = HR$

Note that if, due to vehicle limitations, the equilibrium point cannot be found within the feasible range of the hybridization ratios the final state-of-charge will differ from the initial state-of-charge for the feasible hybridization ratios. If this is the case, the resulting fuel consumption/CO_2 emission must be corrected for the stored/missing energy in the battery. This can be done by estimating the equivalence factor [5] using the average efficiencies of the electric path and the combustion engine.

3.2.3 Equilibrium Point: Results

As shown in Section 3.2.1 the EP is close to the optimal hybridization ratio. This section shows the EP and the optimal CO_2 emissions for all eight driving cycles described in Appendix B. The EP is compared to the global optimum obtained by DP for three different cases. First the EP is compared to the global optimum when the gear ratios are kept constant while the hybridization ratio is changed. Secondly, a comparison is made when the gear ratios are adjusted to the specific engine size, as mentioned

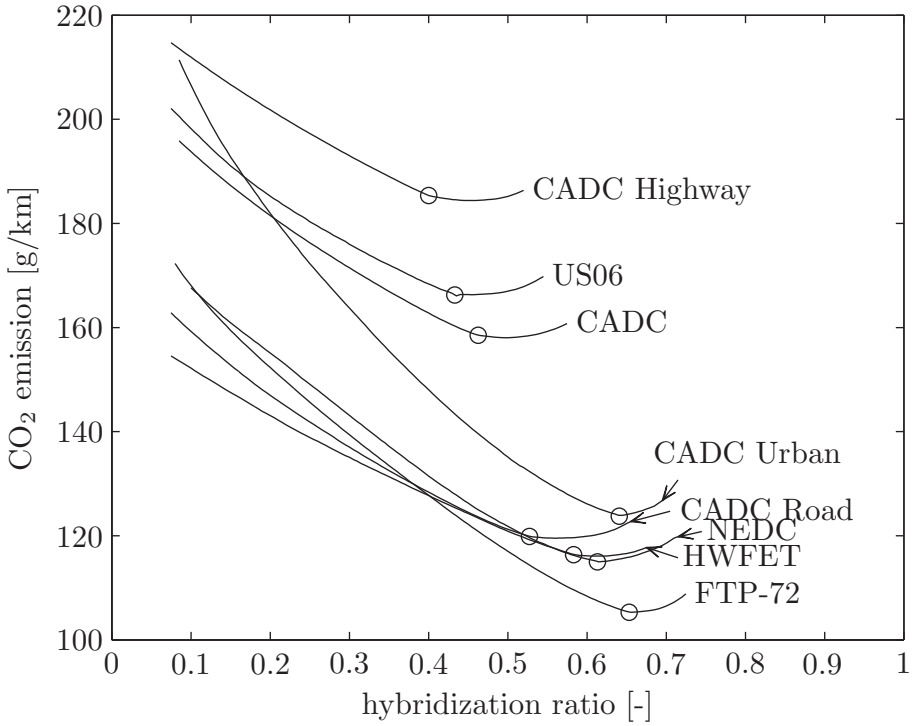

Figure 3.14: The optimal CO_2 emissions (using fixed gear ratio) determined by DP (solid black) for eight different driving cycles together with the EP solution (circle) for each of the driving cycles.

in Section 3.1.2. Third, the optimal hybridization ratios using the rule-based gear switching strategy for adjusted gear ratios are compared to the optimal hybridization ratios obtained when the gear switching is optimal[2].

Fixed Gear Ratio

This section shows the equilibrium point for the eight cycles using fixed gear ratios. The optimal CO_2 emissions for various hybridization ratios and the EP are shown in Fig. 3.14. There is a clear optimum for each of the eight driving cycles, and the EP solution is close to the optimal hybridization ratio. The absolute values for the equilibrium point, together with the optimal hybridization ratios, are shown in Table 3.2. Also, the relative hybridization ratio error e_{hr} between EP and the optimal HR is shown in Table 3.2. When considering fixed gear ratios, the equilibrium

[2]The optimal gear shifting is determined by extending the DP algorithm described in Chapter 4 to two input variables, namely torque split and gear number.

Table 3.2: Results: fixed gear ratios

Drive cycle	HR [%]			CO_2 [g/km]		
	HR^o	EP	$\epsilon_{hr}[\%]$	CO_2^o	CO_2^{ep}	$\epsilon_{co_2}[\%]$
NEDC	61.5	61.3	-0.3	115.0	115.0	0.0
CADC Urb.	64.0	64.1	0.1	123.9	123.7	-0.1
CADC Rd.	56.0	52.8	-6.2	119.5	119.8	0.3
CADC Hwy.	45.5	40.0	-13.7	184.4	185.3	0.5
CADC	49.5	46.3	-7.0	158.0	158.5	0.3
HWFET	61.5	58.3	-5.5	116.1	116.4	0.3
FTP-72	65.5	65.3	-0.3	105.3	105.3	0.0
US06	43.5	43.3	-0.4	166.1	166.3	0.1

point is a lower estimate for the optimal hybridization ratio. The relative error is less than 14% for all driving cycles, which shows that the EP can be used for the estimation of the optimal hybridization ratio.

Table 3.2 also shows the absolute value of the CO_2 emission for the optimal HR and the CO_2 emission for the EP, together with the relative error e_{co_2}. For all driving cycles the CO_2 emission of the EP is extremely close to the CO_2 emission of the optimal HR. Clearly, for all driving cycles, the relative error between the CO_2 emission of the EP and the optimal HR is less than 0.5%.

It is important to note that, in Table 3.2, the proposed method appears to be better than dynamic programming for the CADC Urban driving cycle. There are two reasons for this effect. First, the hybridization ratios investigated in the dynamic programming analysis might not be exactly the true optimum due to the discretization of 0.5%. In contrast, the proposed method finds a hybridization ratio in a continuous interval. Secondly, the discretization of the continuous state and input spaces, when using the dynamic programming algorithm, always causes certain numerical errors. An additional dynamic programming optimization for CADC Urban with a hybridization of 64.1%, 3001 elements in the state grid, and 201 elements in the input grid shows an optimal CO_2 emission of 123.7 g/km, which is equivalent to the EP solution shown in Table 3.2.

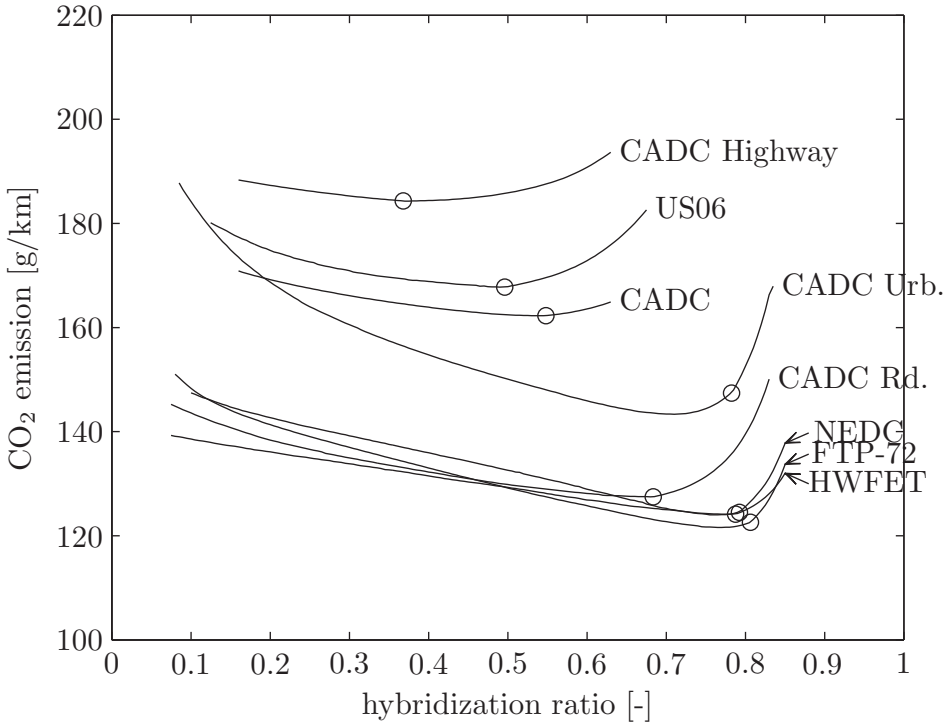

Figure 3.15: The optimal CO_2 emissions (using adjusted gear ratio) determined by DP (solid line) for eight different driving cycles together with the equilibrium point (circle) for each of the driving cycles.

Adjusted Gear Ratio

This section shows the results obtained when adjusting the gear ratios for different hybridization ratios. Figure 3.15 shows the equilibrium point and the optimal CO_2 emission using the same representation as in Fig. 3.14.

As mentioned earlier, the bore-to-stroke ratio is kept constant when the displacement is varied. For small engine displacements the speed range of the engine is therefore higher than for engines with larger displacements. When using fixed gear ratios in the gearbox, the rotational speed of the engine is equal for different engine sizes. Small engines therefore have relatively low rotational speeds compared to their operating range. Also, large engines have relatively high rotational speeds compared to their operating range when fixed gear ratios are used. As Fig. 3.15 shows, the CO_2 emission lines therefore turn out to be flatter when adjusted gear ratios are used than for the fixed gear ratios shown in Fig. 3.14.

For the driving cycles CADC, CADC Highway, and US06 the optimal

Table 3.3: Results: adjusted gear ratios

Driving cycle	HR [%]			CO_2 [g/km]		
	HR^o	EP	$\epsilon_{hr}[\%]$	CO_2^o	CO_2^{ep}	$\epsilon_{co_2}[\%]$
NEDC	76.5	79.3	3.5	124.0	124.5	0.4
CADC Urb.	71.0	78.3	9.3	143.3	147.4	2.7
CADC Rd.	68.0	68.4	0.5	127.5	127.5	0.0
CADC Hwy.	37.0	36.8	-0.5	184.3	184.3	0.0
CADC	54.5	54.8	0.6	162.3	162.3	0.0
HWFET	77.5	78.8	1.6	124.1	124.1	0.0
FTP-72	77.0	80.6	4.5	121.6	122.6	0.8
US06	49.0	49.6	1.3	167.8	167.7	0.0

HR does not change significantly when adjusted gear ratios are considered. However, for the remaining driving cycles the optimal hybridization is shifted towards higher levels.

Table 3.3 shows the EP solution, the optimal HR, and the relative HR error e_{hr}. Note the largest relative HR error of e_{hr} = 9.3% for the CADC Urban driving cycle. The reason for this is that, occasionally, electric driving is considered optimal even though the engine is dragged. This results in higher required electric energy and therefore in a shift of the calculated optimum towards lower levels. However, this effect is only present for extremely low demanding driving cycles. The CO_2 emission prediction for the CADC Urban, however, is only 2.7% from the global optimum.

The low relative error in hybridization ratio of less than 5%, for most cycles indicates that the EP is in fact closer to the optimal HR than when fixed gear ratios are considered. Moreover, as the right part of Table 3.3 shows, when the CO_2 emissions are considered, the EP predicts the optimal CO_2 emission with practically no relative error for most driving cycles.

In summary, especially for predicting the optimal CO_2 emission for a given driving cycle, the method of using the EP and EPS is a viable approach for estimating the global optimal solution. The small relative error in the optimal CO_2 emission prediction for CADC Urban indicates that the optimum is relatively flat and that the larger relative error in the

Table 3.4: HR^o [%] optimal gear shifting (adjusted gear ratios)

shifting	*NEDC*	*CADC Urb.*	*CADC Rd.*	*CADC Hwy.*	*CADC*	*HWFET*	*FTP-72*	*US06*
rule-based	76.5	71.0	68.0	37.0	54.5	77.5	77.0	49.0
optimal	75.5	91.0	61.5	39.5	50.5	73.0	85.5	47.5

prediction of the optimal hybridization ratio is not significant.

Optimal Gear Shifting

Thus far, the gear was chosen using a simple speed-dependent rule-based strategy. It is therefore interesting to investigate whether optimal gear shifting would significantly change the optimal hybridization ratio. In this section, the gear is included as an additional input variable for the DP algorithm to decide. When the gear is included in the algorithm, the computational burden is multiplied by the number of possible gear selections.

The optimal hybridization ratio for rule-based gear shifting, together with the optimal hybridization ratio when optimal gear shifting[3] is used, are shown in Table 3.4. On average for all eight driving cycles the CO_2 emission is 17% lower when using optimal gear shifting. The difference of the optimal HR using rule-based gear shifting and using optimal gear shifting is relatively small for most driving cycles. In other words, the equilibrium point is close to the optimal hybridization ratio even when the gear shifting is optimal. Note that for CADC Urban the optimal hybridization ratio changes significantly due to the increased amount of electric driving. For this extremely low demanding driving cycle the engine is only used to deliver a small amount of energy such that the final battery state-of-charge is equivalent to the initial state-of-charge. The majority of

[3]Note that the CO_2 emissions are different when optimal gear shifting is used since it offers a large potential of saving fuel.

the driving cycle is therefore driven purely electrically.

3.2.4 Parameter Sensitivity Analysis

The results in Section 3.2.3 are specific for the considered vehicle, i.e., a power-to-weight ratio of 68 W/kg, a nominal vehicle mass of $m_0 \approx 1500$ kg, and using no auxiliary electric power demand. This section explores the sensitivity of the results with respect to these parameters. First a variation on the power-to-weight ratio is explored, secondly a study of the sensitivity of m_0 on the results is performed. Finally, the effects of the auxiliary electric power demand on the optimal hybridization are investigated. All results in this section are produced by using the adjusted gear ratios.

Power-To-Weight Variation

Thus far, a constant power-to-weight ratio of 68 W/kg has been used. It is important to also verify the proposed method using different power-to-weight ratios. Table 3.5 shows the results of the proposed method, and using dynamic programming, for a power-to-weight ratio of 81 W/kg. Table 3.6 shows, in a similar way, the results of the proposed method for a power-to-weight ratio of 57 W/kg.

Note that when using a relatively low ratio of 57 W/kg the largest relative error in hybridization ratio is found for the CADC Highway driving cycle. The reason for the EP not corresponding to the optimum HR for this cycle is that the battery state-of-charge reaches its boundaries during this driving cycle. The method of finding the equilibrium point described in this section does not include the state-of-charge boundaries and is thus unable to make the necessary corrections. The dynamic programming solution on the other hand predicts and accounts for the state-of-charge limits.

The effect of the increased electric driving for extremely low demanding driving cycles such as CADC Urban, mentioned in Section 3.2.3, is similar also for different power-to-weight ratios. This can be seen by the high relative error for CADC Urban in Tables 3.5 and 3.6.

Table 3.5: Power-to-weight ratio 81 W/kg (adjusted gear ratios)

Driving cycle	HR [%]			CO_2 [g/km]		
	HR^o	EP	$\epsilon_{hr}[\%]$	CO_2^o	CO_2^{ep}	$\epsilon_{co_2}[\%]$
NEDC	80.0	82.6	3.2	131.3	131.9	0.4
CADC Urb.	74.0	81.4	9.1	155.4	160.0	2.9
CADC Rd.	71.5	73.5	2.7	134.6	134.6	0.0
CADC Hwy.	49.5	49.3	-0.4	189.5	189.5	0.0
CADC	60.5	63.0	4.0	168.9	168.9	0.0
HWFET	81.5	82.3	0.9	129.9	129.8	0.0
FTP-72	80.0	83.5	4.2	130.4	131.4	0.8
US06	56.0	57.9	3.2	175.0	175.1	0.0

Table 3.6: Power-to-weight ratio 57 W/kg (adjusted gear ratios)

Driving cycle	HR [%]			CO_2 [g/km]		
	HR^o	EP	$\epsilon_{hr}[\%]$	CO_2^o	CO_2^{ep}	$\epsilon_{co_2}[\%]$
NEDC	72.5	75.1	3.5	118.3	118.9	0.4
CADC Urb.	66.5	74.5	10.7	134.0	137.4	2.5
CADC Rd.	62.0	62.1	0.1	122.0	122.0	0.0
CADC Hwy.	29.5	26.3	-12.4	181.8	181.8	0.0
CADC	43.5	43.6	0.1	157.9	157.9	0.0
HWFET	72.0	74.4	3.3	119.8	119.9	0.1
FTP-72	73.0	77.1	5.3	114.7	115.6	0.8
US06	38.5	38.3	-0.5	163.2	163.1	0.0

Table 3.7: 150 kg lighter vehicle (adjusted gear ratios)

Drive cycle	HR [%]			CO_2 [g/km]		
	HR^o	EP	$\epsilon_{hr}[\%]$	CO_2^o	CO_2^{ep}	$\epsilon_{co_2}[\%]$
NEDC	75.0	78.6	4.6	116.3	116.9	0.5
CADC Urb.	69.0	77.8	11.3	132.2	136.5	3.2
CADC Rd.	67.5	67.8	0.5	119.5	119.5	0.0
CADC Hwy.	35.0	33.9	-3.1	176.5	176.6	0.0
CADC	52.5	52.9	0.7	154.1	154.1	0.0
HWFET	75.0	78.3	4.2	117.7	117.8	0.1
FTP-72	76.0	80.1	5.1	113.2	114.3	1.0
US06	48.0	48.6	1.3	158.9	158.8	0.0

However, for most driving cycles the equilibrium point corresponds well to the global optimal hybridization ratio and the CO_2 emission of the EP is extremely close to the global optimum calculated using DP.

Vehicle Mass Variation

In contrast to the previous section where the power-to-weight ratio is varied for a constant nominal vehicle mass $m_0 \approx 1500$ kg this section deals with a varying nominal vehicle mass for a constant power-to-weight ratio, namely 68 W/kg. Table 3.7 shows the results of the EP and the optimum determined by DP when a nominal vehicle mass of $m_0 \approx 1350$ kg is used. Similarly, Table 3.8 shows the resulting EP and the optimum determined by DP when a nominal vehicle mass of $m_0 \approx 1650$ kg is used. There is a slight indication that the method performs better in a heavier vehicle since the relative errors are slightly higher in Table 3.7. In general, however, the proposed method of using the EP as an estimate for the optimal hybridization ratio is not sensitive to changes in the nominal vehicle mass.

Influence of Auxiliary Power Demand

The influence of the auxiliary electric power demand on the optimal hybridization ratio was investigated by varying the auxiliary power demand

Table 3.8: 150 kg heavier vehicle (adjusted gear ratios)

Drive cycle	HR [%]			CO_2 [g/km]		
	HR^o	EP	$\epsilon_{hr}[\%]$	CO_2^o	CO_2^{ep}	$\epsilon_{co_2}[\%]$
NEDC	78.0	79.8	2.2	131.7	132.1	0.3
CADC Urb.	71.0	78.6	9.7	154.4	158.1	2.3
CADC Rd.	68.5	68.9	0.5	135.4	135.4	0.0
CADC Hwy.	39.0	38.8	-0.6	192.2	192.2	0.0
CADC	55.5	56.2	1.2	170.4	170.4	0.0
HWFET	79.0	79.1	0.2	130.6	130.5	0.0
FTP-72	77.5	81.0	4.3	129.9	130.7	0.6
US06	50.0	50.3	0.6	176.7	176.7	0.0

$P_{aux} \in \{0,\ 500,\ 1000,\ 1500,\ 2000\}$ W and determining the optimal hybridization ratio for each level of power demand. The dependency of the optimal hybridization ratio HR^o on the auxiliary power P_{aux} was thereafter fitted linearly, for each driving cycle, using a least squares method. The resulting sensitivity of the optimal hybridization ratio to the auxiliary power $\frac{\partial HR^o}{\partial P_{aux}}$ is shown in Table 3.9 for fixed and adjusted gear ratios. The average sensitivity of the optimal hybridization ratio with respect to the auxiliary power demand P_{aux} of all driving cycles is -1.2 %/kW when fixed gear ratios are used. Moreover, the average sensitivity is -3.9 %/kW when adjusted gear ratios are used. These results show that the optimal hybridization ratio decreases only slightly when the auxiliary power demand is increased. This low dependency on the auxiliary electric power demand is a confirmation of the fact that the hybridization ratio found using the method described in this section also is close to the optimum for varying levels of auxiliary power demand.

3.3 Summary and Discussion

We can conclude that for all eight driving cycles the optimal hybridization is lower in a full parallel hybrid than in a torque-assist parallel hybrid. The difference in hybridization ratio between the optimal torque-assist hybrid and the full hybrid that has the same fuel consumption and CO_2 emission

Table 3.9: HR^o sensitivity on auxiliary power $\frac{\partial HR^o}{\partial P_{aux}}$ [%/kW]

gear ratios	*NEDC*	*CADC Urb.*	*CADC Rd.*	*CADC Hwy.*	*CADC*	*HWFET*	*FTP-72*	*US06*
fixed	-1.1	-3.4	-1.0	-0.5	-0.6	-0.7	-1.7	-0.2
adjusted	-2.5	-5.4	-4.8	-0.5	-3.6	-4.1	-4.3	-5.9

can be as high as 51% (see FTP-72 in Table 3.1 and Fig. 3.7). What is more, the difference in CO_2 emissions between the torque-assist hybrid and the full hybrid increases with decreasing hybridization ratio. For a 20% hybrid driving the NEDC there is a 27% reduction of the fuel consumption when including an extra, electronically controlled, clutch. Since the model does not consider any energy losses during clutching and during starting of the combustion engine, the results of the full parallel hybrid is optimistic. This study assumes a predefined gear switching strategy and fixed gear ratios therefore future work will investigate the gear switching strategy's and ratios' influence on the results. Future work also include an analysis of the phenomenons that explain why the hybridization requirements in a full hybrid is smaller than in a torque-assist hybrid.

The proposed method of sizing a torque-assist parallel hybrid electric vehicle by finding the equilibrium point yields the optimal fuel consumption/CO_2 emission within 2.7% of the global optimum for eight different, commonly used, drive cycles. For most of the cycles the proposed method performs even better, less than 1%.

The reason that the method does not perform equally well on the CADC Highway cycle is that the state-of-charge boundary of the battery is reached and that the dynamic programming algorithm overcomes this problem whereas the proposed algorithm for finding the equilibrium point cannot do this without modifications.

The estimation is robust to the definition of the gear ratios since it is valid both when considering fixed gear ratios for different engine sizes and when considering adjusted gear ratios for different engine sizes. Further-

more, when using a given gear-switching strategy the equilibrium point is close to the optimal hybridization ratio using optimal gear switching. These results show that proposed method is robust with respect to the gear-shifting strategy. The parameter sensitivity analysis shows that the proposed method is robust to changes in power-to-weight ratio and nominal vehicle mass. The study on auxiliary power variations shows a very small influence on the optimal hybridization.

Future work includes deeper analysis and investigations on the exact reason why the auxiliary electric power demand has a small effect on the optimal hybridization ratio. Future work also includes similar investigations of other hybrid powertrain structures. In particular the question must be answered if the proposed approach of finding a sizing rule can be applied in other cases as well.

Chapter 4

Dynamic Programming

In this chapter a special class of optimal control problems is studied, namely problems with fixed final time and a partially constrained final state. Furthermore, the considered problems are assumed to include state constraints and input constraints. What is more, the dynamic systems in this study include only a single state variable, and the disturbances are assumed to be perfectly known. In summary, this problem can be written as an optimal control problem

$$\min_{u(t)} J(u(t)) \tag{4.1}$$

s.t.

$$\dot{x}(t) = F(x(t), u(t), t) \tag{4.2}$$

$$x(0) = x_0 \tag{4.3}$$

$$x(t_f) \in [x_{f,min},\ x_{f,max}] \tag{4.4}$$

$$x(t) \in \mathcal{X}(t) \tag{4.5}$$

$$u(t) \in \mathcal{U}(t), \tag{4.6}$$

where

$$J(u(t)) = G(x(t_f)) + \int_0^{t_f} H(x(t), u(t), t)dt \tag{4.7}$$

is the cost functional. This section gives a brief overview of the deterministic dynamic programming algorithm [22], which throughout this study is referred to as dynamic programming (DP). Since dynamic programming is a numerical algorithm used here to solve a continuous control problem, the continuous-time model (4.2) must be discretized. Let the discrete-time

model be given by

$$x_{k+1} = F_k(x_k, u_k), \qquad k = 0, 1, \ldots, N-1 \tag{4.8}$$

with the state variable $x_k \in \mathcal{X}_k$ and the control signal $u_k \in \mathcal{U}_k$. Furthermore, assume that the disturbance is perfectly known in advance and at every time instance k.

4.1 Basic Algorithm

Let $\pi = \{\mu_0, \mu_1, \ldots \mu_{N-1}\}$ be a control policy. Further let the discretized cost of (4.7) using π with the initial state $x(0) = x_0$ be

$$\begin{aligned} J_\pi(x_0) =& g_N(x_N) + \phi_N(x_N) \ldots \\ &+ \sum_{k=0}^{N-1} h_k(x_k, \mu_k(x_k)) + \phi_k(x_k), \end{aligned} \tag{4.9}$$

where $g_N(x_N) + \phi_N(x_N)$ is the final cost. The first term $g_N(x_N)$ corresponds to the final cost in (4.7). The second term is the additional penalty function $\phi_N(x_N)$ forcing a partially constrained final state (4.4). The function $h_k(x_k, \mu_k(x_k))$ is the cost of applying $\mu_k(x_k)$ at x_k, according to $H(x(t), u(t), t)$ in (4.7). The state constraints (4.5) are enforced by the penalty function $\phi_k(x_k)$ for $k = 0, 1, \ldots, N-1$.

The optimal control policy π^o is the policy that minimizes J_π

$$J^o(x_0) = \min_{\pi \in \Pi} J_\pi(x_0), \tag{4.10}$$

where Π is the set of all admissible policies.

Based on the principle of optimality [22], dynamic programming is the algorithm which evaluates the optimal cost-to-go[1] function $\mathcal{J}_k(x^i)$ at every node in the discretized state-time space[2] by proceeding backward in time:

[1]The terms *cost-to-go* and *optimal cost-to-go* are used equivalently throughout this chapter referring to *optimal cost-to-go*. It is important to note that the term optimal is used in the sense of optimality achievable despite the numeric errors.

[2]The following notation is used: x_k^i denotes the state variable x in the discretized state-time space at the node with time-index k and state-index i, while x_k denotes a (state-)continuous state variable at time k.

1. End cost calculation step

$$\mathcal{J}_N(x^i) = g_N(x^i) + \phi_N(x^i) \tag{4.11}$$

2. Intermediate calculation step for $k = N - 1$ to 0

$$\mathcal{J}_k(x^i) = \min_{u_k \in \mathcal{U}_k} \left\{ h_k(x^i, u_k) + \phi_k(x^i) \ldots + \mathcal{J}_{k+1}(F_k(x^i, u_k)) \right\} \tag{4.12}$$

The optimal control is given by the argument that minimizes the right-hand side of equation (4.12) for each x^i at time index k of the discretized state-time space.

The cost-to-go function $\mathcal{J}_{k+1}(x)$ used in (4.12) is evaluated only on discretized points in the state space. Furthermore, the output of the model function $F_k(x^i, u_k)$ is a continuous variable in the state space which can be between the nodes of the state grid. Consequently, the last term in (4.12), namely $\mathcal{J}_{k+1}(F_k(x^i, u_k))$ must be evaluated appropriately. There exist several methods of finding the appropriate cost-to-go function $\mathcal{J}_{k+1}(F_k(x^i, u_k))$ such as using a nearest-neighbor approximation or using an interpolation scheme. Throughout this study, linear interpolation of the cost-to-go function $\mathcal{J}_{k+1}$ is used to account for the problem of the discretized state space.

The output of the algorithm (4.11)–(4.12) is an optimal control signal map. This map is used to find the optimal control signal during a forward simulation of the model (4.8), starting from a given initial state x_0, to generate the optimal state trajectory. In the map the control signal is only given for the discrete points in the state-space grid. The control signal is therefore interpolated when the actual state does not coincide with the points in the state grid.

4.2 Numerical Issues on the Boundary Line

When implementing the algorithm numerical errors must be considered and minimized. One issue to consider is the definition of the cost function for infeasible states and inputs. Infeasible states and inputs are of course

infinitely expensive and should therefore have infinite cost $\phi_k(x^i \notin \mathcal{X}_k) \to \infty$ for $k = 1, \ldots, N$ since the defined objectives (such as final state constraints and model limitations) cannot be achieved. When using infinite cost for such states, some substantial numerical errors occur due to the discretization of time and state space.

Define the set of reachable states Ω_k^i over one time-step by using all admissible inputs and starting at a given state x^i at time k

$$\Omega_k^i = \{x | x = F_k(x^i, u) \ \forall \ u \in \mathcal{U}_k\}. \tag{4.13}$$

Consider the grid point/time step domain in Fig. 4.1 (bottom) and the fact that the DP algorithm is calculating the cost-to-go for the state x^i at time $k+1$. If an infinite cost was used for infeasible states together with a linear interpolation, the feasible part of Ω_{k+1}^i would use an interpolation between an infinite cost-to-go $\mathcal{J}_{k+2}(x^i)$ and a finite cost-to-go $\mathcal{J}_{k+2}(x^{i+1})$. As a result, the cost-to-go for x^i at time $k+1$ becomes infinite, i.e., $\mathcal{J}_{k+1}(x^i) \to \infty$, although the grid point $\{k+1, \ i\}$ lies perfectly within the feasible domain.

Now consider the algorithm at time k and the step of calculating the cost-to-go for the state x^i. For the same reason as for the time $k+1$, the cost-to-go $\mathcal{J}_k(x^i)$ will be infinite since $J_{k+1}(x^i)$ was calculated before to be infinite. When these effects continue and the algorithm proceeds backwards in time, the calculated infeasible region will grow into the actual feasible region.

A first step to tackle this problem is to use a big, but finite value for the cost instead of infinity $\phi_k(x^i \notin \mathcal{X}_k) = \mathcal{J}_\infty$ for $k = 1, \ldots, N$. This big, finite value $\mathcal{J}_\infty$ must be bigger than the maximum value of the cost-to-go function $\mathcal{J}_k(x^i)$. Using a finite cost value for infeasible domains improves the solution, but the effect shown above for infinity cannot be completely eliminated close to the boundary line. Throughout this chapter, the method of using a finite cost value $\mathcal{J}_\infty$ for infeasible domains together with the algorithm in Section 4.1 is referred to as *basic DP*.

Due to the interpolation between feasible and infeasible states, the infinite gradient at the boundary line is being blurred. This is shown in Fig. 4.2 for the fishing problem (introduced later), where the dashed line

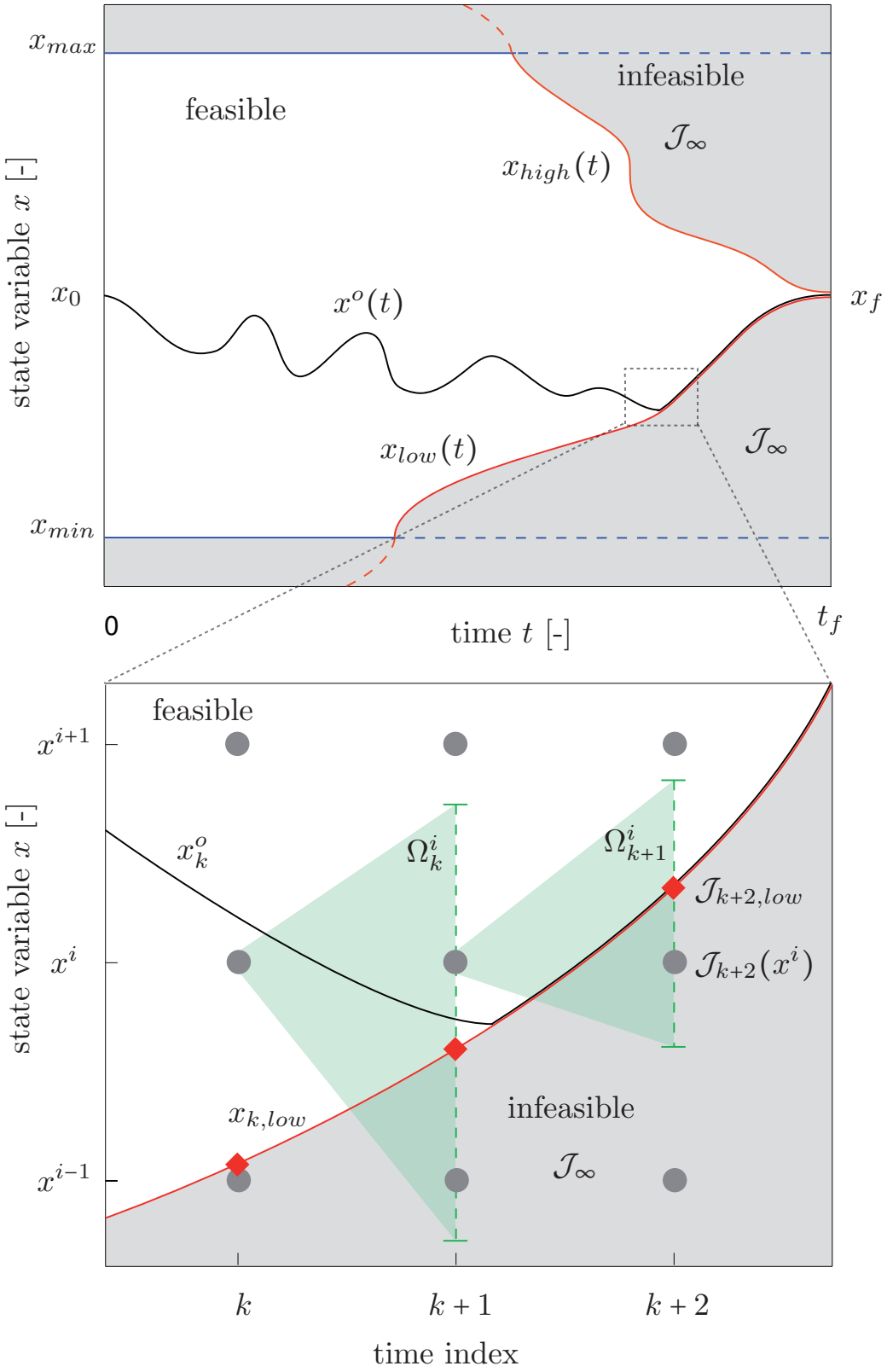

Figure 4.1: Schematic overview of an optimal control problem solved using the dynamic programming algorithm. The figure shows the state variable boundaries for the dynamic programming algorithm for the entire problem domain (top) and in the grid point/time step domain (bottom).

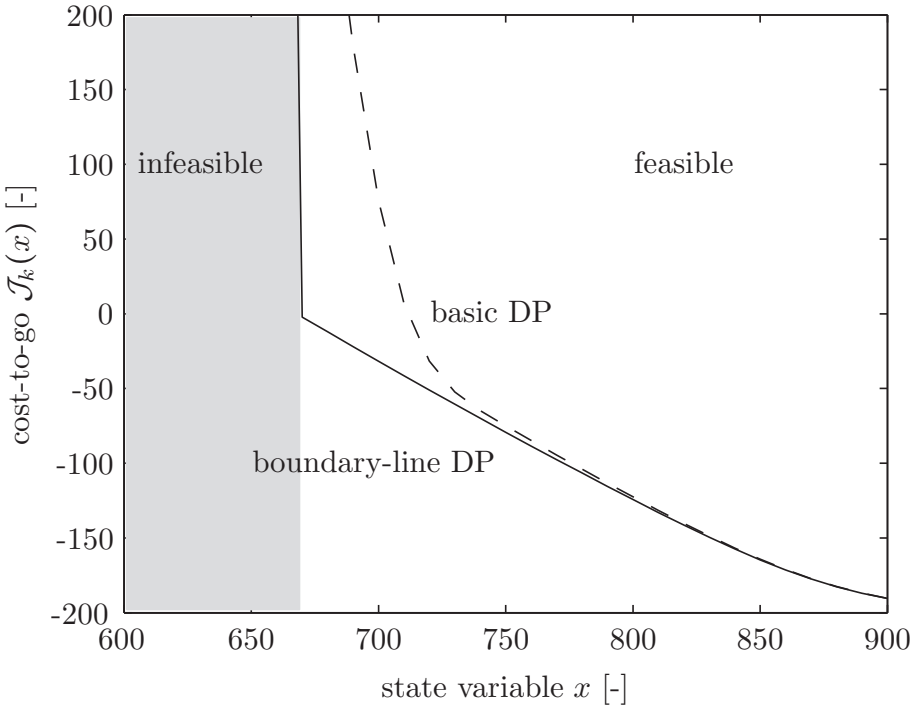

Figure 4.2: Section of the cost-to-go function $\mathcal{J}_k(x)$ at time index k such that $t = 180$ h for the fishing problem. State-space discretization is $\Delta x = 10$, penalty for infeasible states is set to $\mathcal{J}_\infty = 1200$.

is the cost-to-go computed by DP with a finite cost for infeasible states, i.e., the basic DP method. The solid line corresponds to the cost-to-go from DP improved by the new method introduced in this chapter. As a result of the blurred cost-to-go function, the optimal state trajectory cannot approach the boundary line since the computed cost-to-go near the boundary line is too high. Figure 4.3 shows the corresponding state trajectory (dashed) being deviated by this effect. The solid line is the state trajectory from DP improved by the new method.

4.3 Boundary-line method

The method presented in this chapter tackles the problem of a blurred gradient at the boundary line due to interpolation of the cost-to-go between a feasible and an infeasible state-grid point. Therefore, the boundary line between feasible and infeasible regions must be found. This is shown in the first part of this section. The second part shows a simple, yet powerful

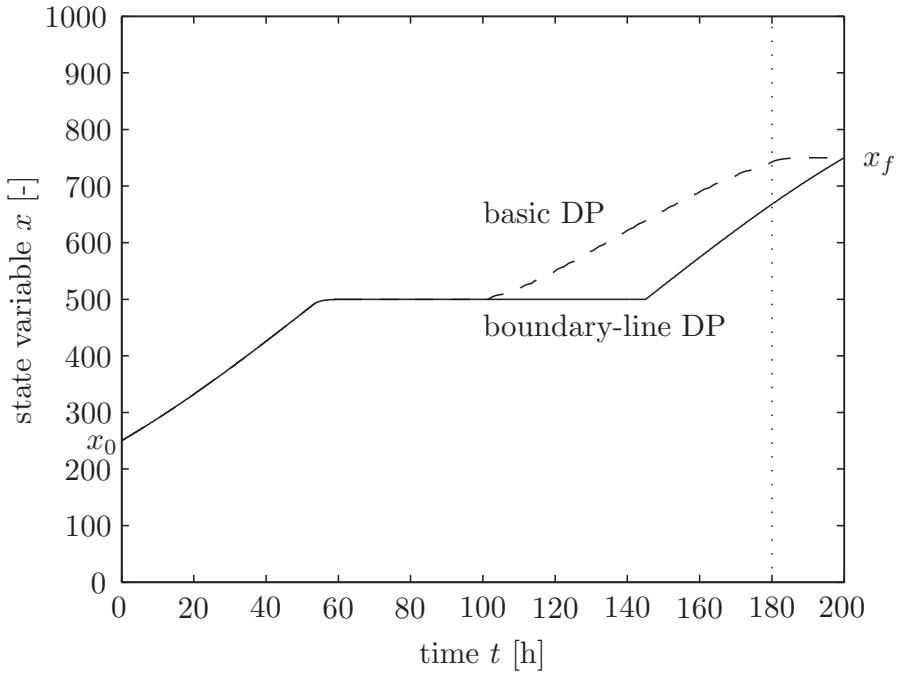

Figure 4.3: State trajectories from DP for the fishing problem. The solid line shows the result based on the boundary-line method. The dashed line is the state trajectory resulting from the basic DP. The dotted vertical line at $t = 180$ h indicates the time where Fig. 4.2 is evaluated. State-space discretization is $\Delta x = 10$, penalty for infeasible states is set to $\mathcal{J}_\infty = 1200$.

method to improve the DP by accounting for this boundary line. This improved DP is referred to as *boundary-line DP*.

Throughout this section, equation (4.8) is reformulated as

$$x_{k+1} = f_k(x_k, u_k) + x_k, \qquad k = 0, 1, \ldots, N-1 \tag{4.14}$$

where

$$f_k(x_k, u_k) = F_k(x_k, u_k) - x_k. \tag{4.15}$$

4.3.1 Computation of the Boundary Line

There exist infeasible regions in the state-time space of an optimization problem with fixed final time and a partially constrained final state if the state dynamics are bounded. Since the dynamic system is assumed to be one-dimensional, there exist only two infeasible regions, namely an upper

and a lower region. This is depicted in Fig. 4.1. In this section, the lower boundary line between the feasible and the infeasible region is derived. The upper boundary line is found analogously.

The partially constrained final state is given by (4.4). The lower boundary line is defined as the lowest state $x_{k,low}$ at each time instance k that allows achieving the minimal final state $x_{f,min}$. Note that the lower boundary line is only discretized in time, i.e., it is continuous in the state variable. The lower boundary line can be evaluated by sequentially going backward in time from $k = N - 1$ to $k = 0$ and solving the following optimization problem at each time instance k

$$\min_{x_{k,low},u_k} \quad x_{k,low} \tag{4.16}$$

$$\text{s.t.}$$

$$f_k(x_{k,low}, u_k) + x_{k,low} = x_{k+1,low} \tag{4.17}$$

$$u_k \in \mathcal{U}_k \tag{4.18}$$

$$x_{k,low} \in \mathcal{X}_k. \tag{4.19}$$

The problem is initialized with $x_{N,low} = x_{f,min}$. At each time-step, u_k and $x_{k,low}$ are the only unknowns, while $x_{k+1,low}$ is a parameter at time k. By solving (4.17) for $x_{k,low}$ and inserting it in (4.16) the following, more direct problem is obtained

$$\max_{x_{k,low},u_k} \quad f_k(x_{k,low}, u_k) \tag{4.20}$$

$$\text{s.t.}$$

$$f_k(x_{k,low}, u_k) + x_{k,low} = x_{k+1,low} \tag{4.21}$$

$$u_k \in \mathcal{U}_k \tag{4.22}$$

$$x_{k,low} \in \mathcal{X}_k. \tag{4.23}$$

If the state is assumed to be unconstrained, i.e., (4.23) is omitted, the following formulation is equivalent

$$x_{k,low} = x_{k+1,low} - \max_{u_k \in \mathcal{U}_k} f_k(x_{k,low}, u_k) \tag{4.24}$$

Equation (4.24) is a so-called fixed point problem ($x = f(x)$), where $x_{k,low}$ is the unknown.

The lower boundary line is finally found by the following algorithm:

1. Initialize with the lower bound of the partially constrained final state $x_{k,low} = x_{f,min}$.

2. Proceed backward in time for $k = N - 1, \ldots, 0$

   (a) Solve the fixed point problem (4.24) without state constraints as shown below in (4.25)–(4.27).

   (b) Check wether the solution found respects the state constraints.

   (c) If the constraints are not respected, solve the general problem (4.20)–(4.23).

   (d) Store the solution $x_{k,low}$ with the respective minimizer $u_{k,low}$ and the cost-to-go $\mathcal{J}_{k,low}$.

The fixed point problem (4.24) of time step k without state constraints can be solved with the following algorithm[3]:

1. Initialization:

$$x_{k,low}^{j=0} = x_{k+1,low} \tag{4.25}$$

2. Iteration over j until a specified tolerance is achieved:

$$x_{k,low}^{j+1} = x_{k+1,low} - \max_{u_k \in \mathcal{U}_k} \{f_k(x_{k,low}^{j}, u_k)\} \tag{4.26}$$

This algorithm converges if

$$\left| \frac{\partial}{\partial x_{k,low}^{j}} \max_{u_k \in \mathcal{U}_k} \{f_k(x_{k,low}^{j}, u_k)\} \right| < 1. \tag{4.27}$$

Note that the algorithm mentioned above (4.25)–(4.27) finds the limit value $x_{k,low}$ in the first iteration if the update function f_k is independent of the state variable x_k.

[3]The top right index of x is the iteration index, here. It is not the index of the state-grid as used in the rest of the chapter.

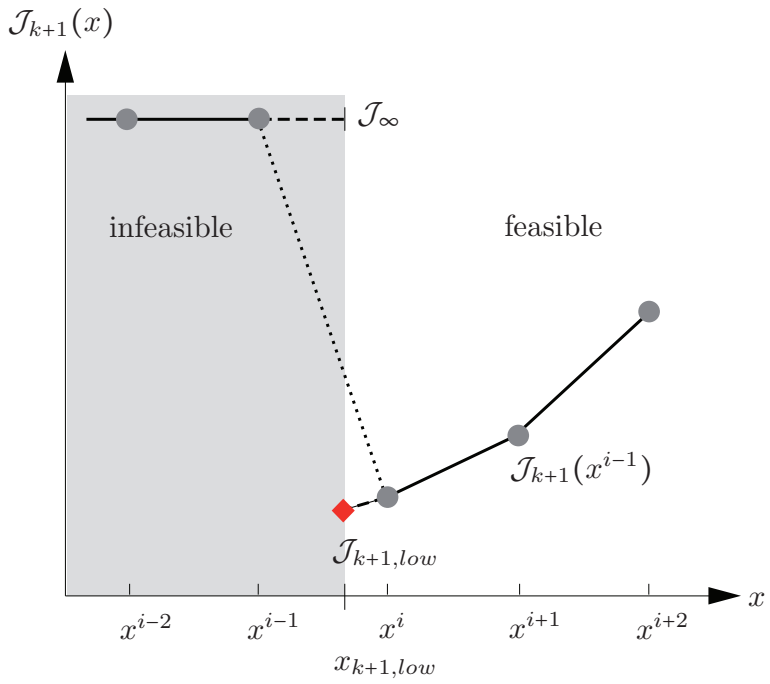

Figure 4.4: Interpolation of $\mathcal{J}_{k+1}(x)$ near the boundary line. The dashed lines illustrates the (linearly) interpolated values including the boundary line. The dotted line illustrates the interpolation used by the basic algorithm.

4.3.2 Interpolation Near the Boundary Line

It is assumed that the state boundary lines $x_{k,low}$ (and $x_{k,high}$) shown in Fig. 4.1 with their corresponding cost-to-go $\mathcal{J}_{k,low}$ (and $\mathcal{J}_{k,high}$) along the boundary line have been calculated prior to the DP algorithm. Therefore, when the set Ω_k^i contains the boundary it is possible to interpolate between the exact boundary and a feasible state grid point, as illustrated in Fig. 4.4 with the solid and the dashed lines. The dotted line illustrates the interpolation by the basic algorithm at the boundary between feasible and infeasible regions.

Consider the DP algorithm to evaluate the cost-to-go for the state-grid point x^i at time $k+1$ (see Fig. 4.1, bottom). Starting from state x^i, the state achieved at the end of this time-step

$$x_{k+2} = f_{k+1}(x^i, u_{k+1}) + x^i \qquad \in \Omega_{k+1}^i \tag{4.28}$$

can reach the feasible as well as the infeasible region. The corresponding

cost-to-go $\mathcal{J}_{k+2}(x_{k+2})$ is evaluated by interpolation between $\mathcal{J}_{k+2}(x^{i+1})$ and $\mathcal{J}_{k+2,low}$ if the state x_{k+2} is above or on the boundary line $x_{k+2,low}$. Otherwise, the cost-to-go is set to infinity or to the big, finite value $\mathcal{J}_\infty$. This procedure allows maintaining the same accuracy close to the boundary line as achieved within the feasible domain.

The application of the optimal control signal map in the forward simulation which is mentioned in Section 4.1 is improved by the boundary line analogously. Since the control signal on the boundary line was evaluated before, interpolation of the control signal is carried out between the grid points of the feasible domain or between the feasible domain and the boundary line.

4.4 Example: Lotka-Volterra Fishery

This section studies a well-known optimal control problem, namely the optimal fishing in a Lotka-Volterra fish population [56]. The fishing problem is chosen because it has an analytic solution.

4.4.1 Continuous-Time Problem

The continuous-time dynamic Lotka-Volterra system is

$$\dot{x}(t) = \frac{2}{100} \cdot \left(x(t) - \frac{x^2(t)}{1000} \right) - u(t), \tag{4.29}$$

where the state variable $x(t)$ is the amount of fish in a lake, the control signal $u(t)$ is the fishing rate. The control signal $u(t)$ is limited to $u(t) \in [0,\ 10]$. For the considered system the state $x(t)$ is limited to $x(t) \in [0,\ 1000]$ since

$$\lim_{\substack{t\to\infty \\ u(t)=0}} x(t) = 1000. \tag{4.30}$$

The objective is to maximize the amount of fish caught, which is equivalent to minimizing

$$J = \int_0^{t_f} -u(t)dt \tag{4.31}$$

within a fixed time t_f while the minimal amount of fish in the population at the final time must be $x_{f,min} = 750$. This can be stated as the optimal control problem

$$\min_{u(t)} \int_{t=0}^{t_f} -u(t)dt \tag{4.32}$$

s.t.

$$\dot{x}(t) = \frac{2}{100} \cdot \left(x(t) - \frac{x^2(t)}{1000} \right) - u(t) \tag{4.33}$$

$$x(0) = 250 \tag{4.34}$$

$$x(t_f) \geq 750 \tag{4.35}$$

$$x(t) \in [0,\ 1000] \tag{4.36}$$

$$u(t) \in [0,\ 10] \tag{4.37}$$

$$t_f = 200. \tag{4.38}$$

The solution to this optimal control problem is straightforward to determine and consists of three parts: First, there is no fishing to let the population grow, then there is fishing such that the population is kept constant, then there is no fishing again to let the population grow to the final condition. The optimal control expressed in time is

$$u^o(t) = \begin{cases} 0 & \text{if} \quad t \in [0,\ t_a] \\ 5 & \text{if} \quad t \in (t_a,\ t_f - t_b) \\ 0 & \text{if} \quad t \in [t_f - t_b,\ t_f] \end{cases} \tag{4.39}$$

where

$$t_a = t_b = 100 \cdot \operatorname{artanh}\left(\frac{1}{2}\right). \tag{4.40}$$

The final maximum amount of fish caught is

$$\begin{aligned} J^o_{analytic} &= -5 \cdot (t_f - t_a - t_b) \\ &= -1000 \cdot \left(1 - \operatorname{artanh}\left(\frac{1}{2}\right)\right) \\ &\approx -450.694 \end{aligned} \tag{4.41}$$

4.4.2 Discrete-Time Problem

In order to evaluate the optimal solution by means of dynamic programming, the continuous-time state dynamics (4.29) must be discretized. Using an Euler forward approximation with a time step $t_s = 0.2$ h, the discrete-time model is

$$x_{k+1} = f(x_k, u_k) + x_k, \qquad k = 0, 1, \ldots, N-1 \tag{4.42}$$

where

$$f(x_k, u_k) = t_s \cdot \left(\frac{2}{100} \cdot \left(x_k - \frac{x_k^2}{1000} \right) - u_k \right). \tag{4.43}$$

The state x_k is the amount of fish in a lake, while the control signal u_k is the constant fishing rate during one time step. The discrete-time optimal control problem is

$$\min_{u_k \in [0,\ 10]} \sum_{k=0}^{N-1} -u_k \cdot t_s \tag{4.44}$$

s.t.

$$x_{k+1} = f(x_k, u_k) + x_k \tag{4.45}$$

$$x_0 = 250 \tag{4.46}$$

$$x_N \geq 750 \quad (= x_{f,min}) \tag{4.47}$$

$$x_k \in [0,\ 1000] \tag{4.48}$$

$$N = \frac{200}{t_s} + 1. \tag{4.49}$$

As mentioned in Section 4.2, use of a big, but finite value $\mathcal{J}_\infty$ to penalize infeasible states improves the numerics. This value should be chosen as small as possible, but larger than any value of the (feasible) cost-to-go that could occur. Since this simple example allows for analytic solutions, the maximum cost-to-go of the continuous-time problem is evaluated in order to choose a suitable value for $\mathcal{J}_\infty$. The minimum of the cost-to-go $\mathcal{J}_t(x)$ is obviously at $t = 0$ and $x = 1000$ and yields

$$\begin{aligned} \mathcal{J}_{t=0}(x = 1000) &= 500 \operatorname{artanh}\left(\frac{1}{2}\right) - 1000 - 125\pi \\ &\approx -1118 \end{aligned} \tag{4.50}$$

For the fishing problem, at $t = 0$, the minimum cost-to-go (4.50) is approximately 1118 less than the cost-to-go at $t = t_f = 200$

$$\mathcal{J}_{t=200}(x \in \mathcal{X}_{t=200}) = 0. \tag{4.51}$$

The infeasible states at t_f must therefore be penalized by a value larger than 1118 to ensure that the final state constraint is met.

Consequently, the penalty $\mathcal{J}_\infty$ used for the cost-to-go of infeasible states is set to a value greater than $\mathcal{J}_\infty > 1118$. For the example here a value of

$$\mathcal{J}_\infty = 1200 \tag{4.52}$$

is chosen and is used in the DP algorithm.

The output of the dynamic programming algorithm is an optimal control signal map, specifying the optimal control signal at each time step k and each state $x_k \in \mathcal{X}_k$. The optimal control signal map for the Lotka-Volterra system is shown in Fig. 4.5. It shows that in the beginning of the problem the optimal control is "not fishing" ($u = 0$) if the fish population is small ($x < 500$), "moderate fishing" ($u = 5$) if the population is $x = 500$ and "full fishing" ($u = 10$) if the population is large ($x > 500$). Toward the end of the problem, one must stop fishing as late as possible, such that the population reaches the specified minimum final size of $x_{f,min} = 750$. The resulting optimal state trajectory, i.e., the fish population for an initial state of $x_0 = 250$ is shown as the black solid line. The solution of the dynamic programming clearly reflects the optimal control found for the continuous problem (4.39).

4.4.3 Resolution Study

As mentioned earlier, the accuracy of the solution obtained with dynamic programming can degrade due to numeric issues. The state space must be discretized for the DP algorithm. The resolution of the state-space discretization is a critical quantity. On one hand, the computational effort increases with a higher resolution. On the other hand, the accuracy of the solution improves with increasing resolution.

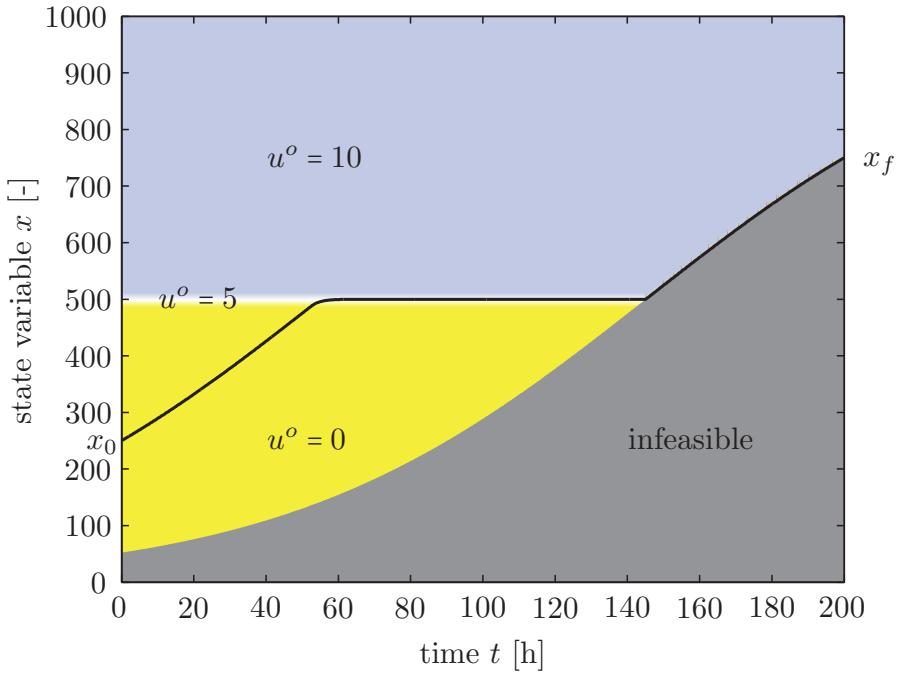

Figure 4.5: The optimal control signal map, determined using dynamic programming, for the discrete-time Lotka-Volterra system. The optimal state trajectory for $x_0 = 250$ when using the map is shown as the solid black line.

Therefore, a study is carried out here to quantify the accuracy of the solution obtained by DP for the simple example of the fishing problem. The fishing problem has been chosen because an analytic solution exists that can be used as a benchmark. The resolution study is carried out for the basic DP, but also for the new method presented in this chapter, i.e., the boundary-line DP.

The quality of the solution is expressed as the relative difference between optimal cost obtained by DP and the analytic optimal solution, $\frac{J^o_{analytic} - J^o_{dp}}{J^o_{analytic}}$. Figure 4.6 shows this deviation of the optimal solution evaluated with DP (basic and boundary-line) from the analytic optimal solution.

Since the analytic solution is evaluated for the original continuous-time problem, the discrete-time solution can never achieve the analytic optimal solution. This discretization error is indicated in Fig. 4.6 with the dotted line marked as "minimum time-discretization error". It emphasizes that the solution using the boundary-line DP converges well toward the discrete-time optimum. Furthermore, this figure illustrates the importance of the boundary line: the numeric solution with the boundary-line DP is closer

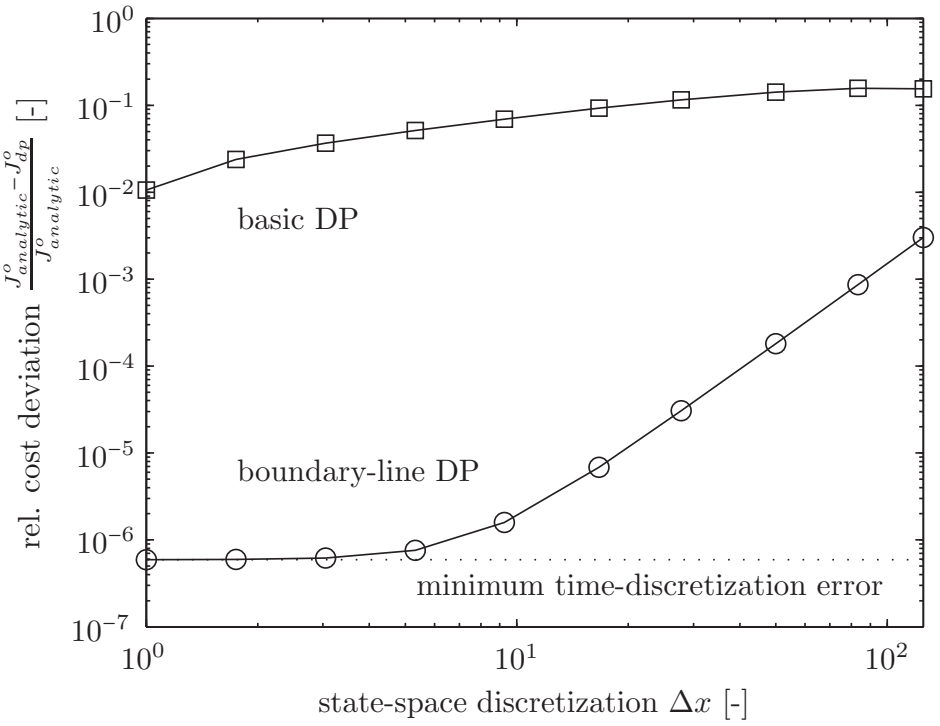

Figure 4.6: The relative deviation of the cost computed by dynamic programming compared to the optimal analytic solution for the fishing problem.

to the analytic solution by a factor of 50 to 68000 than with the basic DP for the same resolution. It is interesting to note that the cost (4.44) resulting from boundary-line DP is inferior to the cost resulting from basic DP over the entire range of resolution that was investigated. The solution using the boundary-line DP at the lowest resolution (Δx = 125) is closer to the analytic solution than the solution of the basic DP at the highest resolution (Δx = 1).

The relative deviation of the final state achieved by the DP (basic and boundary-line) from the optimal final state is shown in Fig. 4.7 for different resolutions. The optimal final state is the lowest admissible final state for this example, i.e., $x^o(t_f) = x_{f,min}$. The figure shows clearly that the final state deviation of the basic DP decreases with decreasing Δx, i.e., with increasing resolution. Using the boundary-line DP, the final state deviation is negligible over the entire range of resolutions investigated here.

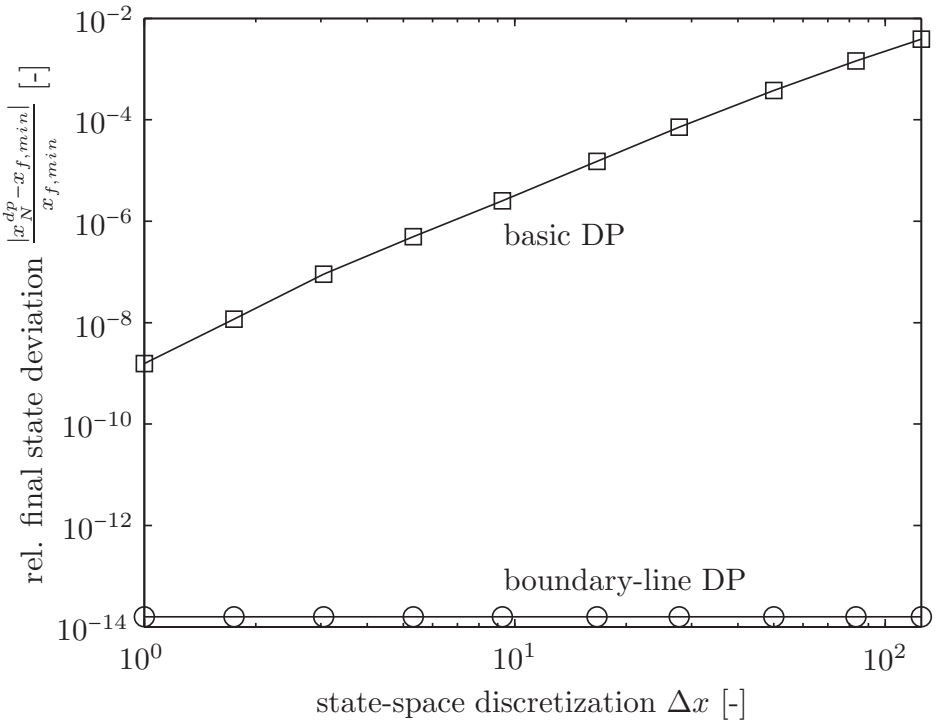

Figure 4.7: The relative deviation of the actual final state and the optimal final state for the fishing problem.

4.4.4 Computational Effort

The computational effort of an optimization method is often a crucial factor that determines whether a method is being applied in practice for a given problem or not. Therefore, not only the accuracy of a solution as shown in Section 4.4.3 is relevant, but also the corresponding computational cost.

The number of model-function evaluations for the basic DP with an equally spaced grid is given by

$$N_{feval}^{DPbasic} = N_x \cdot N_u \cdot N. \tag{4.53}$$

This is only true for a single-dimensional state space and a scalar control signal. The variable N_x represents the number of grid points for the state space, N_u for the control signal, and N for the time discretization.

When using the boundary-line DP, the infeasible domain is well known. Consequently, the computation for the grid points in this infeasible domain (see Fig. 4.1) can be omitted [37]. The number of infeasible grid points

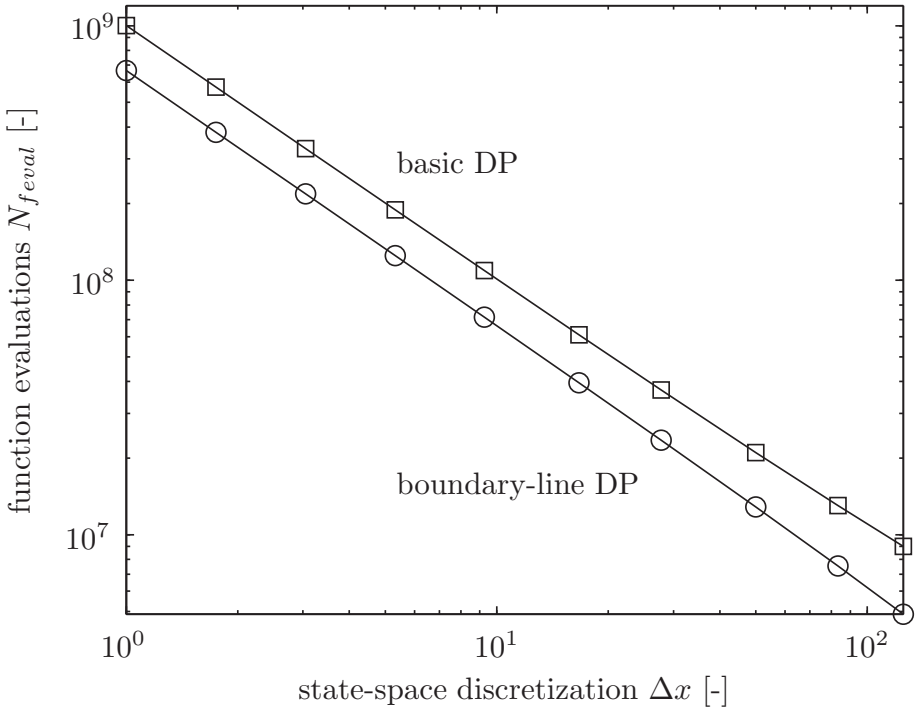

Figure 4.8: Number of function evaluations needed to find the solution of the fishing problem.

at a time step k is denoted as $N_{k,x}^{infeas}$. Hence, the number of function evaluations that can be saved are

$$N_{feval}^{infeas} = N_u \cdot \sum_{k=0}^{N-1} N_{k,x}^{infeas}. \tag{4.54}$$

The cost for evaluating the boundary line cannot be neglected. The number of function evaluations needed to compute the line is denoted by N_{feval}^{line}.

Consequently, the number of function evaluations required for solving the DP with the boundary-line method is given by

$$N_{feval}^{DPline} = N_{feval}^{DPbasic} - N_{feval}^{infeas} + N_{feval}^{line}. \tag{4.55}$$

Figure 4.8 shows the number of function evaluations for the fishing problem over the discretization step Δx. It shows that more computations can be saved due to the infeasible domain than are required to evaluate the boundary line. The boundary-line DP requires fewer function evaluations by a factor of 1.5 to 1.85 than the basic DP over the entire range of discretization steps investigated here. Furthermore, it should be recalled that

Table 4.1: Comparison at similar accuracy for the fishing problem

		basic DP	boundary-line DP
state-space discretization [-]	Δx	1	125
amount of fish caught [-]	$-J$	445.936	449.340
function evaluations [-]	N_{feval}	1002001000	4877143

the accuracy of the solution is considerably higher, even though the computational burden is lower.

More interesting is a comparison of solutions of similar accuracy. Therefore, the solution using the basic DP at the lowest discretization step of $\Delta x = 1$ is compared to the solution of the boundary-line DP at its highest discretization step of $\Delta x = 125$. The values obtained are shown in Table 4.1. These results reveal that the boundary-line DP is computationally more efficient by a factor of $\frac{1002001000}{4877143} \approx 205$ than the basic DP, even though the accuracy of the solution is still better ($449.340 > 445.936$). This result motivates to apply the method to more complex systems.

4.5 DPM-Function

In this section a Matlab function is introduced that solves dynamic programming problems using the theories presented in the previous section. The function is call Dynamic Programming Matrix (DPM) function. The `dpm` function solves the discretized version of the optimal control problem (4.1)–(4.7). This section shows the syntax and commands for solving such problems. In particular, the syntax is shown for two simple optimal control problem. The `dpm` function can be downloaded at [57].

When solving discrete-time optimal control problems the `dpm` function is normally called using

```
[res dyn] = dpm(fun, par, grd, prb, options);
```

where `fun` is the model function handle, `par` is any user defined parameter structure that is forwarded to the model, `grd` is the grid structure, `prb` is the problem structure, and `options` is the option structure. The output of the `dpm` function are normally two structures representing the DP-output and the signals from forward simulation of the model using the optimal control input map.

Since the DP algorithm is often time consuming, the `dpm` function can also be used only for forward simulation when the DP output structure `dyn` is precalculated. This can be very useful when changing the initial condition or when increasing the starting time `N0` of the problem. To call the `dpm` function when the DP output structure is already calculated use

```
res = dpm(dyn, fun, par, grd, prb, options);
```

All the structures in the code above are further explained in the remainder of this section.

4.5.1 Problem Formulation

In the problem structure all necessary parameters that define the problem are given. The important parameters are the time step `Ts` of the model description and the problem length `N`. Moreover, in the problem structure an optional cell array can be defined, which contains time-variant information relevant for the problem description. For example, if the model explicitly depends on the time the cell array `W{1}` would contain a time vector with `N` elements. The corresponding elements in these time-variant vectors are forwarded to the model function throughout the problem. The problem structure can also contain a starting time index where the forward simulation starts. This can be helpful when searching for a time optimal solution. An overview of the problem structure is shown in Table 4.2.

Table 4.2: Problem-structure (prb)

Syntax	Description
`Ts`	time step (is passed to the model function)
`N`	number of time steps in problem (integer that defines the problem length)
`N0`	(optional) start time index (only used in forward simulation)
`W{.}`	(optional) vectors with length `N` containing time-variant data for the model

Table 4.3: Grid-structure (grd)

Syntax	Description
`Nx{.}`	number of grid points in state grid
`Xn{.}.lo`	lower limits for each state (vector for time-variant or scalar for fixed)
`Xn{.}.hi`	upper limits for each state (vector for time-variant or scalar for fixed)
`XN{.}.lo`	final state lower constraints
`XN{.}.hi`	final state upper constraints
`X0{.}`	inital value (only used in forward sim)
`Nu{.}`	number of grid points in input grid
`Un{.}.lo`	(optional) upper limits for each input (vector for time-variant or scalar for fixed)
`Un{.}.hi`	(optional) upper limits for each input (vector for time-variant or scalar for fixed)

4.5.2 State/Input Grids and Constraints

The grid structure `grd` contains all the information about the state and input grids and constraints. An overview of the `grd` structure is shown in Table 4.3. The `grd` structure is composed by cell arrays, where there is a cell for each state variable and each input variable. For example, for a problem with two state variables the `grd` structure contains `grd.X{1}`, `grd.X{2}`, `grd.Xn{1}.lo`, `grd.Xn{2}.lo`, and so on. The input grid is used in a similar way depending on the number of input variables of the problem.

4.5.3 Options Structure

The DP approach can be used for many different problem settings and the options structure defines how to use the algorithm. An overview of the options that can be specified in the `options` structure is shown in Table 4.4. The `HideWaitbar` options decides if waitbars are shown or not when running the DP algorithm. The `SaveMap` option determines if the optimal cost-to-go is saved and returned. Note that the memory requirements increase when `SaveMap=1`.

An important option is the `UseLine` option, which decides if the boundary line method, introduced in Section 4.3, is used or not. The boundary line method is very useful for increasing the accuracy of problems with final state constraints. Note in the actual version of the `dpm` function it can only be used when there is only one state variable. If the boundary line method is used, i.e., if `UseLine=1`, there are three additional options `Iter`, `Tol`, and `FixedGrid` that must be defined. The options `Iter` and `Tol` determines the stopping criteria when numerically inverting the model function. The option `FixedGrid` decides whether to adjust the grid to the boundary lines or fix the grid to the definition in `grd`.

Finally, the `InfCost` is the cost of infeasible states and inputs of the model. When not using the boundary line method `InfCost` is also used to enforce the final state constraints in (4.9), with $\phi_N(x_N)$ =`InfCost` when $x_N \notin [x_{f,min},\ x_{f,max}]$.

Table 4.4: Options-structure (options)

Syntax	Description
`HideWaitbar`	hide waitbars (0/1)
`Warnings`	show warnings (0/1)
`SaveMap`	save cost-to-go map (0/1)
`UseLine`	use boundary line method (0/1)
`FixedGrid`	(used if `UseLine=1`) using the original grid as specified in `grd` or adjust the grid to the boundary lines (0/1)
`Iter`	(used if `UseLine=1`) maximum number of iterations when inverting model
`Tol`	(used if `UseLine=1`) minimum tolerance when inverting model
`InfCost`	a large cost for infeasible states (`I=1`)
`Minimize`	(optional) minimizing (or maximizing) cost function (0/1) default is minimizing
`InputType`	(optional) string with the same number of characters as number of inputs. Contains the character 'c' if input is continuous or 'd' if discrete (default is all continuous).
`gN{1}`	(optional) Cost matrix at the final time (must be of `size(options.gN{1}) = [grd.Nx{1} grd.Nx{2} ... grd.Nx{.}]`)

Table 4.5: DP output-structure (dyn)

Syntax	Description
`B.hi`	`Xo`,`Uo{.}`,`Jo` contains the cost, input, and state for the upper boundary line
`B.lo`	`Xo`,`Uo{.}`,`Jo` contains the cost, input, and state for the lower boundary line
`Jo{.,.}`	optimal cost-to-go (indexed by input number and time index)
`Uo{.,.}`	optimal control input (indexed by input number and time index)

Table 4.6: Results-structure (res)

Syntax	Description
`X{.}`	state trajectories
`C{.}`	cost trajectory
`I`	infeasible vector (problem is not solved if nonzero elements)
`signals`	structure containing all the signals that were saved in the model function

4.5.4 Output Structure

The outputs of the `dpm` function are two structures, namely `res` and `dyn`. The `res` structure contains the results from the forward simulation of the model when applying the optimal control input map. The `dyn` structure is associated with the dynamic programming algorithm, the optimal cost-to-go, and the optimal control input map. When the boundary line method is used the `dyn` structure also contains the boundary lines (with the states, inputs, and costs). An overview of the two structures are shown in Tables 4.5 and 4.6.

4.5.5 Model Structure

The equations describing the model must be implemented in a correct format in order to be used with the `dpm` function. To generate a sample function use the command

```
dpm('sample_model',Nx,Nu);
```

This command will save an m-function as `sample_model.m` with a random model of `Nx` state variables and `Nu` input variables, suitable for usage with the `dpm` function, which can be used as a template when developing a new problem description.

In general the model function should have the format:

```
function [X, C, I, signals] = mymodel(inp,par)
```

where the model input structure `inp` is generated by the `dpm`-function and contains the elements in Table 4.7. The structure `par` can contain any user defined parameters necessary in the model function. It is important that the model function preserves the size of the inputs to the outputs. Consequently, the elements `inp.X{.}`, `inp.U{.}` and the outputs `X{.}`, `C{.}`, and `I` must have the same size. The structure `signals` can contain any user defined internal signals in model. These signals are stored during the forward simulation and returned in the `res` structure when calling the `dpm`-function, Table 4.6.

Table 4.7: Input-structure (inp)

Syntax	Description
`X{.}`	current states (n+m dimensional matrix form depending on the number of inputs and state variables)
`U{.}`	current inputs (n+m dimensional matrix form depending on the number of inputs and state variables)
`W{.}`	current time-variant data (scalar)
`Ts`	time step

Table 4.8: Model outputs

Syntax	Description
`X{.}`	resulting states after applying `inp.U{.}` at `inp.X{.}` (same size as `inp.X{.}`)
`C{.}`	resulting cost of applying `inp.U{.}` at `inp.X{.}` (same size as `inp.X{.}`)
`I`	set with infeasible combinations (feasible=0, infeasible=1) (same size as `inp.X{.}`)
`signals`	structure with user defined signals (same size as `inp.X{.}`)

4.6 Examples

To illustrate the usefulness of the `dpm` function, two examples are discussed below. First, the well-known Lotka-Volterra fishery problem [56] is explained and solved using the `dpm` function. Of course, there exist an analytic solution to the continuous-time Lotka-Volterra fishery problem, and it is therefore not necessary to use a DP algorithm to solve it. However, since this problem is simple and is similar to the problems normally solved with DP, it is used as an example to illustrate the syntax of the `dpm` function. Second, an example of an optimal energy management problem for a parallel hybrid-electric vehicle is solved using the `dpm` function. This problem is well suited for the DP algorithm. Not surprisingly, DP has been used extensively proposed in the literature to solve such energy management problems, both for comparison to causal controllers and for

evaluation of different system configurations. Some examples are [58], [59], [60], and [5].

In the first example of the Lotka-Volterra fishery problem the entire code necessary to use the `dpm` function is shown. In the hybrid-electric vehicle example, however, the model function contains far too many lines to be included in this thesis. Interested readers can download the complete model equations at [57].

4.6.1 Lotka-Volterra Fishery

In order to evaluate the optimal solution to the Lotka-Volterra fishery problem introduced in Section 4.4 the model function (4.42) is implemented in Matlab as:

```
function [X, C, I, signals] = fishery(inp,par)

% state update
func = (0.02.*(inp.X{1}-inp.X{1}.^2/1000)-inp.U{1});
X{1} = inp.Ts.*func + inp.X{1};

% cost
C{1} = -inp.Ts.*inp.U{1};

% infeasibility
I = 0;

signals.U{1} = inp.U{1};
```

Since the state and input spaces have to be discretized, the `dpm` function includes a simple way to define such grids. Let the state variable be limited between 0 and 1000 and let it be discretized using a step of 5 such that

$x_k \in \{0, 5, 10, ..., 995, 1000\}$. Also, let the control input variable be limited between 0 and 10 and let it be discretized with a step of 0.5 such that $u_k \in \{0, 0.5, 1, ..., 9.5, 10\}$. The optimal control problem (4.44)–(4.49) is then solved with the `dpm` function using:

```
grd.Nx{1}    = 201;
grd.Xn{1}.lo = 0;
grd.Xn{1}.hi = 1000;
grd.Nu{1}    = 21;
grd.Un{1}.lo = 0;
grd.Un{1}.hi = 10;

% set initial state
grd.X0{1}    = 250;

% set final state constraints
grd.XN{1}.hi = 1000;
grd.XN{1}.lo = 750;

% define problem
prb.Ts = 1/5;
prb.N  = 200*1/prb.Ts + 1;

% set options
options = dpm();
options.UseLine   = 1;
options.SaveMap   = 1;
options.InfCost   = 1200;
options.FixedGrid = 1;

[res dyn] = dpm(@fishery,[],grd,prb,options);
```

The output of the DP algorithm is an optimal control signal map, specifying the optimal control signal at each time step k and at each state $x_k \in \mathcal{X}_k$. The optimal control signal map for the Lotka-Volterra system is shown in Fig. 4.5. It shows that the optimal control is "not fishing" $u = 0$ if the fish population is small $x < 500$, "moderate fishing" $u = 5$ if the population is $x = 500$ and "full fishing" $u = 10$ if the population is large $x > 500$. Toward the end of the problem, one must stop fishing as late as possible, such that the population reaches the specified minimum final size of $x_{f,min} = 750$. The resulting optimal state trajectory, i.e., the fish population for an initial state of $x_0 = 250$, is shown in Fig. 4.5 by the black solid line.

4.6.2 Hybrid-Electric Vehicle Example

The energy consumption of hybrid-electric vehicles can be described well using a quasi-static discrete-time models. The modeling follows the ideas described in [20, 61]. Essentially, the model contains the battery state-of-charge as the only state variable. In a nutshell, the combustion engine is modeled using an affine Willans approximation [62], the electric motor is modeled using an electric-power map (derived from detailed simulations), and the battery is modeled as a voltage source together with a resistance in series. The vehicle model includes air drag, rolling friction, and inertial forces. The gearbox is modeled using a constant efficiency of 95%. The hybrid vehicle considered in this study has a 20% hybridization as defined in [4].

The model equations can be summarized and described as

$$\xi_{k+1} = f(\xi_k, u_k, v_k, a_k, \varphi_k) + \xi_k, \tag{4.56}$$

where ξ_k is the battery state-of-charge, u_k is the torque split factor, v_k is the vehicle speed, a_k is the vehicle acceleration, and φ_k is the gear number. The model assumes isothermal conditions of the components, no extra fuel consumption during the startup of the combustion engine, and no energy losses during gear shifting. A constant auxiliary electric power demand of 350 W is used in the model.

Since the drive cycle is assumed to be known in advance the particular

driving speed v_k, acceleration a_k and gear number φ_k at instance k can be included in the model function to form the time-variant model:

$$\xi_{k+1} = f_k(\xi_k, u_k) + \xi_k, \qquad k = 0, 1, \ldots, N-1. \tag{4.57}$$

The optimization problem of minimizing the total fuel mass consumed

$$J = \sum_{k=0}^{N-1} \overset{*}{m}_f (u_k, k) \cdot t_s \tag{4.58}$$

for the hybrid vehicle over a given drive cycle, here the Japanese 10-15 drive cycle (J1015), can be stated as the discrete-time optimal control problem:

$$\min_{u_k \in \mathcal{U}_k} \sum_{k=0}^{N-1} \overset{*}{m}_f (u_k, k) \cdot t_s \tag{4.59}$$

s.t.

$$\xi_{k+1} = f_k(\xi_k, u_k) + \xi_k \tag{4.60}$$

$$\xi_0 = 0.55 \tag{4.61}$$

$$\xi_N = 0.55 \tag{4.62}$$

$$\xi_k \in [0.4,\ 0.7] \tag{4.63}$$

$$N = \frac{660}{t_s} + 1 \tag{4.64}$$

where $\overset{*}{m}_f$ is the fuel mass consumption. The time step in this example is $t_s = 1$ s. The optimal control problem (4.59)–(4.64) is solved using DP. Figure 4.9 shows the resulting optimal control map `dyn.Uo{1,:}` and state trajectory `res.X{1}` when using the `dpm`-function as described below.

```
% create grid
grd.Nx{1}    = 61;
grd.Xn{1}.hi = 0.7;
grd.Xn{1}.lo = 0.4;
grd.Nu{1}    = 21;
grd.Un{1}.hi = 1;
grd.Un{1}.lo = -1;

% set initial state
grd.X0{1}    = 0.55;

% final state constraints
grd.XN{1}.hi = 0.55;
grd.XN{1}.lo = 0.55;

% define problem
prb.W{1} = speed_vector;        % (661 elements)
prb.W{2} = acceleration_vector; % (661 elements)
prb.W{3} = gearnumber_vector;   % (661 elements)
prb.Ts   = 1;
prb.N    = 660*1/prb.Ts + 1;

% set options
options           = dpm();
options.UseLine   = 1;
options.SaveMap   = 1;
options.InfCost   = 1000;
options.Iter      = 5;
options.InputType = 'c';
options.FixedGrid = 0;

[res dyn] = dpm(@hev,par,grd,prb,options);
```

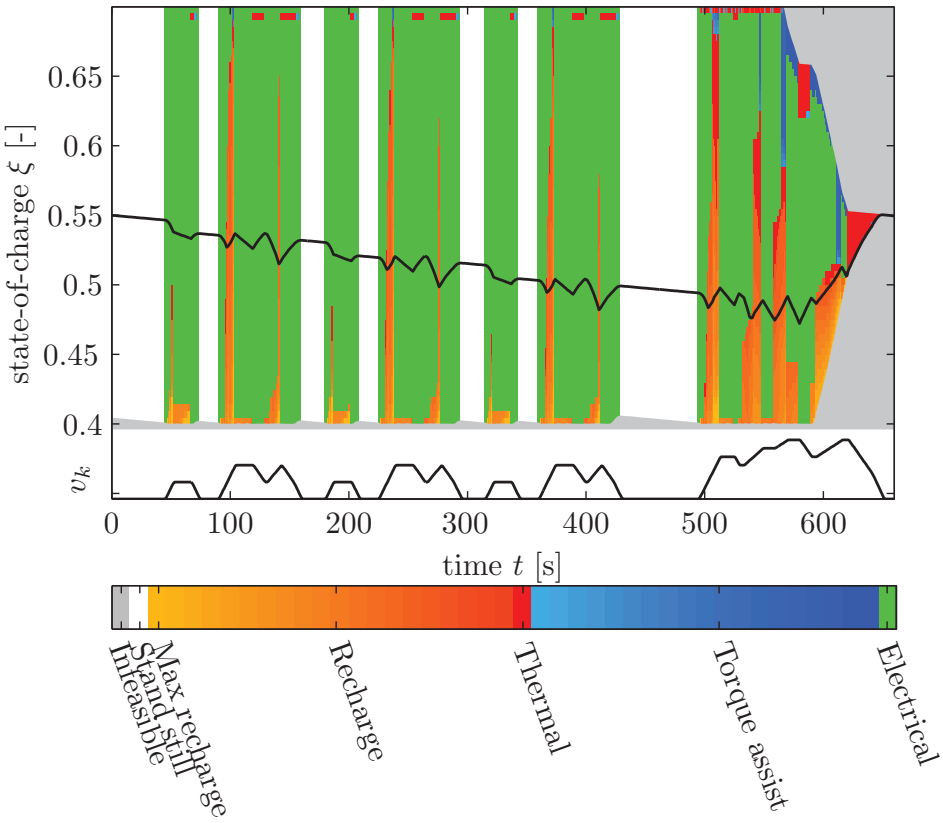

Figure 4.9: Optimal input map obtained using the DP algorithm for a full parallel hybrid-electric vehicle driving the Japanese 10-15 driving cycle. The black curve shows the optimal state-of-charge trajectory when the battery is 55% charged at the start.

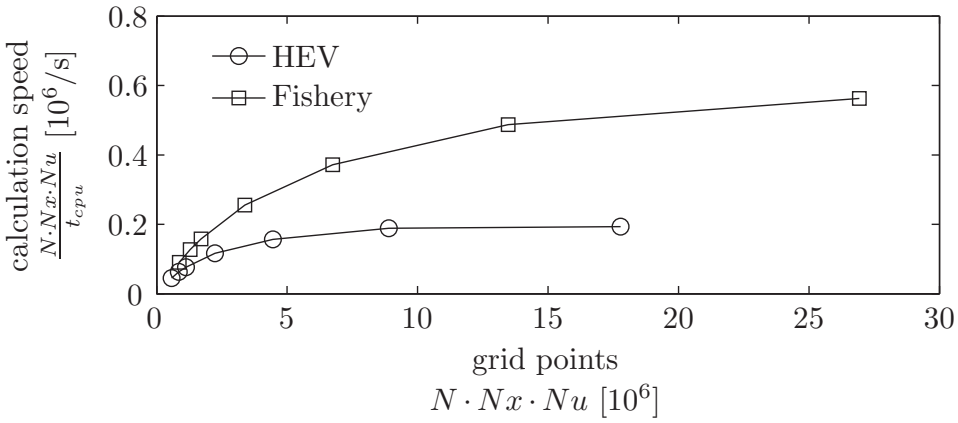

Figure 4.10: The computational cost for the two examples. The values are given in calculated grid points per second as a function of the total number of grid points.

4.7 Summary and Discussion

The boundary-line DP presented in this chapter improves the efficiency of dynamic programming considerably for the case of a single state variable. Not only the final state constraint is fulfilled at high accuracy, but also the calculated optimal cost is very close to the true solution even for a moderate resolution of the discretized state space. The computational cost is substantially reduced since the new method allows the accuracy to be maintained at a much lower state-space resolution. Furthermore, the number of calculated grid points is reduced by evaluating the feasible domain only. The method presented here improves the dynamic programming only if the optimal state trajectory is close to the bounds of the feasible region at some points. This is typically the case for constrained optimal control problems.

The novel method is well suited for optimal control of hybrid electric vehicles because the optimal trajectory coincides with the boundary line at the end of most drive cycles and because the system can be sufficiently well described with a single state variable. The resulting gain in computational time can be used for extensive parametric studies, for instance, such as optimal component dimensioning without increasing the total computational effort.

In this study, the proposed method is applied to partially constrained optimal control problems where only the lower state boundary line is determined. However, the proposed method can easily be applied to constrained optimal control problems where a lower and an upper state boundary line have to be determined.

Finally, a Matlab function is introduced that efficiently solves the deterministic DP problems. The syntax and the main features of the function are highlighted using two examples. This `dpm` function together with the model functions introduced in this chapter can be downloaded at [57]. The computational time[4] required for backward calculation for the two examples, without using the boundary line, is shown in Fig. 4.10. It shows that the function evaluates 600000 points/s for the fishery problem and 200000

[4]Calculated on a 32-bit Intel Pentium D 2.8GHz with 2.0 GB RAM.

points/s for the HEV problem. This is due to the more complex model in the HEV problem.

Future work includes the attempt of a possible extension of the boundary line method to more general problems such as multi-dimensional optimal control problems, and the support of simple discrete-time Simulink models. The main task for the near future will be to optimize the memory requirements of the function.

Chapter 5

Conclusions and Outlook

This chapter presents conclusions and future work in the field of optimal control and design of hybrid electric vehicles. The goal here is not to provide a detailed summary and conclusions since this can be found in each of the previous chapters. The goal is rather on providing general conclusions of this thesis and on providing an broad outlook of research areas that should be further explored.

5.1 Conclusions

In this thesis the energy management problem in hybrid electric vehicles is studied. A mathematical approach is used and the explicit optimal control is derived for a simplified model of a full hybrid. The derivation shows how an optimal strategy is structured and how vehicle parameters affect the strategy. The explicit optimal control is used to derive an energy management strategy, where the equivalence factor is updated by a causal controller. The formulation of the simplified model further allowed to analytically derive a saturation in the equivalence factor that can be used to implement an anti-windup scheme in a causal equivalence factor controller.

This thesis also shows a novel state-of-charge controller for a torque-assist hybrid equipped with an automatic manual gearbox. The benefit of the proposed controller is the clear separation between the torque-split

control and the gear choice. This study shows that the torque split, which is normally used to control the state-of-charge of the battery, can be implemented as a simple rule while the gear choice is used as supervisory control to influence the battery state-of-charge. The proposed controller is robust when regarding different hybridization ratios. Moreover, the proposed controller is also robust to the limitations and energy losses normally present in automated manual gearboxes.

The thesis also investigates the optimal design of hybrid vehicles and in particular the optimal hybridization ratio of parallel hybrid vehicles. This investigation shows that the hybridization need is in fact lower in a full parallel hybrid than in a torque-assist hybrid. A novel method to optimize the hybridization ratio in a torque-assist hybrid is also presented. The method achieves close to optimal solutions while substantially reducing the computational time required to determine the solution. This method is the starting point for the development of the dual clutch transmission gear shifting strategy for the torque-assist hybrid. It is important to note the connection between the method for optimizing the hybridization ratio in the torque-assist hybrid and the gear shifting energy management strategy.

Dynamic programming is used as a tool throughout this thesis. A novel method is presented to improve the accuracy of the dynamic programming solution and therefore also to increase the possibility to reduce the computational requirements. The tool has been implemented in Matlab and is available online for interested researchers and students. The tool is not restricted to the energy management problem of hybrid vehicles, but has also been successfully applied to vehicle parking problems, intelligent cruise control problems, and engine emission control problems.

5.2 Outlook

There are several areas where the research in this thesis can be further explored. The dynamic programming tool should be further developed to reach a broader audience. In particular the boundary-line method, used to enhance the accuracy of dynamic programming, should be extended to multiple dimensions.

Furthermore, the modeling process used to derive the simplified model for the explicit optimal control can also be used for other topologies. The simplest extension is for the series hybrid where some additional efficiencies would be added to the model before the optimal control derivation. Insights like the anti-windup scheme can therefore also be found for other topologies.

Moreover, the simplified model can be used to explicitly prove that the optimal hybridization ratio is indeed lower in a full hybrid than in a torque-assist hybrid. If appropriate assumptions on power constraints and powertrain parameters are made a general proof could be developed.

Since the results and methods described in this thesis rely on simulations the obvious extension to this work is to validate the results, where possible, also with actual hybrid vehicle measurements.

Appendix A

Hybrid Electric Vehicle Model

The hybrid electric vehicle model is a quasi-static discrete-time model. The modeling process follows the theories in [20] and [61]. The model can be described as

$$\boldsymbol{x}_{k+1} = F(\boldsymbol{x}_k, \boldsymbol{u}_k, \boldsymbol{w}_k) \tag{A.1}$$

where normally the state vector $\boldsymbol{x}$, input vector $\boldsymbol{u}$, and disturbance vector $\boldsymbol{w}$ are

$$\boldsymbol{x}_k = [\xi_k]^T \tag{A.2}$$
$$\boldsymbol{u}_k = [u_{s,k}]^T \tag{A.3}$$
$$\boldsymbol{w}_k = [v_k,\ a_k,\ \varphi_k]^T, \tag{A.4}$$

where ξ_k is the battery state-of-charge, $u_{s,k}$ the torque split factor, v_k the vehicle speed v_k, a_k the vehicle acceleration, and φ_k the gear number. Throughout this study a time step of one second has been used $t_s = 1$ s. The model is separated into the subsystems; vehicle, final drive, gearbox, internal combustion engine, electric motor, and battery. The equations describing the subsystems are shown in the following sections.

A.1 Vehicle Model

The vehicle model is based on a vehicle with a nominal mass of $m_0 \approx$ 1500 kg equipped with a 1.6 liter internal combustion engine (totally $m_0 +$

$m_e \approx 1610$ kg). The total mass of the vehicle is

$$m_v = m_0 + m_e + m_m + m_b, \tag{A.5}$$

where the engine mass m_e, motor mass m_m, and battery mass m_b all depend on the specific component sizes.

The vehicle speed v_k and acceleration a_k are given by the drive cycle. The outputs of the model are the wheel rotational speed ω_w, wheel rotational acceleration $\Delta\omega_w$, and the wheel torque T_w. The outputs are determined from the inputs using the following equations

$$\omega_w = v_k / r_w \tag{A.6}$$

$$\Delta\omega_w = a_k / r_w \tag{A.7}$$

where r_w is the wheel radius and

$$T_w = (F_f + F_a + F_i) \cdot r_w, \tag{A.8}$$

where the vehicle air drag force is

$$F_a = 0.5 \cdot \rho_{air} \cdot c_d \cdot A \cdot v_k^2, \tag{A.9}$$

and the inertial force is

$$F_i = (m_v + m_r) \cdot a_k, \tag{A.10}$$

with m_r is the moment of inertia of the drivetrain converted into an equivalent mass. The friction force is

$$F_f = m_v \cdot g \cdot (c_{r0} + c_{r1} \cdot v_k^{c_{r2}}). \tag{A.11}$$

The friction coefficients c_{r0}, c_{r1}, c_{r2}, and c_d have been identified using vehicle coastdown experiments. The vehicle model assumes no wheel slip and the road is assumed to be flat.

A.2 Gearbox Model

In the vehicle two types of gearboxes are considered. The first type is a manual six speed transmission and the second type is a six speed dual

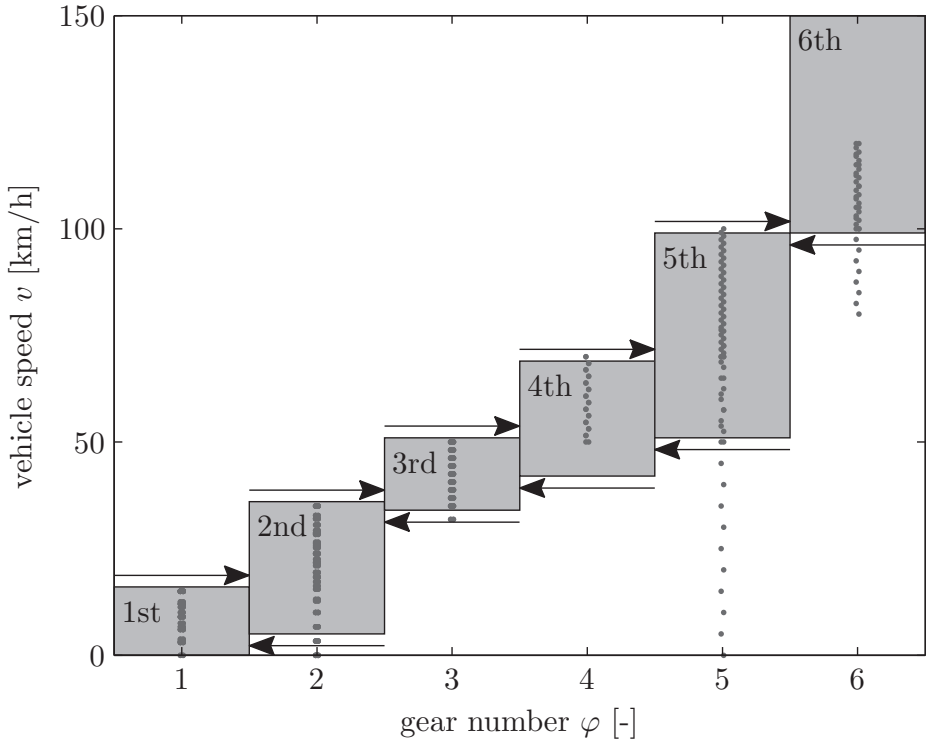

Figure A.1: The standard gear shifting strategy. The gray areas indicate the hysteresis in vehicle speed where each gear is chosen. The New European Driving Cycle shifting is shown as gray dots.

clutch transmission. Normally, when not considering an optimal gear shifting, a simple gear shifting strategy is used for both gearboxes. However, for the New European Driving Cycle the regulatory shifting strategy is used. The simple gear shifting strategy is shown in Fig. A.1. The gear shifting strategy is a simple speed dependent strategy reflecting a normal driver's behavior. The focus is not to have an optimized rule-based strategy, but rather on providing a strategy sample which can be used for comparisons. The gray dots in Fig. A.1 shows the regulatory gear shifting in the New European Driving Cycle. The New European Driving Cycle shifting is similar to the standard shifting strategy represented by the gray boxes.

Final Drive Model

The final drive is assumed to include all the gear ratios between the wheel and the gearbox output. It is assumed that there are no energy losses in

the final drive and the gearbox output torque and speed are therefore

$$T_g = \frac{T_w}{\gamma_f} \tag{A.12}$$

$$\omega_g = \gamma_f \cdot \omega_w \tag{A.13}$$

$$\Delta\omega_g = \gamma_f \cdot \Delta\omega_w. \tag{A.14}$$

where γ_f is the total gear ratio of the final drive.

Manual Transmission Model

The inputs to the manual transmission model are the gearbox output speed, gearbox output acceleration, gearbox output torque, and gear number φ_k. The outputs are the crankshaft rotational speed and acceleration together with the crankshaft torque. The gearbox efficiency is constant for all gears $\eta_{gb} = 0.95$ and thus the torque on the clutch side of the gearbox is

$$T_c = \begin{cases} \frac{T_g}{\eta_{gb} \cdot \gamma(\varphi_k)} & T_g \geq 0 \\ \frac{T_g \cdot \eta_{gb}}{\gamma(\varphi_k)} & T_g < 0 \end{cases} \tag{A.15}$$

where $\gamma(\varphi_k)$ is the gear ratio for each of the gears. The rotational speed of the crankshaft is

$$\omega_c = \gamma(\varphi_k) \cdot \omega_g \tag{A.16}$$

$$\Delta\omega_c = \gamma(\varphi_k) \cdot \Delta\omega_g. \tag{A.17}$$

The manual gearbox assumes no energy losses during gear shifting.

A.3 Internal Combustion Engine Model

The internal combustion engine model is based on an affine Willans approximation [62, 61], i.e. the brake mean effective pressure is an affine function of the fuel mean effective pressure $p_{bmep} \approx e(\omega_c) \cdot p_{fmep} - p_{bmep0}(\omega_c)$. The internal efficiency $e(\omega_c)$, friction mean effective pressure $p_{bmep0}(\omega_c)$, and maximum indicated mean effective pressure $p_{imepmax}(\omega_c)$ are all identified using engine test bench measurements of a naturally aspirated 1.6

liter gasoline direct injection engine. The engine friction torque is then given by

$$T_{e0}(\omega_c) = \frac{V_d \cdot p_{bmep0}(\omega_c)}{4 \cdot \pi}, \tag{A.18}$$

with the displacement V_d. The maximum torque from combustion in the engine is

$$T_{emax}(\omega_c) = \frac{V_d \cdot p_{imepmax}(\omega_c)}{4 \cdot \pi}. \tag{A.19}$$

Note that the maximum net output torque of the engine is therefore $T_{icemax} = T_{emax}(\omega_c) - T_{e0}(\omega_c)$. The fuel mass consumption is calculated using

$$\dot{m}_f = \frac{T_e \cdot \omega_c}{e(\omega_c) \cdot Q_{lhv}}, \tag{A.20}$$

where Q_{lhv} is the lower heating value of gasoline. The combustion engine torque T_e is determined using the equations in Appendix A.6. A comparison between the measured and the simulated fuel consumption maps are shown in Fig. A.2. It clearly shows that the model estimates the fuel consumption well. The mass of the internal combustion engine is approximated as $m_e = V_d \cdot 67600$, where V_d is given in m^3. The model assumes no extra fuel consumption during starting of the combustion engine.

It is assumed that there is complete fuel cut-off for negative torque demand throughout the entire speed range of the combustion engine. Instead of injecting fuel to prevent the engine from stalling at low speed the electric motor would provide the additional torque.

A.4 Electric Motor Model

The model for the electric motor is generated from detailed simulation data of a 24 kW motor. To determine the electric power needed from/supplied to the battery a map Γ, derived from detailed simulations, is used

$$P_{m,el} = \Gamma(\omega_c, T_m) \tag{A.21}$$

The efficiency map of the 24 kW electric motor

$$\eta_m(\omega_c, T_m) = \begin{cases} \frac{T_m \cdot \omega_c}{\Gamma(\omega_c, T_m)} & \text{if } T_m \geq 0 \\ \frac{\Gamma(\omega_c, T_m)}{T_m \cdot \omega_c} & \text{if } T_m < 0 \end{cases} \tag{A.22}$$

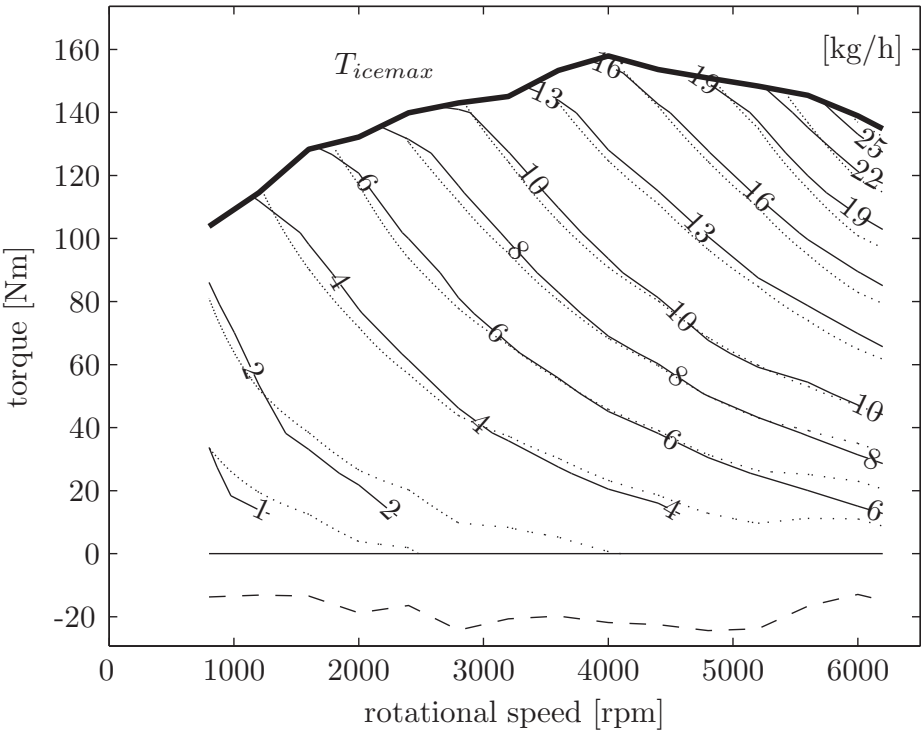

Figure A.2: Internal combustion engine fuel consumption map; measured (solid) and simulated (dotted). The friction mean effective torque is shown in dashed.

is shown in Fig. A.3.

A.5 Battery Model

The battery pack consists of multiple modules in parallel and in series which are each modeled as a voltage source in series with a resistance. The battery model is based on an ADVISOR model of a 6.5 Ah NiMH battery. The battery input/output power is the total power supplied to (or by) the electric motor P_{eltot}

$$P_{eltot} = P_m + P_{aux} \tag{A.23}$$

where P_{aux} is a constant auxiliary power demand. The battery current I_b is calculated using

$$I_b(P_{eltot}) = \frac{V_{oc} - \sqrt{V_{oc}^2 - 4 \cdot R_i \cdot P_{eltot}}}{2 \cdot R_i}, \tag{A.24}$$

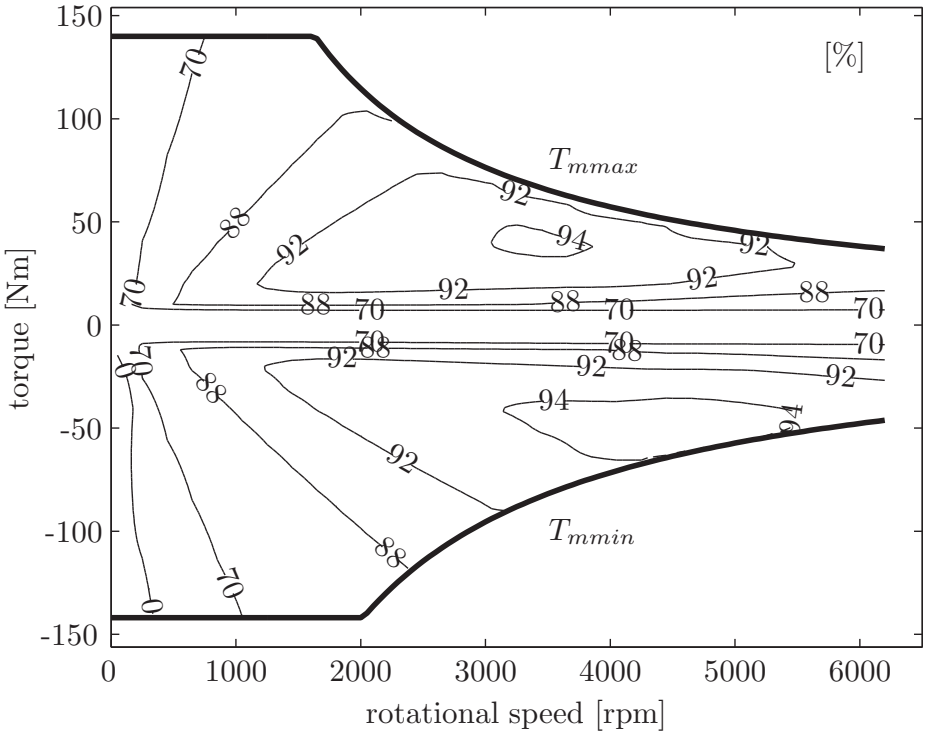

Figure A.3: Electric motor efficiency map, $\eta_m(\omega_c, T_m)$, with maximum and minimum motor torque.

where V_{oc} is the open circuit voltage of the battery and R_i is the battery's internal resistance. Both the open circuit voltage and the internal resistance are functions of the state of charge and the number of modules, and cells per module, used in the battery pack. The battery current is limited to, $I_{min} \leq I_b \leq I_{max}$, where I_{min} and I_{max} depends on the capacity of the battery. The battery's state of charge (SoC) x_k is calculated using

$$\xi_{k+1} = \frac{-I_b \cdot \eta_b(I_b) \cdot t_s}{Q_0} + \xi_k \tag{A.25}$$

where η_b is the battery charging efficiency

$$\eta_b(I_b) = \begin{cases} 1.0 & I_b \geq 0 \\ 0.9 & I_b < 0, \end{cases} \tag{A.26}$$

and Q_0 is the battery capacity.

A.6 Torque Split Factor

The energy management strategy in the hybrid vehicle decides in every time step how the torque demand is split between the electric motor and the combustion engine. The electric motor torque demand T_m and the combustion engine torque demand T_e are determined using the torque split factor $u_s \in [-1,\ 1]$ and the total torque demanded T_d. The torque balance at the input side of the gearbox is

$$T_d - T_{e0} - T_{m0} = J_m \cdot \Delta\omega_c + J_e \cdot \Delta\omega_c + T_c \tag{A.27}$$

where $T_d = T_e + T_m$ is the total torque demanded from the combustion and/or from the electromagnetic forces. The total torque demand for the torque-assist parallel hybrid is

$$T_d = J_m \cdot \Delta\omega_c + J_e \cdot \Delta\omega_c + T_{e0} + T_{m0} + T_c \tag{A.28}$$

and

$$T_d = \begin{cases} J_m \cdot \Delta\omega_c + T_{m0} + T_c & \text{if electric driving} \\ J_m \cdot \Delta\omega_c + J_e \cdot \Delta\omega_c + T_{e0} + T_{m0} + T_c & \text{otherwise} \end{cases} \tag{A.29}$$

for the full parallel hybrid, where T_{e0} is the engine friction torque, J_m is the electric motor inertia, J_e is the engine inertia, $\Delta\omega_c$ is the rotational acceleration of the crankshaft, and T_c is the torque demanded at the gearbox input. Note that the engine friction torque always has to be provided for the torque-assist hybrid, even during pure electric driving, since motor and engine are always coupled. For the full parallel hybrid the engine friction torque does not have to be provided during electric driving since the clutch is assumed to be disengaged.

A summary of the meaning of the torque split factor is shown in Table A.1. Note that this table does not show the complete definition of the input signal u_s. For example, if the torque demand is higher than the maximum torque of the engine, then the range $u_s \in [-1,\ u_0]$ where $u_0 \in (0,\ 1)$ represents boosting with maximum engine load.

The torque split factor $u_s \in [-1,\ 1]$ determines the electric motor torque T_m using a linear interpolation between three distinct values of u_s, namely

Table A.1: Meaning of the control signal u_s

Control signal u_s	T_d	Type of operation
$u_s = -1$	positive	maximum recharging using engine
	negative	purely conventional braking
$u_s \in (-1,\ 0)$	positive	partial recharging using engine
	negative	purely conventional braking
$u_s = 0$	positive	provide all torque by engine
	negative	purely conventional braking
$u_s \in (0,\ 1)$	positive	provide torque by motor and engine
	negative	partial regenerative braking
$u_s = 1$	positive	provide all torque by motor
	negative	maximum regenerative braking

$T_m|_{u_s=1}$, $T_m|_{u_s=0}$, and $T_m|_{u_s=-1}$. This is done in order to guarantee that all $u_s \in [-1,\ 1]$ are feasible and thus minimizing numerical problems when using the dynamic programming algorithm

$$T_m|_{T_d>0} = \begin{cases} \min\{T_{epathmax},\ T_d\} & u_s = 1 \\ \max\{T_d - T_{emax},\ 0\} & u_s = 0 \\ \max\{T_d - T_{emax},\ T_{epathmin}\} & u_s = -1 \end{cases} \tag{A.30}$$

$$T_m|_{T_d<0} = \begin{cases} \max\{T_{epathmin},\ T_d\} & u_s = 1 \\ 0 & u_s = 0 \\ 0 & u_s = -1. \end{cases} \tag{A.31}$$

The combustion engine torque is then given by

$$T_e = \begin{cases} T_d - T_m & T_d > 0 \\ 0 & T_d < 0 \end{cases} \tag{A.32}$$

The maximum torque $T_{epathmax}$ and the minimum torque $T_{epathmin}$ of the electric path are calculated by inverting the battery and the electric motor model.

Appendix B

Driving Cycles

The drive cycles considered, shown in Fig. B.1, are the New European Driving Cycle (NEDC) according to the directive 70/220/EEC with all its amendments, the urban part of the Common Artemis Driving Cycle [18] (CADC Urban), the road part of the Common Artemis Driving Cycle (CADC Road), the highway part of the Common Artemis Driving Cycle (CADC Highway), the complete Common Artemis Driving Cycle (CADC), the Highway Federal Emissions Test cycle (HWFET), the Federal Test Procedure 72 cycle (FTP-72) which is also known as the Urban Dynamometer Driving Schedule (UDDS), and the US06 Supplemental Federal Test Procedure cycle (US06).

The cycles chosen include different driving patterns ranging from low-speed city driving to demanding high-speed cycles. The speed profiles have been adjusted such that a conventional vehicle with a 1.6 liter combustion engine is capable to drive them. This is done in order to have exactly the same speed profile for varying hybridization ratios.

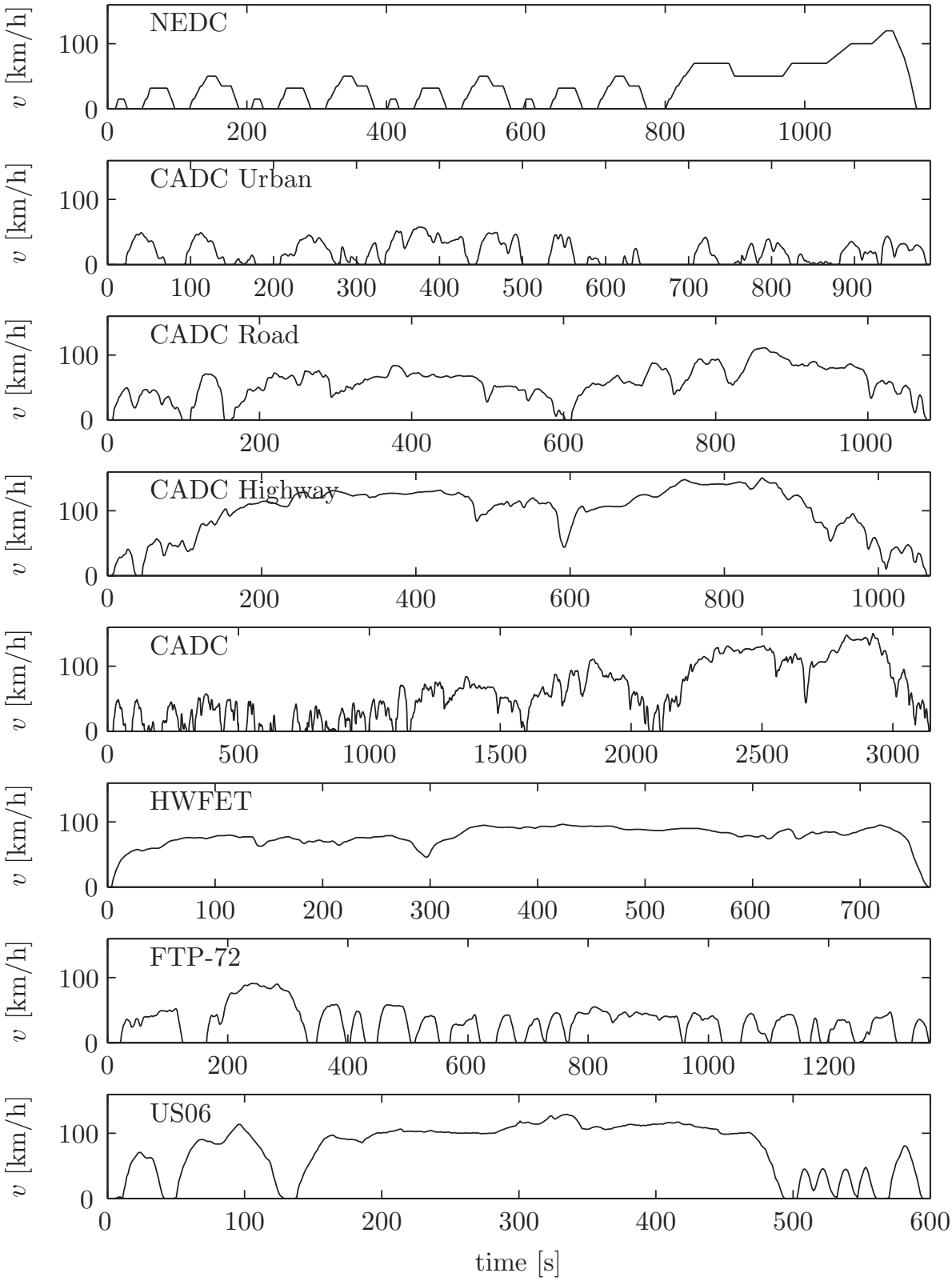

Figure B.1: The driving cycle speed profiles: NEDC, CADC Urban, CADC Road, CADC Highway, CADC, HWFET, FTP-72, and US06.

Appendix C

Hamiltonian Minimization

The amount of boosting $P_m^{bo}(s)$ in (2.37) is limited by the electric motor maximum power constraint when

$$P_m^{bo}(s) > P_{mmax} \tag{C.1}$$

which is equivalent to

$$s < s_{lim}^{bo,m} \triangleq \frac{\eta^2}{e(2P_{mmax}\alpha + \eta)}. \tag{C.2}$$

The amount of recharging $P_m^{re}(s)$ in (2.39) is limited by the electric motor minimum power constraint when

$$P_m^{re}(s) < P_{mmin} \tag{C.3}$$

which is equivalent to

$$s > s_{lim}^{re,m} \triangleq \frac{1}{\eta e(1 + 2\alpha\eta P_{mmin})}. \tag{C.4}$$

When the electric motor minimum power constraint is active in the recharging region, electric driving is optimal for $P_d > 0$ when

$$H_{el}(P_d) < H_{re}(P_{mmin}) \tag{C.5}$$

$$P_d < P_{lim}^{re,m}(s) \triangleq \ldots$$

$$\frac{-\left(\frac{s}{\eta} - \frac{1}{e}\right) + \sqrt{\left(\frac{s}{\eta} - \frac{1}{e}\right)^2 + 4\frac{s\alpha}{e\eta^2}\Psi_1}}{2\frac{s\alpha}{\eta^2}} \tag{C.6}$$

where

$$\Psi_1 = \left(P_0 + P_{mmin}(\eta e s(1 + P_{mmin}\eta\alpha) - 1)\right). \tag{C.7}$$

If $P_d < 0$ then recuperation is optimal when

$$H_{el}^{-}(P_d) < H_{re}\left(P_{mmin}\right) \tag{C.8}$$

$$P_d < P_{lim}^{re,m-}(s) \triangleq \ldots$$

$$\frac{-\left(\frac{s}{\eta} - \frac{1}{e}\right) + \sqrt{\left(\frac{s}{\eta} - \frac{1}{e}\right)^2 + 4s\alpha\eta^2\Psi_2}}{2\frac{s\alpha}{\eta^2}} \tag{C.9}$$

where

$$\Psi_2 = \left(\frac{P_0}{e} + \left(s\eta - \frac{1}{e}\right)P_{mmin} + s\alpha\eta^2 P_{mmin}^2\right). \tag{C.10}$$

Nomenclature

Latin Symbols

A	Area	[m^2]
B	Boolean (1/0)	[-]
E	Energy	[J]
F	Force	[N]
H	Hamiltonian	[W]
I	Current	[A]
J	Cost	[-]
	Inertia	[kgm^2]
$\mathcal{J}$	Cost-to-go	
P	Power	[W]
Q_0	Battery capacity	[As]
Q_{lhv}	Lower heating value	[J/kg]
T	Torque	[Nm]
$\mathcal{X}$	State space	
$\mathcal{U}$	Input space	
V	Voltage	[V]
	Volume	[m^3]
a	Acceleration	[m/s^2]
c_d	Air drag coefficient	[-]
c_r	Rolling friction coefficient	[-]
e	Internal engine efficiency	[-]
g	Gravity constant	[N]
m	Mass	[kg]
$\overset{*}{m}_f$	Mass flow	[kg/s]

p	Pressure	[Pa]
s	Equivalence factor	[-]
t	Time	[s]
t_{gs}	Gear Shift Duration	[s]
t_s	Time step	[s]
$\boldsymbol{x}$	State vector	
$\boldsymbol{u}$	Input vector	
v	Speed	[m/s]
$\boldsymbol{w}$	Disturbance vector	

Greek Symbols

Γ	Electric motor map	[W]
α	Electric path coefficient	[W^{-1}]
γ	Gear ratio	[-]
ϵ	Error	[-]
η	Efficiency	[-]
λ	Costate	
ξ	Battery state-of-charge	[-]
ρ	Density	[kg/m^3]
φ	Gear number	[-]
ω	Rotational speed	[rad/s]
$\Delta\omega$	Rotational acceleration	[rad/s^2]

Abbreviations

BAT	Battery
CADC	Common Artemis Driving Cycle
CFC	Causal Feedback Controller
DCT	Dual Clutch Transmission
DP	Dynamic Programming
DPM	Dynamic Programming Matrix (Function)
ECMS	Equivalent Consumption Minimization Strategy
EM	Electric Motor

EP	Equilibrium Point
EPS	Equilibrium Point Strategy
F	Full (Parallel Hybrid)
FTP-72	Federal Test Procedure 72
GPS	Global Positioning System
HEV	Hybrid Electric Vehicle
HR	Hybridization Ratio
HWFET	Highway Federal Emissions Test
ICE	Internal Combustion Engine
NEDC	New European Driving Cycle
OO	Optimal Torque Split / Optimal Gear Shifting
OS	Optimal Torque Split / Standard Gear Shifting
SHM	Selective Hamiltonian Minimization
TA	Torque-Assist (Parallel Hybrid)
TEPS	Transmission Equilibrium Point Strategy
US06	Supplemental Federal Test Procedure

List of Tables

List of Figures

Bibliography

[1] K. Oh, J. Min, D. Choi, and H. Kim. Optimization of control strategy for a single-shaft parallel hybrid electric vehicle. *Journal of Automobile Engineering*, 221:555–565, 2007.

[2] P. Tona, P. Moulin, S. Venturi, R. Tilagone, and P. Gautier. Towards integrated powertrain control for a mild-hybrid urban vehicle with a downsized turbo-charge CNG engine. *Oil and Gas Science and Technology*, 62(4):595–613, 2007.

[3] H.-D. Lee, S.-K. Sul, H.-S. Cho, and J.-M. Lee. Advanced gear-shifting and clutching strategy for a parallel-hybrid vehicle. *IEEE Industry Applications Magazine*, 6(6):26–32, 2000.

[4] O. Sundstrom, L. Guzzella, and P. Soltic. Optimal hybridization in two parallel hybrid electric vehicles using dynamic programming. In *Proc. of the 17th IFAC World Congress*, pages 4642–4647, Seoul, Korea, 2008.

[5] A. Sciarretta and L. Guzzella. Control of hybrid electric vehicles. *IEEE Control Systems Magazine*, 27(2):60–70, 2007.

[6] N. J. Schouten, A. Salman, and N. A. Kheir. Energy management strategies for parallel hybrid vehicles using fuzzy logic. *Control Engineering Practice*, 11(2):171–177, 2003.

[7] J.-S. Won and R. Langari. Intelligent energy management agent for a parallel hybrid vehiclepart II: Torque distribution, charge sustenance strategies, and performance results. *IEEE Transactions on Vehicular Technology*, 54(3):935–953, 2005.

[8] C.-C. Lin, J.-M. Kang, J.W. Grizzle, and H. Peng. Energy management strategy for a parallel hybrid electric truck. In *Proceedings of*

the American Control Conference, Arlington, VA, USA, June 25–27 2001.

[9] G. Paganelli, T. M. Guerra, J.-J. Santin, A. Noel, M. Delhom, and E. Combes. Single shaft parallel hybrid car powertrain: Modelisation and control. In *International Conference on Advances in Vehicle Control and Safety*, pages 415–419, Amiens, France, July 1–4 1998.

[10] G. Paganelli, T. M. Guerra, S. Delprat, J.-J. Santin, M. Delhom, and E. Combes. Simulation and assessment of power control strategies for a parallel hybrid car. *Journal of Automobile Engineering*, 214(7):705–717, 2000.

[11] A. Brahma, Y. Guezennec, and G. Rizzoni. Optimal energy management in series hybrid electric vehicles. In *Proceedings of the American Control Conference*, pages 60–64, Chicago, IL, USA, June 28–30 2000.

[12] A. Sciarretta, M. Back, and L. Guzzella. Optimal control of parallel hybrid electric vehicles. *IEEE Transactions on Control Systems Technology*, 12(3):352–363, 2004.

[13] C. Musardo, G. Rizzoni, Y. Guezennec, and B. Staccia. A-ECMS: An adaptive algorithm for hybrid electric vehicle energy management. *European Journal of Control*, 11(4–5):509–524, 2005.

[14] S. Delprat, T.M. Guerra, and J. Rimaux. Optimal control of a parallel powertrain: from global optimization to real time control strategy. In *Proceedings of Vehicular Technology Conference, IEEE 55th*, volume 4, pages 2082–2088, Birmingham, AL, USA, May 6–9 2002.

[15] R. Cipolone and A. Sciarretta. Analysis of the potential performance of a combined hybrid vehicle with optimal supervisory control. In *Proceedings of the 2006 IEEE international conference on control applications*, pages 2802–2807, October 2006.

[16] M. Athans and P. L. Falb. *Optimal Control*. New York: McGraw-Hill, 1966.

[17] X. Wei, L. Guzzella, V. Utkin, and G. Rizzoni. Model-based fuel optimal control of hybrid electric vehicle using variable structure control systems. *Journal of Dynamic Systems, Measurement, and Control*, 129(1):13–19, 2007.

[18] M. Andr. The artemis european driving cycles for measuring car pollutant emissions. *Science of The Total Environment*, 334–335(1):73–84, 2004.

[19] L. Guzzella and A. Amstutz. CAE tools for quasi-static modeling and optimization of hybrid powertrains. *IEEE Transactions on Vehicular Technology*, 48(6):1762–1769, 1999.

[20] L. Guzzella and A. Sciarretta. *Vehicle propulsion systems: Introduction to modeling and optimization*. Springer, Berlin, 2nd edition, 2007.

[21] L. Guzzella. Discrete-event IC engine models: Why the constant speed assumption is valid. *Journal of Dynamic Systems, Measurement, and Control*, 125(4):674–676, 2003.

[22] R.E. Bellman. *Dynamic programming*. Princeton University Press, Princeton, NJ, 1957.

[23] D.P. Bertsekas. *Dynamic Programming and Optimal Control*. Athena Scientific, 1995.

[24] O. Sundström, D. Ambühl, and L. Guzzella. On implementation of dynamic programming for optimal control problems with final state constraints. In *Proceedings of Les Rencontres Scientifiques de l'IFP: Advances in Hybrid Powertrains*, Rueil-Malmaison, France, November 25–26 2008.

[25] P. Pisu and G. Rizzoni. A comparative study of supervisory control strategies for hybrid electric vehicles. *IEEE Transactions on Control Systems Technology*, 15(3):506–518, 2007.

[26] D. Ambühl, A. Sciarretta, C. Onder, L. Guzzella, S. Sterzing, K. Mann, D. Kraft, and M. Küsell. A causal operation strategy for hybrid electric vehicles based on optimal control theory. In *Proceedings of the 4th Symposium on Hybrid Vehicles and Energy Management*, pages 318–331, Braunschweig, Germany, February 14–15 2007.

[27] D. Ambühl and L. Guzzella. Preditive reference signal generator for hybrid electric vehicles. *IEEE Transactions on Vehicular Technology*, 2009. Accepted for publication.

[28] A. H. Glattfelder and W. Schaufelberger. *Control Systems with Input and Output Contstraints*. Springer Verlag, Berlin, 2003.

[29] J.-S. Won, R. Langari, and M. Ehsani. An energy management and charge sustaining strategy for a parallel hybrid vehicle with CVT. *IEEE Transactions on Control Systems Technology*, 13(2):313–320, 2005.

[30] F. Wang, X.-J. Mao, H. Zhong, and Z.-L. Ma. Parallel hybrid electric system energy optimization control with automated mechanical transmission. *Journal of Automobile Engineering*, 223(2):151–167, 2008.

[31] G. Paganelli, G. Ercole, A. Brahma, Y. Guezennec, and G. Rizzoni. General supervisory control policy for the energy optimization of charge-sustaining hybrid electric vehicles. *JSAE Review*, 22(4):511–518, 2001.

[32] R. C. Baraszu and S. R. Cikanek. Torque fill-in for an automated shift manual transmission in a parallel hybrid electric vehicle. In *Proc. of the American Control Conference*, pages 1431–1436, Anchorage, AK, USA, 2002.

[33] M. Kulkarni, T. Shim, and Y. Zhang. Shift dynamics and control of dual-clutch transmissions. *Mechanism and Machine Theory*, 42(2):168–182, 2007.

[34] Y. Zhang, X. Chen, X. Zhang, H. Jiang, and W. Tobler. Dynamic modeling and simulation of a dual-clutch automated lay-shaft transmission. *ASME Journal of Mechanical Design*, 127(2):302–307, 2005.

[35] O. Sundström, L. Guzzella, and P. Soltic. Torque-assist hybrid electric powertrain sizing: From optimal control towards a sizing law. *IEEE Transactions on Control Systems Technology*, 2009. submitted.

[36] J. Larminie and J. Lowry. *Electric vehicle technology explained*. Wiley, Chichester, 2003.

[37] M. Back, S. Terwen, and V. Krebs. Predictive powertrain control for hybrid electrical vehicles. In *IFAC Symposium on Advances in Automotive Control*, pages 451–457, Salerno, Italy, April 2004.

[38] D. Ambuehl and L. Guzzella. Predictive reference signal generator for hybrid electric vehicles. *IEEE Transactions on Vehicular Technology*, 2009. submitted.

[39] S. M. Lukic and A. Emadi. Effects of drivetrain hybridization on fuel economy and dynamic performance of parallel hybrid electric vehicles. *IEEE Transactions on Vehicular Technology*, 53(2):385–389, 2004.

[40] T. C. Moore. HEV control strategy implications of performance criteria, system configuration and design, and component selection. In *Proc. of the American Control Conference*, pages 679–683, Albuquerque, New Mexico, USA, 1997.

[41] D. J. Santini, A. D. Vyas, J. L. Anderson, and F. An. Hybridizing with engine power reduction. *Transportation Research Record*, 1915:19–26, 2002.

[42] K. Oh, J. Kim, D. Kim, D. Choi, and H. Kim. Optimal power distribution control for parallel hybrid electric vehicles. In *IEEE International Conference on Vehicular Electronics and Safety 2005*, pages 79–85, 2005.

[43] M. R. Cuddy and K. B. Wipke. Analysis of the fuel economy benefits of drivetrain hybridization. In *SAE International Congress and Exposition*, Detroit, MI, USA, 1997. SAE paper 970289.

[44] D. Rotenberg, A. Vahidi, and I. Kolmanovsky. Ultracapacitor assisted powertrains: Sizing, modeling and control, and the impact on fuel economy. In *Proc. of the American Control Conference*, pages 981–987, Seattle, WA, USA, 2008.

[45] L. Triger, J. Paterson, and P. Drozdz. Hybrid vehicle engine size optimization. In *SAE Future Transportation Technology Conference and Exposition*, San Antonio, TX, USA, 1993. SAE paper 931793.

[46] F. An, F. Stodolsky, and D. Santini. Hybrid options for light-duty vehicles. In *SAE Future Transportation Technology Conference and Exposition*, Costa Mesa, CA, USA, 1999. SAE paper 1999-01-2929.

[47] C. Holder and J. Gover. Optimizing the hybridization factor for a parallel hybrid electric small car. In *Proc. of the IEEE Vehicle Power and Propulsion Conference*, pages 1–5, 2006.

[48] V. Galdi, L. Ippolito, A. Piccolo, and A. Vaccaro. A genetic-based methodology for hybrid electric vehicles sizing. *Soft Computing*, 5(6):451–457, 2001.

[49] X. Hu, Z. Wang, and L. Liao. Multi-objective optimization of HEV fuel economy and emissions using evolutionary computation. In *SAE World Congress and Exhibition*, Detroit, MI, USA, 2004. SAE paper 2004-01-1153.

[50] M.-J. Kim and H. Peng. Combined control/plant optimization of fuel cell hybrid vehicles. In *Proc. of the American Control Conference*, pages 496–500, Minneapolis, Minnesota, USA, 2006.

[51] U. Zoelch and Schroeder D. Dynamic optimization method for design and rating of the components of a hybrid vehicle. *International Journal of Vehicle Design*, 19(1):1–13, 1998.

[52] G. Y. Liao, T. R. Weber, and D. P. Pfaff. Modelling and analysis of powertrain hybridization on all-wheel-drive sport utility vehicles. *Journal of Automobile Engineering*, 218(D):1125–1134, 2004.

[53] B. M. Baumann, G. Washington, B. C. Glenn, and G. Rizzoni. Mechatronic design and control of hybrid electric vehicles. *IEEE/ASME Transactions on Mechatronics*, 5(1):58–72, 2000.

[54] I. Bolvashenkov, H. G. Herzog, and A. Engstle. Factor of hybridization as a design parameter for hybrid vehicles. In *Proc. of the International Symposium on Power Electronics, Electrical Drives, Automation and Motion*, pages 926–929, Taormina, Italy, 2006.

[55] O. Sundström and A. Stefanopoulou. Optimum battery size for fuel cell hybrid electric vehicle, part 1. *ASME Journal of Fuel Cell Science and Technology*, 4(2):167–175, May 2007.

[56] M.B. Schaefer. Some aspects of the dynamics of populations important to the management of the commercial marine fisheries. *Bulletin of Mathematical Biology*, 53:253–279, 1991. Reprinted from the Bulletin of the Inter-American Tropical Tuna Commission, 1(2):27–56, 1954.

[57] O. Sundström and L. Guzzella. DPM-function. *Institute for Dynamic Systems and Control, Department of Mechanical and Process Engineering, ETH Zurich*, 2009. http://www.idsc.ethz.ch/.

[58] H. Mosbech. Optimal control of hybrid vehicle. In *Proc. of the International Symposium on Automotive Technology & Automation*, volume 2, pages 303–310, Turin, Italy, 1980.

[59] C.-C. Lin, H. Peng, J. W. Grizzle, and J.-M. Kang. Power management strategy for a parallel hybrid electric truck. *IEEE Transactions on Control Systems Technology*, 11(6):839–849, 2003.

[60] A. Sciarretta, M. Back, and L. Guzzella. Optimal control of parallel hybrid electric vehicles. *IEEE Transactions on Control Systems Technology*, 12(3):352–363, 2004.

[61] L. Guzzella and C.H. Onder. *Modeling and control of internal combustion engine systems.* Springer, Berlin, 2004.

[62] S. J. Pachernegg. A closer look at the willans-line. In *SAE International Automotive Engineering Congress and Exposition*, Detroit, MI, USA, 1969. SAE paper 690182.